



A review on machining of NiTi shape memory alloys: the process and post process perspective

Eren Kaya¹ · İrfan Kaya¹

Received: 19 June 2018 / Accepted: 1 October 2018 / Published online: 13 October 2018
© Springer-Verlag London Ltd., part of Springer Nature 2018

Abstract

Nickel–titanium (NiTi) shape memory alloys have gained more prominence due to their functional and mechanical properties. This material undergoes solid-state phase transformation during machining. Together with this, inherent properties of this material result in challenging machinability behaviors such as excessive tool wear, high cutting forces, and degraded surface integrity. Furthermore, unique stress–strain curve of this material complicates predicting machining behaviors. This paper reviews research in the machining of NiTi shape memory alloys carried out over the last 20 years with the objective of assessing overall machinability characteristics. It is concluded that functional properties and machinability responses of NiTi are very sensitive to machining parameters and environment. Machinability rate of NiTi should be assessed not only by usual machinability measures (i.e., tool wear, cutting forces, surface integrity) but also by considering post machining functional behaviors.

Keywords Machinability · NiTi · Shape memory alloy · Tool wear · Surface integrity · Functional quality

Nomenclature

A	austenite	M	martensite
A_s	austenite start temperature	M_s	martensite start temperature
A_f	austenite finish temperature	M_f	martensite finish temperature
a_p	axial depth of cut	\dot{m}	mass flow rate
a_e	radial depth of cut	n	rotational speed
α_o	flank angle	P	pressure
e_C	specific cutting energy	R_a	arithmetic average height
F_C	cutting force	R_z	ten-point mean roughness
F_f	feed force	r	nose radius
F_Z	normal force	r_e	edge radius
f	feedrate	Q	volumetric flow rate
f_Z	feed per tooth	T	temperature
h	machining induced layer	t_R	distance from edge
H_m	microhardness	u	flow velocity
κ_r	cutting edge angle	VB_{max}	maximum flank wear
l	drilling depth	VB_{notch}	notch flank wear
L	milling length	V_c	cutting speed
		σ^{As}	austenite start stress level
		σ^{Af}	austenite finish stress level
		σ^{Ms}	martensite start stress level
		σ^{Mf}	martensite finish stress level
		σ_S	detwinning start stress
		σ_f	detwinning finish stress
		γ_o	rake angle
		ΔH	latent heat

✉ Eren Kaya
erenkaya@anadolu.edu.tr

¹ Department of Mechanical Engineering, Eskisehir Technical University, 26555 Eskisehir, Turkey

1 Introduction

With the advancements in material science and engineering, a deeper understanding of microstructure and processing of materials have been improved dramatically over the last century. Advancement in the understanding of a material type is often the forerunner to the stepwise progression of a technology. For example, automobiles would not have been possible without the availability of inexpensive steel or any other comparable substitutes. Accordingly, the increasing demand for lighter, stronger and functional materials spawned active materials. Shape memory alloys (SMAs) are a unique class of active materials, which can recover to their original shape after applying stimuli, such as deformation due to stress, heat or magnetic field [1]. SMAs possess attractive characteristics such as ability to provide large recoverable strain during mechanical loading (pseudoelasticity), shape recovery upon heating (shape memory effect, SME), and potent biocompatibility, which make SMAs one of the suitable actuators for biomedical applications. The main advantages of SMAs are the high actuation stress and mechanical strength they can provide when compared to the other types of shape memory polymers and shape memory hybrids [1]. SMAs have been employed in many applications, such as in automotive [2, 3], aerospace [4, 5], biomedical [6], communication [7, 8], composites and structures [9], micro-actuators, and micro-electromechanical systems [10, 11]. A brief overview of applications that SMAs have been used are given in Table 1. There are various alloying compositions, each of which comes with special properties, present among the SMAs. Although copper-based and iron-based SMAs are low cost and commercially available, they have not been used very often due to their instability, impracticability [12], and poor thermo-

mechanical performance [13, 14]. NiTi-based SMAs are the most commonly studied and used ones since they ensure better functional fatigue and biocompatibility properties [15]. Although most studies suggest these materials for having good biocompatibility, there are still questions regarding *in vivo* performance and molecular level interactions at cell [16]. Among these questions, stress-assisted corrosion [17] and toxic effects of ion release [18] are the most significant ones. It was reported that, however, the titanium oxide layer formed on NiTi acts as a barrier to corrosion and chemical interactions and confines the diffusion of nickel ions [15, 19]. Most of the scholars came to an agreement that *in vivo* and *in vitro* biocompatibility of NiTi is very eligible for biomedical applications [20, 21].

Manufacturing processes play a very important role in shaping the final desired product. Due to its unique shape memory properties, manufacture of NiTi needs special attention. In order to manufacture desired NiTi parts, developing a better understanding of the unique properties of NiTi is required.

1.1 Shape memory property

The mechanism of the shape memory phenomenon of the SMAs is based on diffusionless solid phase transformation [22], which should be well understood to predict mechanical behaviors. Within typical operating temperatures, NiTi have two phases (austenite and martensite), three different crystal structures (i.e., twinned martensite, detwinned martensite, and austenite) [14], and there are six possible transformations [22]. The martensite (M) or product phase, which has a monoclinic crystal structure, is stable at low temperatures while the austenite (A) or parent phase, which has generally a cubic crystal

Table 1 Present and prospective applications of SMAs

Application domain	Function/part	Application examples
Automotive	Engine	Radiator, fan clutch, engine control, fuel injector, valves
	Drivetrain	Transmission control
	Wheel/brake/suspension	Brake, absorber, tire
	Body	Lamps, wiper, sunroof, side mirror, engine hood, spoiler
Aerospace	Interior	Rear view window, airbags, dashboard
	Engine	Inlet, rotor, nozzle
Robotics	Body	Aero-structure, skin, wing, winglet, flap edge
	Biomimetic	Crawling, walking, rolling, climbing, swimming, flying
Biomedical	Biomedical	Endoscopic
	Humanoid robots	Fingers, hands, head, facial expression
	Vascular	Stents, filters, arteries, vessels, valves, aorta
	Orthopedic	Skull, spine, bone, muscles, fingers
Communication	Orthodontic	Braces, brackets, palatal arches, files
	Surgical instruments	Catheters, scopes, suture
Communication	Antenna	Radio frequency slot antenna

structure, is stable at high temperatures. There are two forms of martensite: twinned martensite (self-accommodated) and detwinned martensite (reoriented). When austenitic SMA is cooled in the absence of a load, the crystal structure changes from austenite to martensite (forward transformation) resulting in the twinned martensite variant. The transformation begins to revert to martensite at the martensite start temperature (M_s) and completes at the martensite finish temperature (M_f). When a mechanical load is applied on the twinned martensite, reorientation of the variants (detwinning process) causes a permanent macroscopic shape change. Upon heating the material above a critical temperature, the reverse transformation begins at the austenitic start temperature (A_s). Similarly, when the material is further heated, austenitic transformation is completed at the austenitic finish temperature (A_f) and the original shape of the SMA is regained. This phenomenon is called the shape memory effect. Figure 1 represents above described shape memory effect of NiTi.

1.2 Pseudoelasticity

Phase transformation can also be induced by applying mechanical load to SMAs in the austenitic phase. When enough mechanical load is applied to the material above A_f temperature, martensitic transformation initiates at the critical stress level (σ^{Ms}). Upon further mechanical loading, martensitic phase transformation is completed at the σ^{Mf} stress level. This loading results in a stable detwinned martensite phase. It should be noted that this elastic loading is accompanied by large inelastic strains [23]. Further increasing the stress above the σ^{Mf} causes elastic deformation of the detwinned martensite. When the load is released gradually under constant

temperature, austenitic phase transformation initiates at the critical stress level (σ^{As}). Due to phase transformation during unloading, recovery of strain is observed on the material and the austenitic phase transformation is completed at the σ^{Af} stress level. This rubber-like super elastic behavior of the material is called pseudoelasticity [24]. Above described pseudoelastic behavior is represented in Fig. 2. Here, path 2 shows a mechanical loading at a stable temperature (above A_f). In path 1, thermo-mechanical loading is applied under varying temperature. The horizontal and dotted lines between σ^{As} and σ^{Af} indicate detwinning start stress level (bottom line) and detwinning finish stress level (top line).

1.3 Melting and preprocessing of NiTi

Composition and thermal/mechanical treatments have a direct influence on the shape memory effect, pseudoelasticity, damping, impact absorbing, and thermo-mechanical properties of NiTi. An alteration of 0.1 at.% in the nickel content was shown to shift the transformation temperatures by nearly 10 °C [15, 25]. Due to this extreme sensitivity, nickel and titanium ratio should be strictly controlled during melting practice in order to meet required transformation temperatures. Figure 3 displays the NiTi binary equilibrium phase diagram. It can be seen that thermodynamically stable phases exist in the proximity of equiatomic percentages of nickel and titanium.

Due to the high reactivity of titanium in NiTi, melting must be done in a vacuum or an inert atmosphere. Vacuum arc melting (VAR) and vacuum induction melting (VIM) processes are commonly used for casting of NiTi. Combination of VIM and VAR melting is often used to achieve further refining.

Fig. 1 Stress–strain–temperature relationship of typical NiTi SMA demonstrating shape memory effect [23]

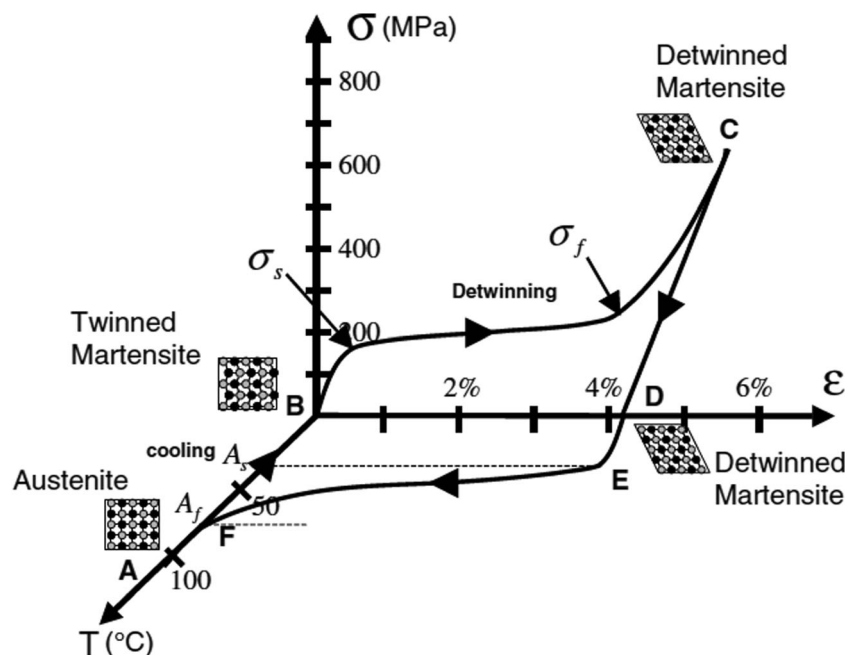
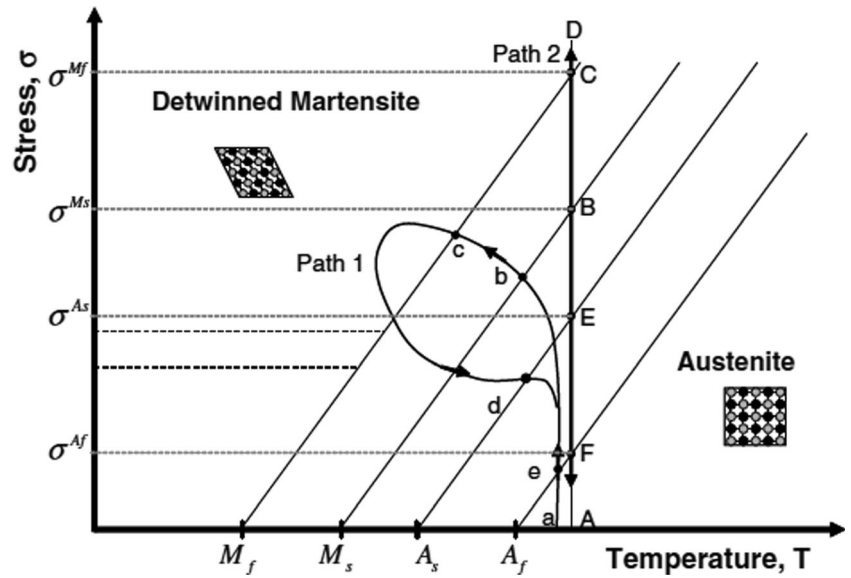


Fig. 2 Pseudoelastic loading cycle [23]

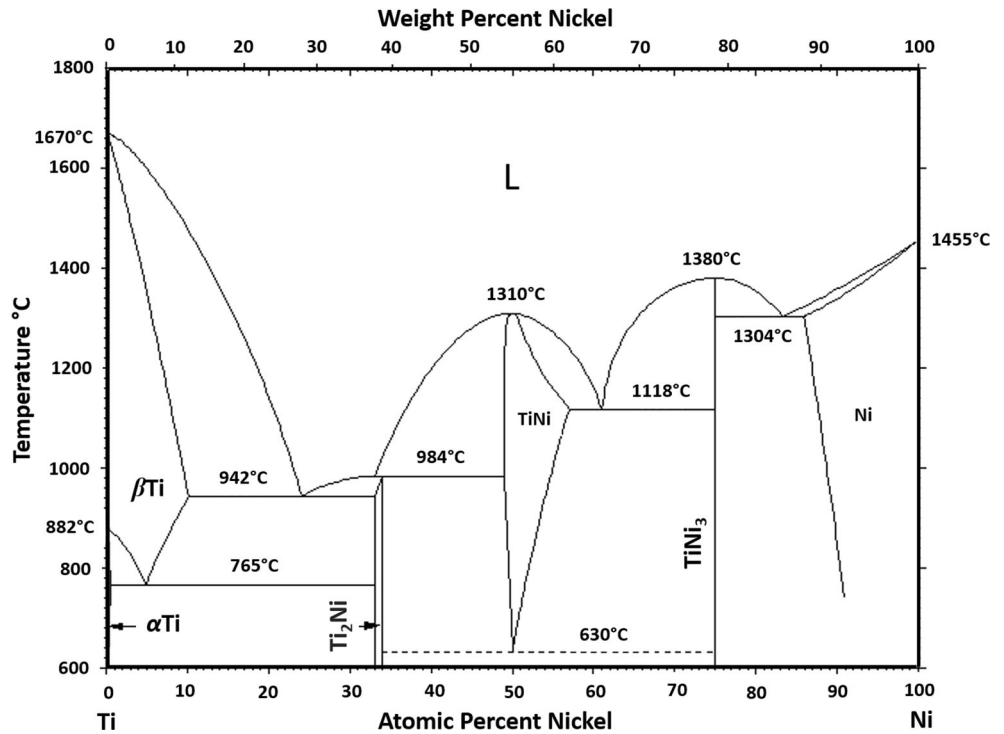


Electron beam melting and plasma melting have been reported to be used in experimental scales [27]. NiTi parts can be produced by powder metallurgy methods such as conventional sintering or selective laser melting [28]. Optimal hot working temperatures for NiTi have been reported to be around 800 °C where the alloy is easily workable [27].

Heat treatment parameters of NiTi should be experimentally determined for desired phase transformation temperatures. Typically, temperatures close to 500 °C and treatment duration

over 5 min are employed for super-elastic SMAs. But, lower temperatures between 300 and 400 °C are also suitable if enough time is allowed. Alternatively, solution heat treatment at high temperatures between 600 and 900 °C followed by aging treatment around 400 °C can be applied to alloys containing more than 55.5 wt.% nickel to obtain good superelastic or shape memory properties [27]. Transformation temperatures can be tailored owing to precipitation formation by aging [29].

Fig. 3 NiTi binary phase diagram [26]



1.4 Cold forming

In addition to heat treatment, pseudoelasticity and shape memory behavior of NiTi SMAs may be optimized by cold working methods. Furthermore, alterations in mechanical properties such as decreased ductility or increased strength are possible with cold working processes [30]. Cold forming is a cold working process and it is used for shaping the material to desired geometry. Earlier works on cold working of NiTi have shown that transformation temperatures of NiTi SMAs are related to lattice defects due to cold working [31, 32]. It was observed that when the specimens were worked under recrystallization temperature, appearance of two separate peaks (i.e., rhombohedral (R) phase) during martensitic phase transformation was observed [33]. This intermediate phase, which is formed due to increased dislocation density, inhibits growth of martensitic phase and shift the transformation temperatures [34, 35]. Furthermore, cold working of NiTi may have substantial effects on functional fatigue properties of the material [36].

Miller et al. investigated influences of cold work and heat treatment on the shape memory effect and plastic strain development of NiTi SMAs [32]. They reported that an increase in cold work resulted in transformation hardening which led to decreased transformation strains during thermally induced phase transformation. Additionally, it was shown that an increase in the amount of applied cold work remarkably decreased the latent heat. This was resulted from stabilized martensite due to high levels of plastic deformation. This “pinned” martensite restricts the amount of material transformed. Fully annealing this material for recrystallization eliminated this trapped martensite. Similar results were reported by Frick et al. [37]. Differential scanning calorimetry (DSC) results of the study showed that cold-drawn sample with no post treatment displayed no visible transformations, whereas the increase of aging temperature after cold working resulted in increased transformation enthalpy. This was attributed to dislocation annihilation and precipitate growth. As expected, cold drawn NiTi displayed larger hardness values than cold-drawn and heat treated or hot-rolled NiTi. Khaleghi et al. investigated influence of short-time annealing heat treatment on the superelastic behavior of cold drawn Ni-rich binary Ni_{50.9}Ti_{49.1} (at.%) [38]. They found that increasing the cold work level leads to improved superelastic behavior if proper annealing time is selected. Lei et al. investigated effects of cold drawing and annealing amount on mechanical and superelasticity properties of cold drawn ultra-thin NiTi wire [39]. They showed that increase of the cold drawing amount under 500 °C annealing temperature resulted in decreased super-elasticity. Canadinc et al. investigated effects of wire drawing followed by annealing heat treatment on deformation response and cyclic stability of Ni₅₀Ti₃₅Hf₁₅ SMA wires [40]. Wire drawing followed by annealing was reported to increase

strength and superelasticity of the material by replacing initial brittle response with ductile response. These studies show that it is possible to produce NiTi parts by cold forming processes with good properties. Phase transformation and mechanical properties of NiTi may be altered by controlling the cold work and heat treatment parameters. Cold work without any following annealing heat treatment has been reported to increase dislocation density. This inhibits plastic flow, which consequently increases hardness, as well as martensitic transformation. More specifically, transformation temperatures, latent heat, superelasticity, hardness, ductility, and strength have been reported to be greatly influenced by cold work deformation, annealing temperature, and time. In order to produce parts at desired mechanical and phase transformation properties, these parameters need to be optimized. Considering all these factors, cold forming may be an alternative to machining process for parts without complex geometries or with larger dimensional tolerances. Alternatively, cold forming may be adopted before precise machining in order to tailor the functional or mechanical properties of the workpiece.

1.5 Machinability

Machining is one of the most widely employed manufacturing process due to its precise shaping capabilities, economical aspects and operational reliability of the final product. Considering the application areas of NiTi (i.e., biomedical, aerospace), machining operations are widely employed in order to produce precise and reliable products. However, the machinability of NiTi is considered to be very challenging due to several reasons such as high strain hardening, unconventional stress–strain characteristics, severe adhesion, and poor chip breaking [15, 41, 42]. Inherent material properties like low thermal conductivity, high specific heat [43], and low effective elastic modulus [44] have been considered to be further limitations. These factors lead to poor machinability characteristics such as high specific cutting energy and cutting forces [45], severe tool wear [42], and excessive burr formation [46]. Furthermore, these factors may negatively affect the surface integrity characteristics of the finished product.

Phase transformation plays a major role in the machining of NiTi alloys as pointed out by Kong et al. [47]. The transformation temperature window of these materials is rather narrow (around 80 °C), depending on the material composition, heat treatment history, manufacturing method, and cold working conditions. A small change of thermal phase may alter the material properties significantly. As a result, mechanical and metallurgical machinability behaviors of the material may be quite sensitive to even small variations in machining parameters. For example, having the symmetry of a cube in austenite phase, NiTi is very hard and rigid. However, when in martensite phase, being not symmetrical, it is rather malleable and soft [43, 48]. This leads to a narrow window of proper machining

parameters [49], which are mostly determined by experimental studies for specific cutting conditions. Considering the fact that machinability response of these alloys is quite unique and not well understood yet, an in-depth analysis of the current state of NiTi machinability characteristics is required.

Functional performance of SMAs is of great importance since these materials are mainly employed for their shape memory, pseudoelasticity, actuation, and damping properties. It was shown that the functional behaviors of NiTi may be affected from process parameters during machining [50]. This is because the transformation behaviors of these materials depend on applied stress and temperature. Increased temperatures and severe plastic deformations are observed during the machining process. These two effects exist on surface and subsurface of the workpiece at different rates depending on cutting parameters and process design. Accordingly, the phase transformation properties and, in turn, functional behaviors are affected. Therefore, unlike other difficult-to-cut materials such as aero engine alloys, post manufacturing functional properties of these alloys should also be considered.

Energy-assisted machining methods such as electro discharge machining (EDM) [51], laser machining, and femtosecond laser machining (FSM) [52, 53] are other shaping processes employed in the manufacture of NiTi. However, thermal damage and heat affected zone (HAZ) were reported as potential disadvantages of these processes. Furthermore, their 3D shaping capabilities are limited. Considering the shaping capabilities of conventional methods on complex geometries and some limitations of unconventional machining methods, conventional machining methods seem like the most viable methods for the machining of NiTi SMAs [46, 49, 54]. The main aim of this work is to review the effects of various machining parameters, cooling lubrication conditions, and cutting tools on the machinability and functional characteristics of NiTi SMAs during contact type machining processes. Major results of alternative machining methods such as EDM, FSM, abrasive water-jet machining (AWJ), and pure water-jet machining (PWJ) are also briefly addressed.

This paper presents developments and findings in the machining of NiTi alloys over the last 20 years. Considering very distinct machinability characteristics of NiTi, results of the reported studies are discussed in detail. In order to ensure a better understanding in machinability of NiTi, following are aimed:

- Review and discussion of cutting tool materials for machining NiTi
- Review and assessment of tool wear mechanisms and wear modes
- Comparison of machining responses to varying machining parameters
- Causes, effects, and behavior of machining induced phase transformation

- Effects of machining on functional properties
- Discussion of suggested machining concepts to increase machinability

2 Tool materials for machining NiTi

In the last century, foremost improvements in the rate at which various materials are machined generally resulted from development and application of new tool materials. These tool materials include coated carbides (various types of coatings), ceramics, cubic boron nitride (CBN), and polycrystalline diamond (PCD). These tool materials have yielded very satisfying results, when machining hard-to-machine materials such as stainless steel, super alloys, and titanium alloys, provided suitable cutting conditions and cutting parameters are applied. Although machining behaviors of NiTi resemble nickel-based superalloys like Inconel 718 (mostly studied super alloy) or titanium alloys like Ti6Al4V (mostly studied titanium alloy), not many of these tool materials found applications in machining of NiTi. The main reasons for this limitation are probably the unique stress–strain and machining-induced phase transformation behaviors of NiTi.

The ultimate selection of the cutting tool material is based on the ability of the cutting tool to maintain its hardness, toughness, and chemical stability at high temperatures [55]. Similar to high-temperature alloys (above described nickel-based superalloys and some titanium alloys), very high cutting temperatures concentrated near the tip of the cutting tool were observed when machining NiTi. The main reasons of this heat concentration are low thermal conductivity and relatively high specific heat of the material. Although mechanical properties of NiTi and austenitic stainless steel are similar [44], machinability characteristics of NiTi are very poor compared to that of austenitic stainless steel. One of the main reasons of this difference is thermal properties of NiTi.

There are many studies available on performances of various cutting tool materials when machining nickel-based super alloys and titanium alloys. However, present knowledge in the machinability response of NiTi to these tool materials is very limited. Regarding the main limitations and their causes in the machinability of NiTi, nickel-based superalloys and titanium alloys yielded similar results to NiTi according to present works in the literature. Since the available data from these studies covers a very large span, improvements in the machining of NiTi may be ensured by analogy. In Table 2, mechanical and thermal properties of Inconel 718, Ti6Al4V alloy, and two phases of NiTi are presented. In this section of the paper, a very brief review of available cutting tool material performance data when machining nickel-based super alloys, titanium alloys, and NiTi SMAs is conducted. An easier understanding of cutting tool effects in machinability of NiTi is aimed.

Table 2 Some selected mechanical and physical properties of Inconel 718, Ti6Al4V, and equiatomic NiTi at room temperature

	Inconel 718 [56, 57]	Ti6Al4V [56]	NiTi [58, 59]	
			Austenite	Martensite
Nickel content (wt.%)	50–55	–	55	
Titanium content (wt.%)	1	89	45	
Other elements	Cr, Fe, Co	Al, V	–	
Density (kg m^{-3})	8190	4420	6450	
Ultimate tensile strength (MPa)	1240	930	895	
Yield strength (MPa)	1036	885	195–690	70–140
Elastic modulus (GPa)	211	114	83	28–41
Hardness (Hv)	370	320	290	220
Melting range/point ($^{\circ}\text{C}$)	1260–1336	1649	1310	
Specific heat ($\text{J kg}^{-1} \text{K}^{-1}$)	435	560	837	
Average coefficient of thermal expansion ($\mu\text{m m}^{-1} \text{K}^{-1}$)	13	8.6	11	6.6
Thermal conductivity ($\text{W m}^{-1} \text{K}^{-1}$)	11.4	7.2	18	8.5

Being the oldest among the hard cutting tool materials (harder than high speed steel), tungsten carbide tools (WC) have been proven their superiority in almost all machining processes of nickel and titanium alloys [60]. Composition and microstructure have a strong influence on performance of carbide tools. Commercial WC tools contain binder phase of cobalt in the range of 3 to 12% and the carbide grain size of these tools vary from 0.5 to 5 μm . Generally, increase of grain size or cobalt content results in decreased abrasion resistance and increased fracture toughness [55]. One drawback of carbide tools is its low thermochemical stability. Generally, at temperatures above 700 $^{\circ}\text{C}$, carbide tools fail due to thermal softening of the cobalt phase and subsequent plastic deformation of the cutting edge [61]. Studies showed that the maximum temperature at the tool–chip interface can reach as high as 1300 and 1000 $^{\circ}\text{C}$ when machining nickel alloys [62] and titanium alloys [63], respectively. As a result, with the currently available carbide tools, it does not seem possible to cut NiTi at high cutting speeds ($V_c > 100$ m/min).

Chemical vapor deposition (CVD) and physical vapor deposition (PVD) coated carbides were developed to optimize toughness and hardness of the cutting tool. Their development rendered possible to machine difficult to cut materials at higher cutting speeds with reduced tool wear. Furthermore, lower cutting forces and lower cutting temperatures were observed owing to lower coefficient of friction and higher thermal conductivity of these coating materials [64]. PVD method is much more preferred for carbide tools, because the PVD process employs lower temperatures than CVD process. Lower deposition temperature provides refinement of the grain size of the coating layer by preventing *nphase* formation [55]. Formation of *nphase* and/or residual stress in CVD coatings decreased transverse rupture of carbide tools by as much as 30% compared to PVD coatings [55, 65]. Turning

experiments of Inconel 718 showed that multilayer PVD coated carbide inserts showed longer tool life and better abrasion resistance compared to multilayer coated CVD carbide inserts [66]. Similar behaviors are expected when machining NiTi.

It was reported that cutting speeds above 30 m/min resulted in increased tool wear when drilling NiTi with carbide tools [45]. Wear analysis of TiCN/TiAlN multilayer PVD coated carbide tools showed that, at cutting speed of $V_c = 100$ m/min, minimum wear was observed when turning NiTi [42, 67]. However, TiB₂-coated carbide tools showed high flank and crater wear rate due to tribo-chemical dissolving of the TiB₂ coating. Using TiN-coated carbide drills ensured no advantage over uncoated carbide drills regarding tool wear [42]. When machining nickel-based super alloys with carbide tools, results were very similar to machining of NiTi with carbide tools. Cutting speed values between 50 and 90 m/min [68–70] and 25–50 m/min [70, 71] were suggested to obtain best tool life when machining with PVD-coated and PVD-uncoated carbide tools, respectively. When drilling Ti6Al4V alloy with coated and uncoated carbide tools, results showed that uncoated carbide drills outperformed TiAlN-coated carbide drills at cutting speed values up to 50 m/min [72]. Cutting speeds up to 150 m/min was successfully applied in high speed milling of Ti6Al4V alloy with PVD-coated carbide tools [73].

The introduction of super hard cutting tool materials has enabled higher cutting speeds to be achieved when machining nickel and titanium alloys. These materials principally include ceramics, CBN, and PCD tools. Even though these materials maintain their high hardness at increased temperatures, their mechanical and thermal shock resistance are quite low. Therefore, application parameters (i.e., workpiece material, machining parameters, etc.) should be carefully studied when employing these cutting tool materials. A brief review of the properties of different tool materials is shown in Table 3.

Table 3 Properties of different tool materials [74–77]

Material property	Tool material						
	Tungsten carbide (K10) (94% WC + 6% Co)	Alumina (90–95% Al ₂ O ₃ + 5–10% ZrO ₂)	Mixed alumina (Al ₂ O ₃ + 30% TiC + 5–10% ZrO ₂)	Whisker reinforced alumina (75% Al ₂ O ₃ + 25% SiC)	SiAlON (77% Si ₃ N ₄ + 13% Al ₂ O ₃ + 1% Y ₂ O ₃)	CBN (50–90% CBN + 50–10% TiN-TiC)	PCD (90% PCD + 10% Co)
Grain size (μm)	0.5–5	1–2	1–2		1	1–3	1–5
Density (g cm ⁻³)	14.8	3.9–4.0	4.2–4.3	3.7	3.2	3.1	4.12
Hardness (Hv) at 20 °C	1700	1700	1900	2000	1600	3000–4500	6000–10,000
Hardness (Hv) at 1000 °C	400	650	800		900	1800	
Fracture toughness (MPa m ^{-1/2})	10	1.9	2	8	6	9–11	6–8
Young's modulus (KN mm ⁻²)	630	380	420	390	300	680	1050
Thermal conductivity (W m ⁻¹ K ⁻¹)	100	8–10	12–8	32	23	100	540
Coefficient of thermal expansion (10 ⁻⁶ K ⁻¹)	5–6	8–10	8		3.2	5	4–5

Ceramic tools provide desirable tool behaviors such as high hardness, high hardness at increased temperatures, and chemical inertness (in most applications). However, their fracture toughness and thermal conductivity are much lower than carbide tools. There are three types of ceramics employed as cutting tools. These are aluminum oxide ceramics (Al₂O₃), whisker-reinforced alumina ceramics (Al₂O₃ + SiC_w), and SiAlON ceramics (S₃N₄ + Al₂O₃). Investigations showed that nickel-based superalloys can be machined with ceramic tools at the speeds of the order of 250–500 m/min with minimum tool wear [78–80]. Thus, they have replaced carbide tools in many applications in machining of nickel-based alloys. Conversely, when machining titanium alloys, ceramics have not yielded favorable results. This originates from their poor thermal conductivity and reactivity with titanium [60]. However, ceramics can machine titanium at high speeds provided their thermal conductivity and chemical compatibility with titanium alloys are improved [81]. Yet, there is no commercially available ceramic tool available for machining titanium. Machinability of NiTi was investigated using Al₂O₃ and mixed ceramics (Al₂O₃ + TiC) [82]. It was reported that investigated ceramic materials were not capable of machining NiTi. Whisker reinforced ceramics might yield better results, as they possess higher thermal conductivity and higher fracture toughness compared to oxide ceramics.

Ultra-hard cutting tool materials (CBN and PCD) showed good performance when machining nickel and titanium alloys. Being the hardest material after diamond, CBN cutting tools are employed in machining of various difficult-to-cut materials such as surface-hardened steels and irons, nickel-based superalloys, and titanium alloys. Compared to ceramics, CBN tools display better fracture resistance and higher thermal conductivity, which are the major limitations of ceramic tools. CBN tools are generally composed of 50–90% CBN and ceramic binders, such as TiC or TiN. The main limitation of these tool materials is their high cost. However, it was reported that machining of nickel-based super alloys with CBN tools in an economic manner may be possible considering the increased material removal rate [74, 75, 82].

Machining of Inconel 718 with CBN tools between cutting speeds of 300–350 m/min yielded positive results regarding cutting forces [83], surface quality [83, 84], tool life [85, 86], and residual stress formation [84]. Furthermore, compared to ceramic cutting tools, lower tensile residual stress formation was observed when machining Inconel 718 with CBN tools [87]. When machining Ti6Al4V with CBN cutting tools, cutting speed values of the order of 200–250 m/min resulted in favorable results regarding tool life with no additional surface deterioration, compared to carbide tools [88–90]. Binderless CBN tools (with no binder phase or sintering agent) displayed superior tool life when machining titanium alloys [91, 92]. This result probably originated from improved mechanical and thermal properties of binderless CBN compared to regular

CBN tools. When machining NiTi with CBN cutting tools (90–95% CBN, 5–10% cobalt), higher tool wear was observed compared to carbide tools [82]. It should, however, be noted that the machining was conducted under the same cutting speed for both cutting tool materials. Considering the high-temperature hardness of CBN tools, higher cutting speeds might yield less tool wear due to thermal softening of the workpiece.

PCD cutting tools are made from diamond, which is the hardest material known. In addition to superior hardness, PCD cutting tools exhibit very high values of thermal conductivity and exceptional wear resistance. PCD tools, however, react with ferrous metals at moderate temperatures and they are subjected to graphitization. Therefore, they can only be used for machining non-ferrous materials such as aluminum and its alloys, titanium alloys, copper, granites, composites, ceramics, and tungsten carbide. Studies showed that when machining Ti6Al4V alloy with PCD tools, compared to carbide tools, threefold increase in tool life, better surface finish, less chatter, and higher material removal rate (MRR) was observed [93, 94]. Regarding cutting speed, optimal value was reported between 180 and 250 m/min for turning [95] and milling [96] processes. These positive results even at high cutting speed values, most probably originated from higher thermal conductivity and extreme hardness of PCD. This is because, when machining titanium, the main problem is high chemical reactivity of titanium at elevated temperatures. It was reported that the use of PCD (92% PCD, 8% cobalt binder) cutting tools, when machining NiTi, led to high notch wear formation [82].

3 Tool wear

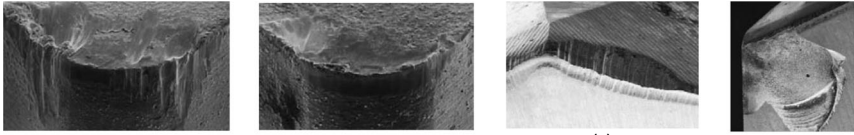

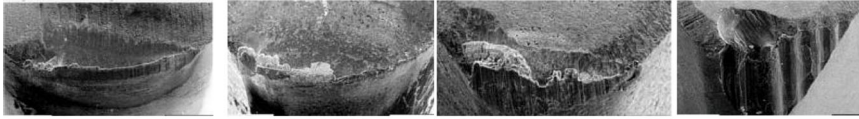
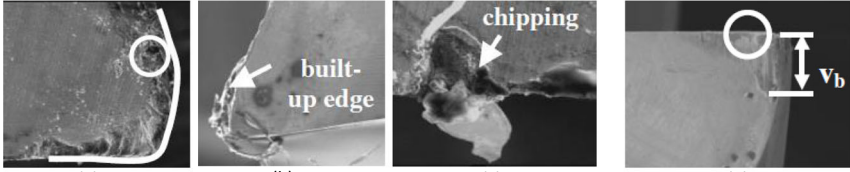
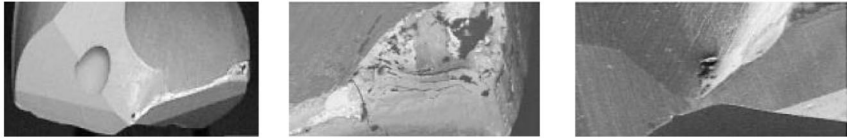
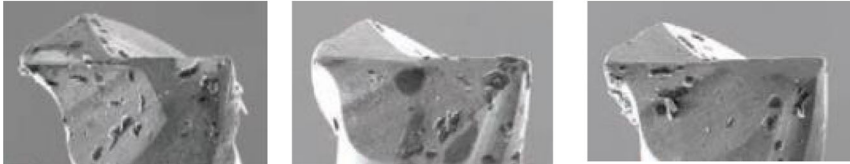
During the machining process, especially when machining difficult-to-cut materials, it is normal to observe tool wear, which originates from cutting action and friction at tool–chip and tool–workpiece interfaces. However, tool wear is a gradual process and excess of it causes tool failure and, unfortunately, it cannot be accurately predicted using present analytical models. In order to control and understand tool wear process, proper tool wear monitoring is vital to understand tool wear behaviors of certain cutting conditions. Flank and crater wear are the most important measured forms of tool wear, while flank wear criterion is most commonly used for wear monitoring [97].

Tool wear is one of the major concerns in the machinability of difficult-to-cut materials because it not only affects the productivity of the process but also influences the overall quality of finished parts. Negative effects of rapid tool wear on overall machinability performance may be listed as follows: (1) need for frequent tool change which results in increased tool cost and increased machining time, (2) increased cutting force and subsequent increased energy consumption [98], (3) increased

cutting temperature, (4) dimensional inaccuracy, and (5) negative impacts on surface integrity characteristics (residual stress formation, surface degradation, altering of micro structure). Due to increased cutting force and temperatures, tool wear progress accelerates. Furthermore, owing to its unique phase transformation characteristics, the subsurface zone of machined NiTi SMAs is severely affected from machining induced temperature and pressure variations [46, 50, 99]. Considering the application range of the NiTi, a better understanding of the tool wear process during machining gains even more importance because, in addition to surface integrity and dimensional accuracy issues, desired functional behaviors should also be of concern.

Tool wear is influenced by the rigidity of machine tool, cutting tool, and workpiece as well as thermal, mechanical, and chemical interactions among cutting tool, cutting environment, and workpiece. Rigidity and dynamic issues are out of scope of this paper and not discussed. Very high mechanical load on a relatively small area causes concentrated pressure on the tool tip. Together with that, chip flow on tool face and relative motion between cutting tool and workpiece initiate tool wear. Very high cutting temperatures at this region further accelerate physical and chemical processes related to tool wear. During machining of nickel and titanium alloys, observed wear mechanisms are abrasive wear, adhesive wear, diffusion wear, fatigue wear, oxidation wear, and debonding failure [100]. When machining NiTi, dominant wear mechanisms are adhesion and abrasion. Typical tool wear mechanisms and types that occurred during machining of NiTi are shown in Fig. 4.

When machining NiTi, mostly observed wear types were notch wear, flank wear, crater wear, edge breakage, and chipping. Notch wear, or V-shaped groove, at the depth of cut line is very common when machining titanium alloys [101] and nickel-based super alloys [102]. This wear type mainly originates from high temperature, high workpiece strength [103], and work hardening/fatigue hardening of the workpiece [44, 104]. Notch wear is the most dominant tool wear type observed in turning of NiTi [42, 82, 105, 106]. High specific heat combined with very low thermal conductivity results in concentrated temperature at tool edge. Concentrated temperature together with rapid strain hardening of NiTi are mainly responsible for this kind of wear. Notch wear may be minimized by using a tougher tool material, chamfering tool edge [107], altering cutting parameters [42], or using varying depth of cut strategy [108] if multiple passes are made. In the turning of NiTi with carbide tools, increasing cutting speed to $V_c = 100$ m/min resulted in reduced notch wear owing to reduced cutting forces [42, 82]. Cutting depth values smaller than tool nose radius led to decreased notch wear [42]. Alternatively, employing TiN-coated carbide tools significantly reduced notch wear [82]. When milling NiTi, increase of feedrate led to increased notch wear due to

Process	Tool	Workpiece material	Reference
Turning (a,b) Drilling (c,d)	TiCN/TiAlN multilayer coated carbide	β -NiTi	[43]
			
	(a) Flank wear, crater wear, notch wear, edge breakedge, adhesion (b) Flank wear, crater wear, adhesion (c) Chipping, edge wear (d) Flank wear		
Turning	TiB ₂ coated carbide	β -NiTi	[103]
			
	(a) Flank wear, notch wear, abrasion marks on flank face, chip flow damage (b) Adhesion, crater wear, edge fracture (c) Adhesion on rake face, notch wear, flank wear with abrasion marks		
Turning	(a)CBN (b)PCD (c)Mix Ceramic (d)Al ₂ O ₃ Ceramic	β -NiTi	[80]
			
	(a)Abrasion on rake face, adhesion, flank wear (b) Attrition wear, notch wear (c)Severe adhesion, edge breakage, abrasion, crater wear (d) notch wear, crater wear, flank wear		
Milling	Uncoated carbide end mill (\varnothing 10 – 4 teeth)	β -NiTi	[42]
			
	(a)Micro chipping and micro galling (b)Built up edge (BUE) (c) Microchipping and microgalling (d) flank wear, abrasion marks		
Drilling	TiCN/TiN coated carbide drill (\varnothing 5)	α -NiTi	[46]
			
	(a)Chipping, edge breakedge (overview) (b)flank wear, adhesion (cutting edge) (c)adhesion wear (drill centre)		
Micro milling	Fine grain carbide micro end mill (\varnothing 0.5)	α -NiTi	[104]
			
	(a)Chipping, flank wear, edge breakedge (b)Flank wear (c) Slight flank wear		

increased load [43]. Application of cryogenic cooling during machining NiTi was reported to yield very low notch wear compared to dry cutting and cutting with minimum quantity lubrication (MQL) [105]. This was attributed to reduced tool–chip contact length leading to reduced cutting force.

Crater wear occurs on the rake face of the cutting tool small distance from cutting edge, where the maximum tool temperature is observed. Very high temperature and pressure on this zone initiate the diffusion process and subsequent local removal of tool material forms crater. Hot chip flow over this

◀ **Fig. 4** A brief review of tool wear mechanisms and types in machining of NiTi. TiCN/TiAlN multilayer coated carbide (a) Flank wear, crater wear, notch wear, edge breakage, adhesion (b) Flank wear, crater wear, adhesion (c) Chipping, edge wear (d) Flank wear. TiB₂-coated carbide (a) Flank wear, notch wear, abrasion marks on flank face, chip flow damage (b) Adhesion, crater wear, edge fracture (c) Adhesion on rake face, notch wear, flank wear with abrasion marks; (a) CBN (b) PCD (c) Mix ceramic (d) Al₂O₃ ceramic. (a) Abrasion on rake face, adhesion, flank wear (b) Attrition wear, notch wear (c) Severe adhesion, edge breakage, abrasion, crater wear (d) Notch wear, crater wear, flank wear. Uncoated carbide end mill (Ø10—4 teeth) (a) Microchipping and microgalling (b) Built-up edge (BUE) (c) Microchipping and microgalling (d) Flank wear, abrasion marks. TiCN/TiN-coated carbide drill (Ø5) (a) Chipping, edge breakage (overview) (b) Flank wear, adhesion (cutting edge) (c) Adhesion wear (drill center). Fine grain carbide micro end mill (Ø0.5) (a) Chipping, flank wear, edge breakage (b) Flank wear (c) Slight flank wear

surface aids formation of the crater by abrasive wear mechanism. Although the progression of cratering to tool edge may cause catastrophic tool failure, generally the volume available to be worn away completely is much greater for crater wear than for flank wear. This is also valid for machining of NiTi (see Fig. 4). However, cratering should also be kept under control for NiTi. It is clear from Fig. 4 that crater wear together with abrasive marks are present on the rake face of the worn tools. Some of these craters grew in to edge breakage. It was reported that, when turning NiTi, employing TiB₂-coated carbide tools accelerated cratering due to tribo-chemical dissolving [82]. Probably, this process was followed by severe abrasion due to the very hard nature of the TiB₂ particles. Although application of cryogenic cooling was effective in reducing the crater formation, it was not as effective as reducing the notch wear on flank face [105]. Likewise, cratering was reported to be a severe problem during milling of NiTi [43].

Chipping along the cutting edge occurs when the cutting edge removes the chip intermittently like milling process. Intermittent removal of chip results in cyclic mechanical and thermal loadings on the cutting edge. These loadings are followed by small cracks called chipping. In turning process, the cyclic load occurs by rotation of shear angle when a tool exits a cut [109]. This kind of wear is more common in the milling of NiTi than turning. When milling NiTi, microchipping gradually occurred and led to tool failure [41]. Application of chilled air did not decrease chipping during micro end-milling of NiTi [110]. In this case, chipping might be originated by hardening of NiTi at low temperatures. Variation of inclination angle had a great influence on edge chipping during multi-axis micro end-milling [49]. As seen in Fig. 4, chipping was the dominant wear type when drilling NiTi [42, 45, 82, 111]. During deep hole drilling of NiTi, lower cutting speeds $V_c < 30$ m/min led to increased chipping due to increased strain hardening [54]. Increasing feedrate to $f = 0.03$ mm/rev resulted in decreased chipping during deep

hole drilling [42]. This probably originated from more stable chip formation due to increased chip thickness.

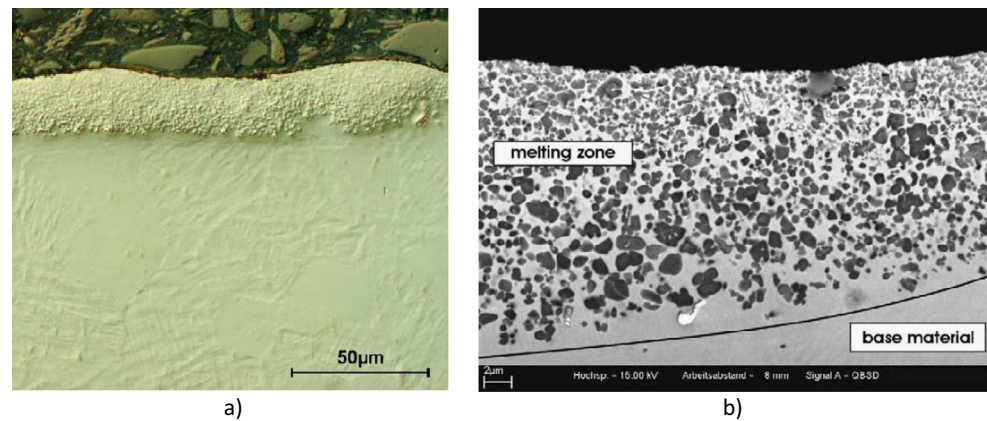
4 Machining operations

As stated in previous sections, machining of NiTi is very challenging due to high strain hardening, low thermal conductivity, high specific heat, and low effective elastic modulus. All these factors make dynamic mechanical properties of these alloys unique and lead to severe tool wear, high cutting forces, and poor chip handling. Gou et al. conducted both quasi static and Split Hopkinson pressure bar compression test of Ni_{50.8}Ti_{49.2} (at.%) under the strain rate of between 2600 and 6400 s⁻¹ [43]. Results showed that ultimate compressive stress (UCS) reached up to 3 GPa under moderate strain rate values, while this value was around 2.3 GPa in quasi-static compression test. UCS decreased to 1.6 GPa and failure plastic strain reached up to 0.2 under higher strain rates due to adiabatic shearing. These unique thermo-mechanical behaviors indicate that NiTi is very difficult to machine. A well-conducted review of experimental studies is required since complex thermo-visco-elasto-plastic behaviors of this material under machining conditions still cannot be predicted with present methods.

4.1 Non-conventional machining

Depending on the properties of desired product, non-conventional machining methods may be good alternatives to tool-based traditional machining methods. Some researchers suggested non-contact type machining methods (non-conventional methods) such as EDM, FSM, AWJ, and PWJ; however, there are some limitations with these machining methods. Huang et al. reported that HAZ underneath the machined surface (50–150 μm) was observed in energy-assisted machining methods of EDM and FSM [53]. HAZ formation may locally change transformation temperatures and microstructure of NiTi components. Subsurface hardening was another unfavorable result reported in EDM with a minimum depth value of 150 μm. Additionally, the FSM process resulted in severely granulated texture (around 10 μm deep), probably due to recasting, and formation of a recast layer with combination of hot and ablated particles. It was also reported that during laser machining of narrow grooves, evaporated material may not evacuate cutting zone and recast to back to cut wall. Similar results were reported by Theisen and Schuermann [51]. They reported HAZ formation range of between 5 and 22 μm depth during EDM. In addition to HAZ, TiC precipitation, melting drops as well as discharge craters with cracks were also observed as shown in Fig. 5. The subsurface hardening effect was observed in other studies using EDM [112] and FSM [113].

Fig. 5 Limitations when cutting NiTi using EDM. **a** Melting drops. **b** TiC precipitates in melting zone [51]



AWJ and PWJ are promising methods as they cause little (AWJ) or no (PWJ) thermal distortion [114]. These methods may even be candidates for simple milling operations if controlled-depth milling is ensured [115]. Frotscher et al. investigated feasibility of water jet cutting of biomedical NiTi sheet [116] and they found that cutting quality was not good enough. Kong et al. investigated PWJ and AWJ methods through an analysis of controlled-depth milling of NiTi SMA [47]. They reported that the main limitations were non-homogenous depth, inaccurate milling depth, and flat surface in PWJ. The major reason of these occurrences was low yield strength and high strain hardening of the martensite as this process was conducted in 100% martensitic state with no temperature-induced phase change. It was reported that AWJ machining may be a better solution for controlled milling because the abrasive erosion resistance of austenite phase is lower considering the fact that temperature-induced austenitic transformation is expected in AWJ [117]. However, this process was unable to yield as-milled-like surfaces due to scallop-shaped footprint between passes as seen Fig. 6.

These results showed that non-contact type machining methods may be used in production of NiTi parts if

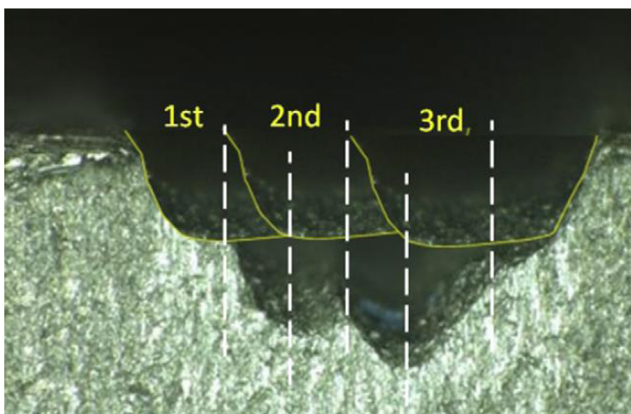


Fig. 6 Demonstration of first and subsequent jet footprints when attempting to ensure controlled depth milling with AWJ [47]

dimensional and surface characteristics of the part allow the above summarized limitations. However, as pointed out by Kong et al. [47], cutting quality for high-value industrial applications remains a challenge. Contact type machining methods remain an important goal considering the prevalence and well-proven capabilities of them. Applications of these for NiTi are reviewed in the following subsections.

4.2 Turning

Although NiTi SMAs were discovered around the 1950s, first machinability study in turning process was conducted at the beginning of the 2000s. A brief review of turning studies of NiTi and the consequences are briefly presented in Table 4. Weinert and Petzoldt investigated machinability characteristics of a Ni_{50.9}Ti_{49.1} SMA (at.%) in turning process [42]. The sample was in the austenite phase at room temperature (heat treated by annealing at 850 °C in the air for 20 min and water-quenched afterwards aged at 350 °C for 60 min and quenched in water again). The cutting insert was TiCN/TiAlN multilayer-coated cemented carbide with geometry of CNGG 120402 ($\alpha_o = 6^\circ$, $\gamma_o = 7^\circ$) according to ISO classification. In all cutting tests, dry and lubricated conditions were investigated (lubricant of 5% coolant, 95% water emulsion). Effects of cutting speed were investigated between $V_c = 20$ and 180 m/min ($f = 0.05$ mm/rev and $a_p = 0.2$ mm). High cutting forces (above 170 N) with severe notch wear and poor chip breaking were observed between cutting speed range of $V_c = 20$ and 60 m/min. In the second range between cutting speed of $V_c = 60$ and 130 m/min, minimum cutting forces (about 50 N), minimum tool wear (no notch wear at about $V_c = 100$ m/min), minimum chip breaking problem, and least burr accumulation were reported. Cutting speeds above $V_c = 130$ m/min resulted in increased cutting force and tool wear (especially in dry cutting conditions). This was attributed higher friction due to elevated cutting temperatures. The effects of varying cutting speed on cutting forces and tool wear are shown in Fig. 7. Effect of feed rate was investigated

Table 4 A brief review of studies conducted on turning of NiTi SMA's

Reference	Material composition	Phase (room temperature)	Cutting condition, Fabrication method	Tool material	Tool geometry
[42]	Ni50.9Ti49.1 (at. %)	Austenitic	FloodingDry	Carbide multilayer coated	CNGG 120402
[105]	Ni49.9Ti50.1 (at. %)	Martensitic	Dry MQLCryogenic	Coated carbide	DCGT 11T308HP
[106]	Ni49.9Ti50.1 (at. %)	Martensitic	PreheatedCryogenic	Coated carbide	DCGT 11T308HP
[82]	Ni50.8Ti49.2 (at. %)	AusteniticAusteniticMartensitic	Wet	Ceramics CBN PCD	
	Ni50.9Ti49.1 (at. %)			Coated carbide	
	Ni50.3Ti49.7 (at. %)			Uncoated carbide	
[118]	Ni50.8Ti49.2 (at. %)	Austenitic	VAR VIM + VAR HR + full anneal CW + superelastic heat treatment	Coated carbide	DCGT 11T308HP
[119]	Ni50.8Ti49.2 (at. %)	Austenitic	Dry MQLCryogenic	Coated carbide	DCGT 11T308HP
[50]	Ni55.8Ti44.2 (wt. %)	Austenitic	DryCryogenic	Coated carbide	TPGN 220412
[120]	Ni55.8Ti44.2 (wt. %)	Austenitic	DryCryogenic	Coated carbide	TPGN 220412
[121]	Ni49.9Ti50.1 (at. %)	Martensitic	PreheatedCryogenicDry	Coated carbide	DCGT 11T308HP
[122]	Ni49.9Ti50.1 (at. %)	Martensitic	PreheatedDry MQLCryogenic	Coated carbide	DCGT 11T308HP

Reference	Cutting parameters	Remarks
	V_c (m/min) f (mm/rev) a_p (mm)	
[42]	20–180 0.05–0.15 0.2–0.5	Problems: high notch wear, flank wear, poor chip breakage, high burr formation Results: good chip breakage when $V_c < 40$ m/min. Minimum tool wear, burr formation, and cutting force when $V_c = 80$ –120 m/min, $f = 0.06$ –0.1 mm/rev. Minimum subsurface hardening at $V_c = 160$ m/min
[105]	12.5–100 0.05 0.5	Problems: Severe tool notch wear, adhesion, poor chip shape, and breakage Results: Severe tool wear in dry and MQL when $V_c > 25$ m/min. Minimum tool wear, cutting forces, and optimal chip handling achieved in cryogenic cutting as concluded that workpiece was kept in martensite structure with cryogenic cooling
[106]	12.5–50 0.1 0.5	Severe tool wear in preheated machining $V_c > 12.5$ m/min. Acceptable tool wear in cryogenic machining under all cutting speed values. Cutting forces were slightly lower in cryogenic machining. Cooling/heating concept did not affect chip thickness
[82]	20–100 0.035–1.0 0.2–0.3	Coated carbides outperformed uncoated carbides regarding tool wear. TiB ₂ coating increased tool wear. Ceramic tools were not capable of machining. PCD tool lead to sudden breakage. High wear was observed in CBN tool
[118]	25 0.05 0.5	Compared to VIM, VIM + VAR led to increased tool wear due to TiC inclusions. Compared to CW + superelastic heat treatment, increased tool wear was observed when HR + full annealing applied. This resulted from increased work hardening due to ductility
[119]	12.5–50 0.05 0.5	Narrower B2 peaks were observed at higher cutting speeds. Compared to dry and MQL cutting, broader B2 peaks were observed in cryogenic cuttings. Even, there were B19' peaks in cryogenic cutting at lower speeds
[50]	6.25–100 0.05	Deeper machining-induced layer and hardened layer were observed at lower cutting speeds. Compared to dry cutting, deeper machining induced layer and hardened layer was observed in cryogenic cuttings. Post machining, DSC results showed that cryogenic machining and/or low cutting speeds led to reduced volume of transformed material (changes in phase transformation properties)
[120]	6.25 0.05	According to TEM analysis, compared to dry machined samples, significantly higher density of deformation twins and greater dislocation density in the cryogenically machined specimens were reported. Contribution of twinning to the overall plastic deformation of the martensite phase was higher than that of the austenite phase
[121]	12.5–100 0.05 0.5	According to XRD analysis, austenite to martensite transformation is not complete after machining. This effect was more pronounced in dry cutting and cutting at higher cutting speeds. Transformation temperatures of cryogenically machined samples shifted significantly
[122]	12.5–100 0.05 0.5	Role of active phase during machining of NiTi investigated. Temperature measurements showed that workpiece was in austenitic state under dry, MQL, and preheated condition, but in martensitic state under cryogenic cutting

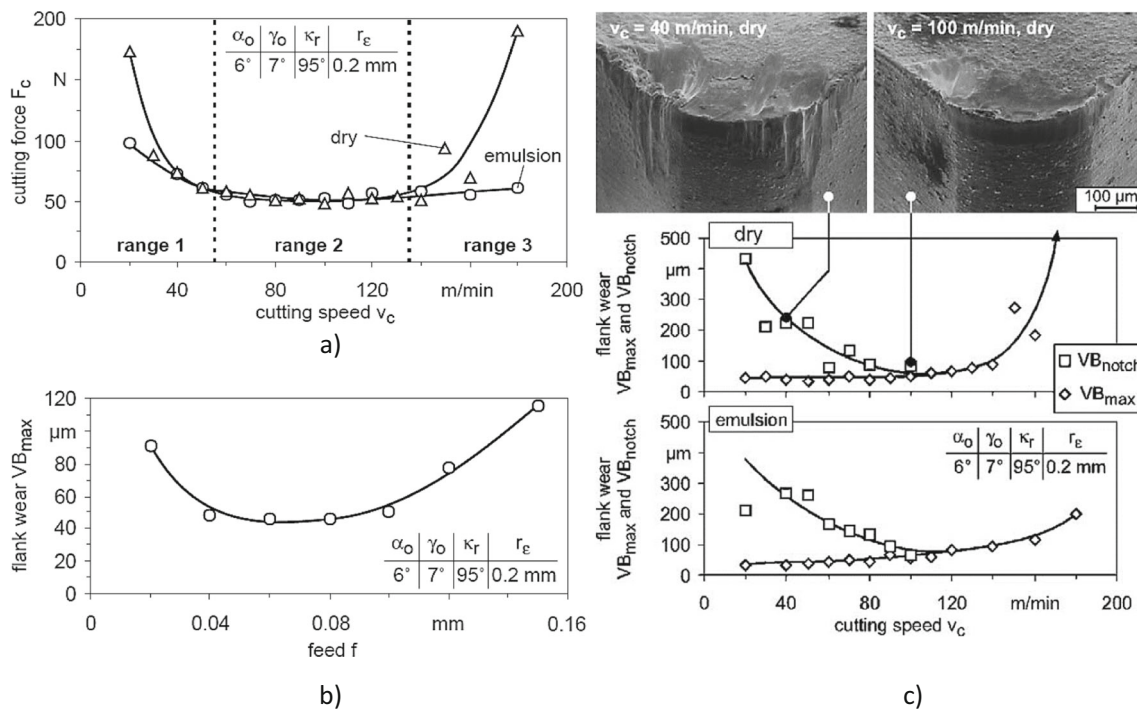


Fig. 7 Effects of varying cutting parameters on tool wear and cutting forces: **a** cutting speed against cutting force; **b** feedrate against flank wear; **c** cutting speed against flank wear [42]

between $f = 0.02$ and 0.15 mm/rev ($V_c = 100$ m/min, $a_p = 0.2$ mm, dry cutting). At low feed rate values ($f < 0.04$ mm/rev), high tool wear as well as the formation of burr was observed. The minimum tool wear and burr formation were observed between feed range of $f = 0.04$ and 0.09 mm/rev (see Fig. 7b). The reduction of burr formation was attributed to increased chip thickness resulting from increased feed values. The researchers also conducted experiments for various depth of cut values and concluded that cutting depth should be chosen around nose radius value of the insert for minimum tool wear and maximum productivity. However, it should be noted that the reported wear was measured using constant removal volume. As a result, lower values down to $a_p = 0.1$ mm led to increased tool wear due to increased contact length (increased feed rate).

Lubrication is a very important concept in machining, especially in difficult-to-cut materials. Presence of lubrication reduces friction, abrasion, and adhesion at the tool–chip interface. This ensures lower wear rates and cutting forces [123]. Cryogenic cooling can be implemented in machining process (cryogenic machining) to improve all major surface integrity and machinability characteristics. Cryogenic machining was reported to yield positive results in nickel-based super alloys [124] and titanium alloys [125]. Conversely, according to Hong et al., cryogenic cooling resulted in increased force components in the machining of Ti6Al4V alloy due to low cutting temperatures which makes workpiece stronger and harder [126]. Kaynak et al. examined various machinability

characteristics of $Ni_{49.9}Ti_{50.1}$ (at.%) alloy (martensitic at room temperature) under cryogenic cooling (liquid N_2 , $P = 1.5$ MPa, $\dot{m} = 10$ g/s), MQL ($P = 0.4$ MPa, $Q = 60$ ml/h), and dry cutting conditions in tuning process [105]. The cutting insert was TiB_2 -coated carbide with geometry of DCGT 11T308HP. During the experiments, a constant feed rate $f = 0.05$ mm/rev, constant depth of cut $a_p = 0.5$ mm, and variable cutting speed values $V_c = 12.5, 25, 50, 100$ m/min were used. The cutting experiments resulted in the abrasion dominant wear mechanism and wear modes of notch wear, flank wear, and crater wear. It was also reported that in dry and MQL conditions, chip flow damage played a major role in accelerated notch wear. Increasing cutting speed beyond $V_c = 25$ m/min and 50 m/min yielded unfavorable tool wear results for dry and MQL, and cryogenic conditions, respectively. In progressive tool wear tests (five measurements with cutting time of 1-min intervals, $V_c = 25$ m/min, $a_p = 0.5$ mm, $f = 0.05$ mm/rev), cryogenic condition yielded longest steady-state results with least overall tool wear. Besides, adhesive wear was observed in dry and MQL condition (no adhesion in cryogenic cooling). Most severe and deepest notch wear and flank wear was observed in dry machining condition. The main cutting forces, at $V_c = 25$ m/min, were also in agreement with tool wear rates, being lowest in cryogenic cutting (80 N) and highest in dry cutting (160 N) conditions (see Fig. 8a). Reported surface roughness values, at $V_c = 25$ m/min, were 1.2, 0.6, and 0.4 μm for dry, MQL, and cryogenic cutting conditions, respectively. It was reported that the recorded

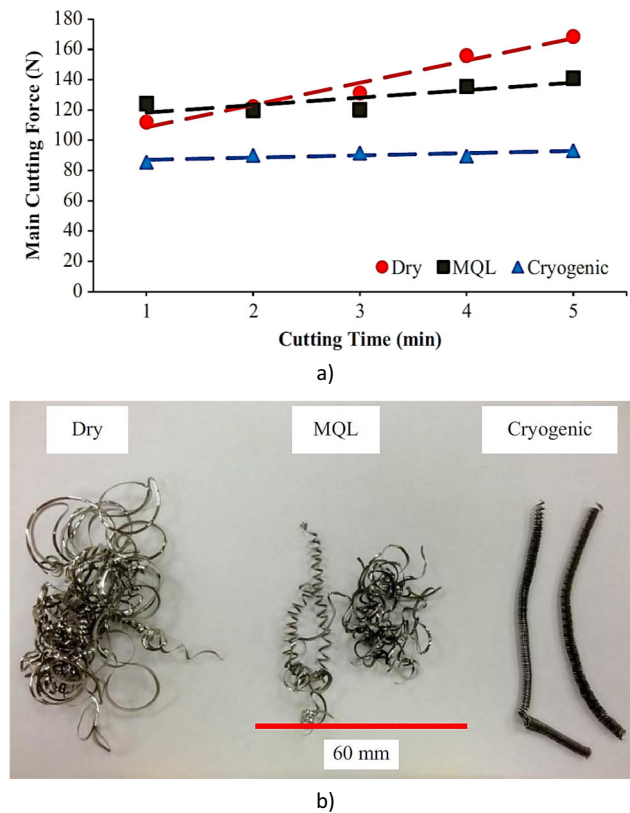


Fig. 8 Comparison of dry, MQL, and cryogenic cutting results: **a** cutting force vs. cutting time; **b** generated chip shapes [105]

maximum temperature during dry, MQL, and cryogenic cutting was 523, 259, and 96 °C, respectively. Considering the high pressure in cutting region, it can be inferred that shear process was ensured in martensitic state, in which strength of the material is relatively low, in cryogenic machining. Conversely, during dry and MQL conditions, probably, the alloy was a B2 order compound. DSC analysis of the generated chips supports this thesis. Accordingly, chip shapes generated from cryogenic cutting was more favorable compared to MQL and dry cutting as seen in Fig. 8b. It was concluded that cryogenic cooling yielded minimal tool wear and cutting force due shorter tool–chip contact length and active phase being martensite.

Preheated machining or hot machining is a method used for easing cutting process by aiming thermal softening of the workpiece. This method was reported to yield positive results when machining superalloys such as Waspalloy [127] and Inconel 718 [128]. Kaynak et al. [106] investigated the effects of temperature variation on the machinability behavior of Ni_{49.9}Ti_{50.1} (at.%) alloy through cryogenic and preheated machining processes (TiB₂-coated DCGT11T308HP geometry carbide insert; $V_c = 12.5, 25, 50$ m/min; $f = 0.1$ mm/rev; $a_p = 0.5$ mm; liquid N₂ cryogenic cooling at $P = 1.5$ MPa). The temperature of the workpiece, which was martensitic at room conditions, was increased to 175 °C (above A_f temperature)

during the preheating process. It was reported that wear was reasonable at low cutting speed of $V_c = 12.5$ m/min under both conditions. However, there was a large increase of notch wear in the preheated condition under $V_c = 25$ and 50 m/min. Moreover, chip flow damage was apparent in preheated machining, whereas it was eliminated in cryogenic machining. The increase of cutting speed resulted in decreased cutting forces in cryogenic machining. In preheated machining, however, the trend was uncommonly converse [129, 130]. In this case, increase of cutting speed resulted in increased cutting forces. This may be originated from increased tool wear. It was also reported that the machining conditions (preheated vs. cryogenic) did not have a significant effect on chip thickness [131]. Considering the active phase difference between cryogenic and preheated machining, this finding shows that chip thickness is not influenced by an active phase of the material.

Weinert et al. [82] investigated optimum cutting parameters and effects of various cutting tool materials in turning of NiTi SMA. The applied tool materials were uncoated carbide, various types of coated carbides, CBN, PCD, and ceramics. The results revealed that the coated carbides outperformed their uncoated couples in terms of resistance to wear. However, TiB₂ coating exhibited worse results compared to other coatings (TiN, TiAlN, TiCN). This may have resulted from chemical affinity between titanium and TiB₂. It was also reported that turning with PCD or CBN tools at the same cutting speeds with carbide tools ended up with higher tool wear rates. However, experimentation of higher cutting speeds ($V_c > 100$ m/min) might yield acceptable tool wear results with these tool materials because less adhesion has been reported at higher cutting speeds when machining with these ultra-hard cutting tool materials [132, 133]. As expected, composite and oxide ceramics were not suitable for machining of NiTi. This was most probably due to the chemical affinity between titanium and ceramics [60, 81]. The results showed that, at lower cutting speeds ($V_c < 60$ m/min), severe notch wear was observed. Increasing the cutting speed around $V_c = 100$ m/min ended up with decreased notch wear as well as increased surface quality. It was concluded that cutting depth values above the nose radius of the insert resulted in increased notch wear. The researchers also suggested a very novel approach by aiming to keep the material in B19' phase. Prior to machining, they cooled the workpiece with liquid N₂ to ensure temperature-induced forward phase transformation to martensitic structure; afterwards, they expanded the material with a mandrel. The stress applied by the mandrel from the inner diameter of the work piece causes stress-induced martensite. After this step, no further cooling was applied. With the application of this novel method, the workpiece can be kept in martensitic structure throughout the machining process.

Melting technique, prior processing, and heat treatment are substantial factors affecting mechanical and shape memory

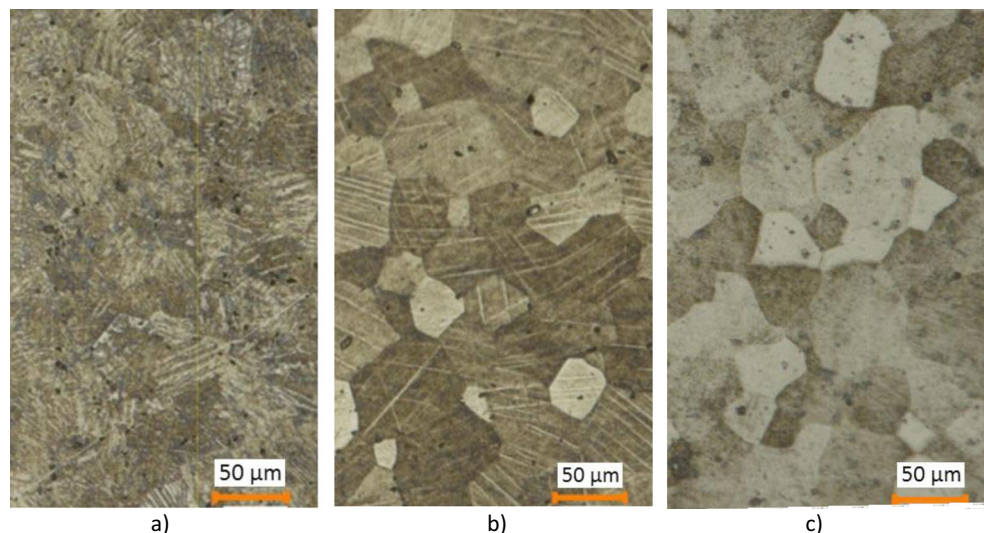
behaviors of NiTi [134, 135]. For example, hot worked and fully annealed material is expected to perform a ductile elongation. Therefore, these factors would also affect machinability of NiTi. Kaynak et al. investigated the influence of melting techniques (VAR vs. VIM combined with VAR (VIM + VAR)), prior processing (cold worked vs. hot worked), and heat treatment on the machinability performance of Ni_{50.8}Ti_{49.2} (at.%, B2 phase at room temperature) [118]. Cross-section microstructure images of the investigated specimens are displayed in Fig. 9. ISO code designation of DCGT11T308HP KC5410 cutting tool, with TiB₂ coating and having edge radius $r_e = 18\text{--}20\ \mu\text{m}$, was used in tests. Regarding cutting parameters, constant values of cutting speed $V_c = 25\ \text{m/min}$, feedrate $f = 0.05\ \text{mm/rev}$, and depth of cut $a_p = 0.5\ \text{mm}$ were used. Two cutting conditions were applied: (1) cryogenic (liquid N₂, $P = 1.5\ \text{MPa}$, $\dot{m} = 10\ \text{g/s}$) and (2) MQL ($P = 0.4\ \text{MPa}$, $Q = 60\ \text{ml/h}$). It was observed that hot rolled (HR) and the full annealed workpiece resulted in slightly increased flank wear compared to cold worked (CW) and superelastic heat-treated one. This was probably due to increased work hardening, which resulted from ductility of the material. Regarding melting method, VIM + VAR method yielded shorter tool life compared to VAR method. VAR method results in oxide inclusions, whereas VAR + VIM method results in both oxide and carbide inclusions. Therefore, the VAR + VIM method was detrimental to tool life, as TiC particles are harder and sharper than TiO₂ particles. According to [82], severe flank wear, crater wear, and relative short tool life observed in this study may be originated from TiB₂ coating.

Machinability responses of NiTi such as tool wear, cutting forces, surface roughness, chip breakage, chip shape, and burr formation of the conducted studies are reviewed in the previous paragraphs. Machining-induced subsurface microstructure and phase transformation behavior are of great

importance and should be taken into consideration because the functional performance of NiTi parts and operational safety closely rely on these factors. Considering the application range of these materials, such as biomedical and aerospace, these factors gain even more importance. Kaynak investigated phase transformation response of room-temperature austenitic ($M_s = -43\ \text{°C}$, $M_f = -71\ \text{°C}$, $A_s = -32\ \text{°C}$, $A_f = -11\ \text{°C}$) NiTi SMAs after turning process ($f = 0.05\ \text{mm/rev}$, $V_c = 12.5, 25, 50\ \text{m/min}$, $a_p = 0.5\ \text{mm}$) [119]. Cutting tests were conducted under cryogenic, MQL, and dry conditions. X-ray diffractometer (XRD) analysis of the machined samples was compared with as-received material, which showed the only B2 diffraction peak. Results showed that the broadest peak was observed at lowest cutting speed while the narrowest peak was observed at the highest cutting speed as shown in Fig. 10. At lower cutting speed values, cutting temperatures are lower than that at high cutting speeds. As a result, mechanical effect is more dominant than thermal effect [136]. Consequently, the stress-induced transformation broadened the peak. Conversely, at higher cutting speed values, increased temperatures suppressed mechanical effect by reducing dislocation density and stress. As a result, narrow B2 peaks were obtained. Compared to dry and MQL cutting, cryogenic cutting yielded broader B2 peaks. The B19' martensitic peaks were observed in cryogenically machined samples at low cutting speeds. These results suggest that the local martensitic structure took place after cryogenic machining due to induced stress to subsurface [119].

As stated previously, machining induced shape memory/superelasticity properties of NiTi need to be understood well. Kaynak et al. investigated cutting speed and cooling concept dependent phase transformation temperatures, transformation latent heat, and machining induced subsurface layer of room temperature austenitic Ni_{55.8}Ti_{44.2} (wt.%) SMA ($M_s = -14\ \text{°C}$, $M_f = -34\ \text{°C}$, $A_s = -8\ \text{°C}$, $A_f = 6\ \text{°C}$) [50].

Fig. 9 Microstructure of B2 NiTi fabricated with different methods: **a** VAR + cold work + superelastic heat treatment; **b** VAR + hot rolled + full annealed; **c** VIM + VAR + hot rolled + full annealed [118]



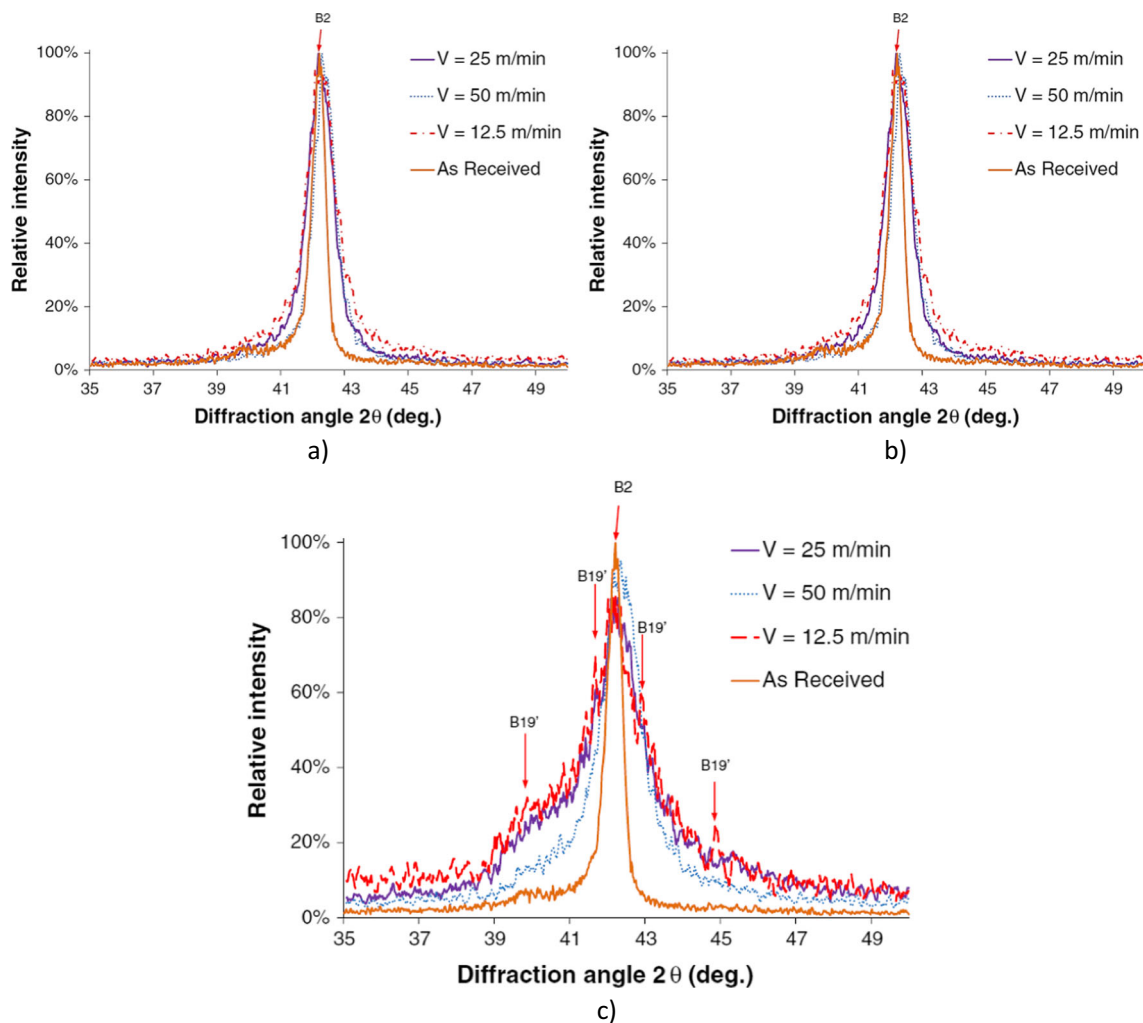


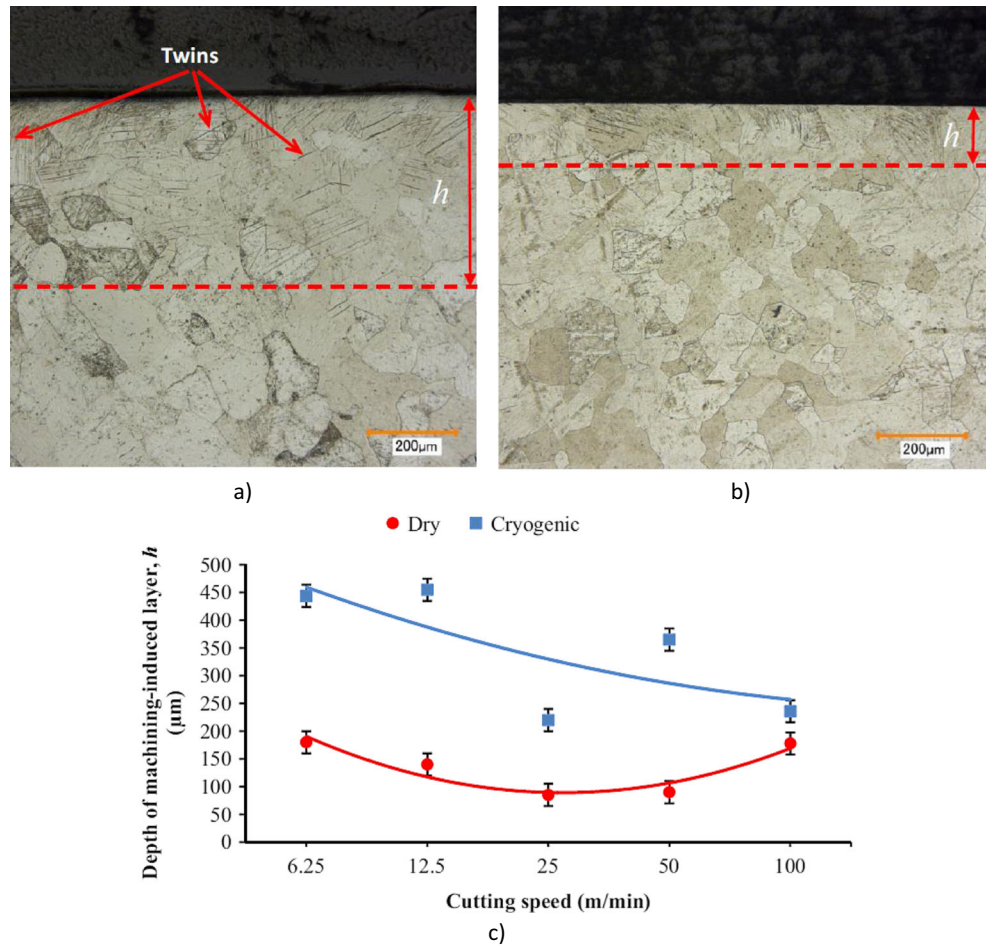
Fig. 10 XRD patterns of machined and as-received room temperature austenite NiTi samples: **a** dry machining condition, **b** MQL condition, **c** cryogenic condition [119]

Turning experiments were conducted under cutting speeds of $V_c = 6.25, 12.5, 25,$ and 50 m/min. Machining-induced layer (h) was examined using optical microscopy by measuring the depth of the regions with extensive twinning in the grains. Figure 11a and b shows the depth of the affected layer in dry and cryogenic machined sample at $V_c = 12.5$ m/min. It can be seen that depth of affected layer is much larger in cryogenically machined sample. Similarly, cutting speed had a direct effect on machining-induced layer. In both of the cutting concepts, increased cutting speed resulted in a decreased machining induced layer as seen in Fig. 11c. The reduced machining induced layer in dry cutting or high cutting speed was attributed to the dislocation annihilation effect of increased temperatures. Microhardness results were in good agreement with cross-sectional sample layer measurements as seen in Fig. 12. Increase of cutting speed resulted in decreased hardening and hardening depth. Similarly, compared to cryogenic cutting, dry cutting yielded lower hardness values and hardening depth because increased temperature at higher cutting

speeds in dry cutting led to reduced density of twins/dislocations and recovery of plastic deformation. DSC analyses were conducted to compare latent heat for transformation (ΔH) of cryogenically and dry machined samples with as-received sample. The results are displayed in Fig. 13. ΔH can be considered as the volume of transformed material. ΔH of the dry machined sample was remarkably higher than that of cryogenically machined sample, but lower than that of as-received material under all cutting speed values. Additionally, decreased cutting speeds led to decreased ΔH . These results show that application of cryogenic cooling and/or lower cutting speed lessen the transformed material volume during solid state phase transformation.

Transmission electron microscopy (TEM) analysis of dry and cryogenically machined austenitic NiTi was conducted for a better understanding of machining induced microstructure change [120]. Experimental procedure was identical to study reviewed above. In the study, TEM samples were cut from the surface region to investigate the affected layer. As

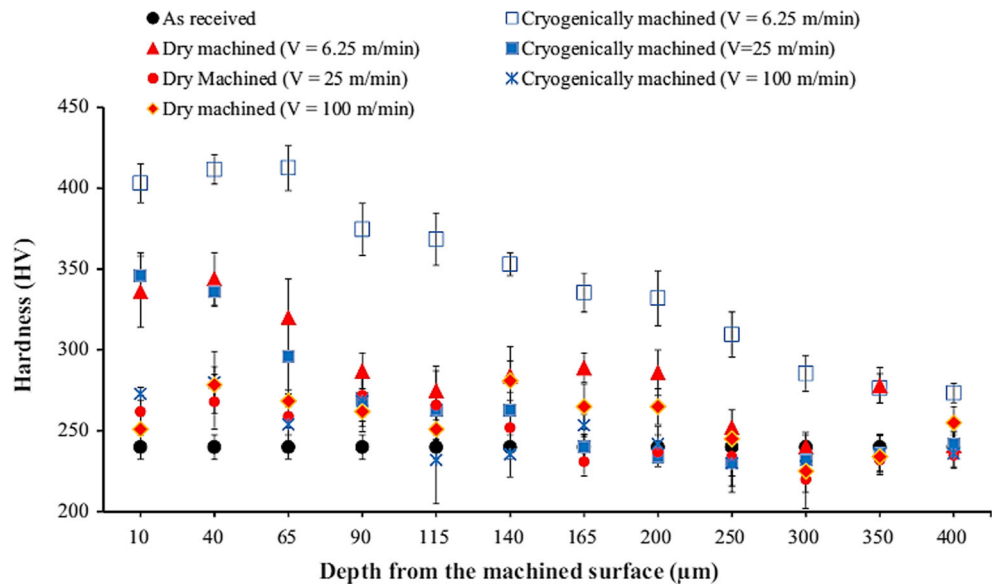
Fig. 11 Machining induced layers of room temperature austenitic NiTi. **a** Microstructure after cryogenic machining at $V_c = 12.5$ m/min. **b** Microstructure after dry machining at $V_c = 12.5$ m/min. **c** Maximum depth of machining-induced layer vs. cutting speed [50]



presented in Fig. 14a, TEM image of as-received material showed that it is in B2 phase. This was confirmed by selected area diffraction (SAD) pattern as seen in Fig. 14d. As presented in Fig. 14b, dry machining led to some deformation of twin

bands. It was reported that these twin bands were B2 compound twins [137], according to SAD patterns displayed in Fig. 14e. According to the bright-field micrograph of the cryogenically machined sample displayed in Fig. 14c, higher

Fig. 12 Effects of cutting speed machining condition on subsurface hardness and hardening depth [50] (here “ V ” denotes cutting speed)



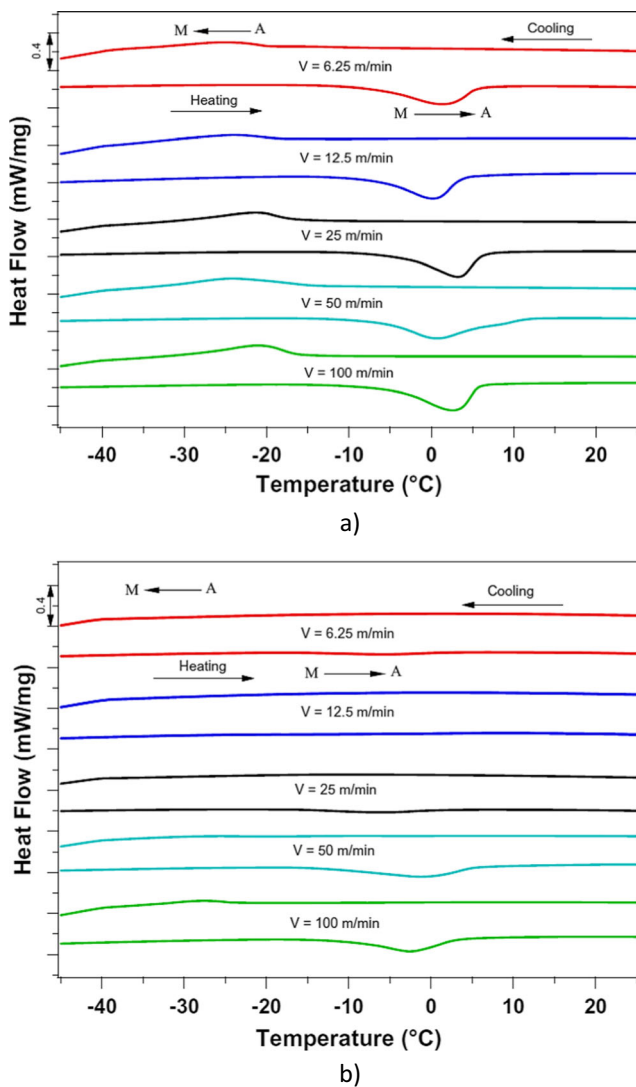


Fig. 13 DSC responses of room-temperature B2 alloys as a function of cutting speed after machining: **a** dry machining, **b** cryogenic machining [50] (here “V” denotes cutting speed)

density of twin bands were seen in this specimen compared to dry machined specimen. SAD pattern displayed in Fig. 14f indicated that the specimen was still fully austenitic [138]. According to this study, the contribution of twinning to the overall plastic deformation of the martensite phase was higher than that of the austenite phase [120]. This results in significantly higher density of deformation twins and greater dislocation density in the cryogenically machined specimens. This behavior is similar to results reported by Morawiec et al. [139]. They reported that martensitic phase transformation was hardly visible after rolling process induced deformation because of high density of dislocations and vacancies in the crystal structure of the material [140].

In the previously mentioned studies, machining-induced phase transformation characteristics of room-temperature austenitic NiTi SMAs were reviewed. Yet, these

characteristics need to be also addressed for room-temperature martensite materials. Kaynak et al. investigated phase transformation responses of room temperature martensite ($M_s = 33\text{ }^\circ\text{C}$, $M_f = 49\text{ }^\circ\text{C}$, $A_s = 85\text{ }^\circ\text{C}$, $A_f = 107\text{ }^\circ\text{C}$) $\text{Ni}_{49.9}\text{Ti}_{50.1}$ (at.%) in dry, preheated, and cryogenic turning processes ($V_c = 12.5\text{--}100\text{ m/min}$, $f = 0.05\text{ mm/rev}$, $a_p = 0.5\text{ mm}$) [121]. XRD spectra of the machined samples and as-received material is shown in Fig. 15. Prior to machining, no B2 peak was observed, but all machined samples showed B2 peaks. This peak was broader with B19' peaks in cryogenic machining. Austenitic phase transformation is an expected occurrence during machining due to increased cutting temperatures; however, complete transformation to martensite after machining was not observed, and even samples cooled back to ambient temperature (below M_f). The researchers concluded that deformed structure does not allow the subsurface to transform back to austenite after the machining process. Moreover, DSC responses of the machined samples showed that transformation temperatures of the cryogenically machined samples significantly increased. The scholars suggested that stabilized martensite, via residual stress and the plastic strain formation due to higher dislocation density [141], was higher in the samples machined under cryogenic conditions [121]. This stabilized martensite structure is expected to inhibit austenitic transformation by imposing a friction stress on the B19'/B2 interface [142, 143]. Another finding of this study showed that there were considerable differences between first and second cycles of DSC responses of the machined specimens. The largest difference was reported in cryogenically reported specimen.

Active phase of NiTi SMAs has a direct influence on machinability characteristics of these alloys since B2 structure is harder and stronger, while the B19' structure is more ductile and softer. Increased temperatures during machining of NiTi induces austenitic transformation; however, at the same time, concentrated stress in the deformation zone induces martensitic transformation. Kaynak et al. investigated active phase of room-temperature martensitic $\text{Ni}_{49.9}\text{Ti}_{50.1}$ (at.%) in turning process by controlling cutting temperature [122]. They measured the variation in transformation temperatures as a function of stress by load-biased thermal cycling test under 5 and 300 MPa. Workpiece temperature and maximum chip temperature were recorded using infrared camera. Cutting speed-dependent chip temperature values for dry, preheated, MQL, and cryogenic machining are displayed in Fig. 16. It was concluded that the material was in B2 structure during dry, MQL, and preheated machining. Considering increased transformation temperatures ($59\text{ }^\circ\text{C}$ increase) due to deformation stress, cryogenically machined sample was in fully B19' phase except when cutting speed was $V_c = 100\text{ m/min}$.

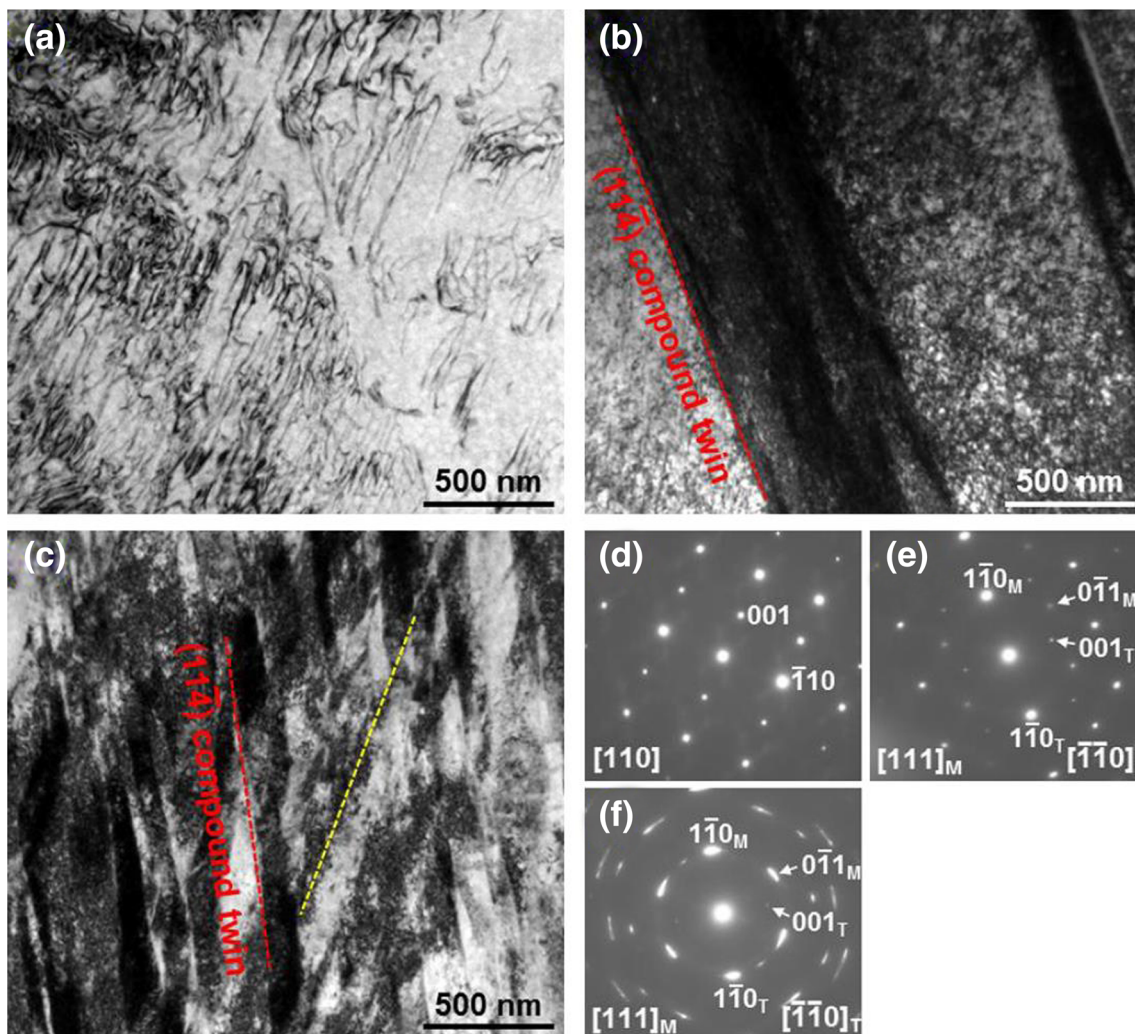


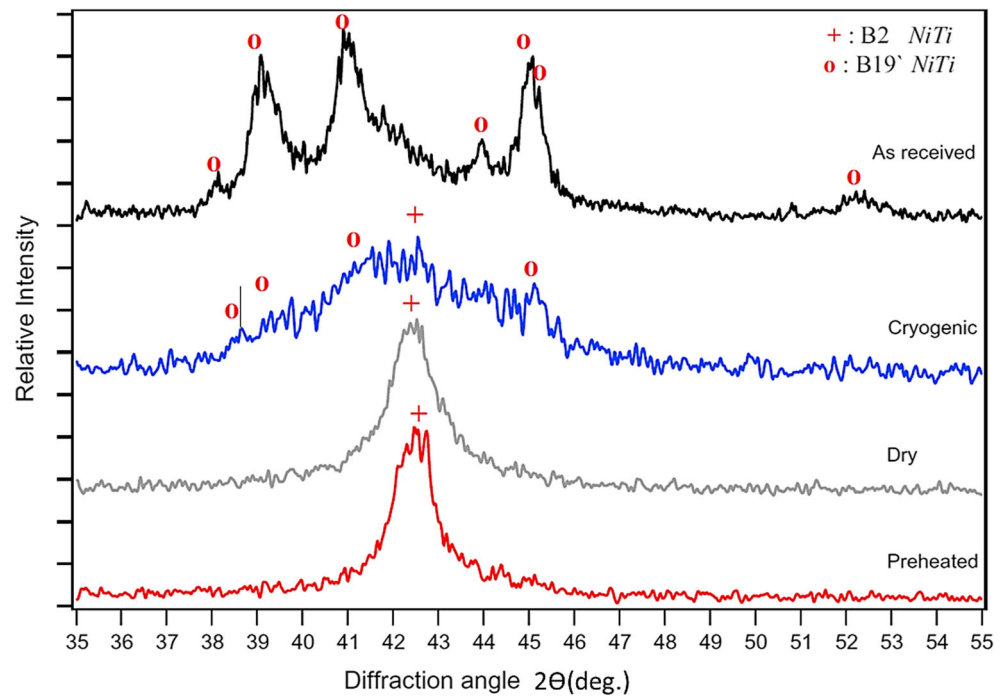
Fig. 14 Bright-field TEM images of specimens: **a** as-received, **b** dry machined, **c** cryogenic machined. Selected area diffraction patterns obtained from specimens: **d** as-received, **e** dry machined, **f** cryogenic machined [120]

4.3 Drilling

Machinability studies of NiTi conducted under drilling process yielded similar results to turning results. Mainly, severe adhesion together with high strain hardening have been reported to be main limitations. A brief review of drilling studies of NiTi is presented in Table 5. Weinert and Petzoldt conducted a study towards understanding the effects of various cutting parameters in drilling and deep hole drilling of martensitic $\text{Ni}_{50.3}\text{Ti}_{49.7}$ (at.%) alloy and austenitic $\text{Ni}_{50.9}\text{Ti}_{49.1}$ (at.%) alloys [42]. The drilling tool was TiCN/TiN multilayer-coated solid carbide drill with a diameter of 5 mm and capable of inner cooling. Effects of cutting speed were investigated between $V_c = 5$ and 160 m/min under the constant feed of $f = 0.1$ mm/rev and drilling depth of $l = 5$ mm. It was observed that there was a nearly constant drilling torque level of 3 Nm independent from alloy and cutting speed. For minimum cutting forces (1200–1500 N), a cutting speed range of about 30–60 m/min was recommended as shown in Fig. 17a.

Investigated feed rates were between $f = 0.05$ and 0.20 mm/rev with a constant speed of $V_c = 60$ m/min. Increase of feed resulted in linearly growing drilling torque and feed force. In terms of martensite and austenite phase comparison, higher feed forces were observed in austenitic alloy resulting from higher tensile stress of austenite compared to martensite. Microhardness test of the subsurface zone showed that the largest subsurface hardening occurs at lowest cutting speeds (up to 100 μm depth), while the increase of cutting speed reduced depth of this area (see Fig. 17b). The scholars attributed this result to large chip thickness and high cutting forces at low cutting speed values. Probably, low temperatures and high mechanical loads at low cutting speeds led to increased twinning and dislocation density as suggested by [50]. Conversely, increased microhardness was observed under increased feed values, which also results in increased chip thickness along with higher cutting forces. Similarly, domination of mechanical effect over temperature effect possibly increased twinning density. The subsurface hardening effect was

Fig. 15 XRD patterns of machined NiTi samples at $V_c = 12.5$ m/min and as-received material [121]



reported to be more severe when drilling martensitic alloy. This result was associated with the lower plateau strength of the twinned martensite compared to that of austenite. Similar results were observed when deep-hole drilling NiTi. Microhardness value as a function of depth from the surface and microstructure of machining affected layer is shown in Fig. 17c. Here, probably, twinned martensite accommodates in the affected layer.

Lin et al. employed tungsten arc melting technique to prepare the $Ni_{50}Ti_{50}$ (B19' phase) and $Ni_{51}Ti_{49}$ (B2 phase) SMA specimens for drilling tests [44]. They used three different drill materials, namely, high speed steel (HSS), HSS + TiN coating, and WC. Regarding the cutting parameters, rotation speed of $n = 88\text{--}305$ rpm and feedrate of $f = 0.07\text{--}0.22$ mm/rev were

tested. Cutting speed of $n = 163$ rpm and feedrate of $f = 0.07$ mm/rev yielded optimum results. Drilling forces up to 5000 N were reported in both alloys. This was attributed to high hardness, viscosity, and pseudoelasticity of the materials. Drilling force results as a function of cutting time for $Ni_{50}Ti_{50}$ and $Ni_{51}Ti_{49}$ are displayed in Fig. 18a and b. TiN-coated HSS tool outperformed the HSS tool in both regards: drilling length (22.9 mm vs. 11.8 mm) and cutting forces. This case, most probably, resulted from increased drill hardness as well as decreased interface friction due to TiN coating. WC drill displayed longest drilling depth among the investigated tools. It was also reported that machining of $Ni_{51}Ti_{49}$ specimen was more difficult (for WC tool 29% less drilling length). This occurrence possibly originated from the higher flow stress of

Fig. 16 Variation of maximum chip temperature as a function of cutting speed [122]

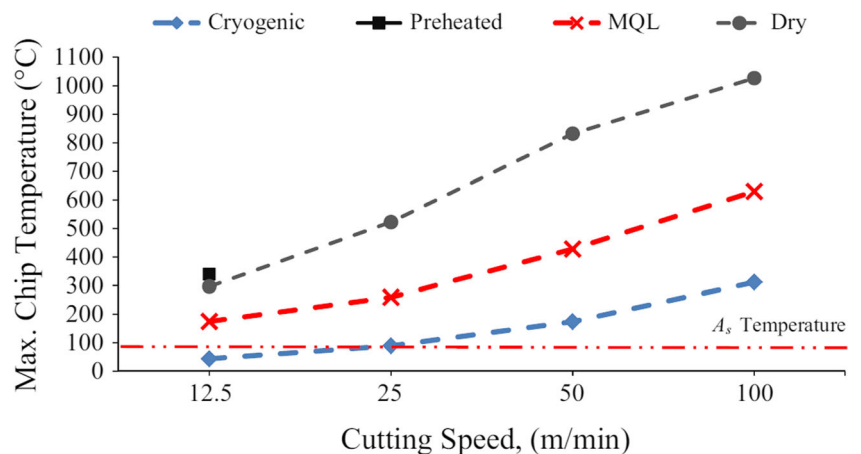
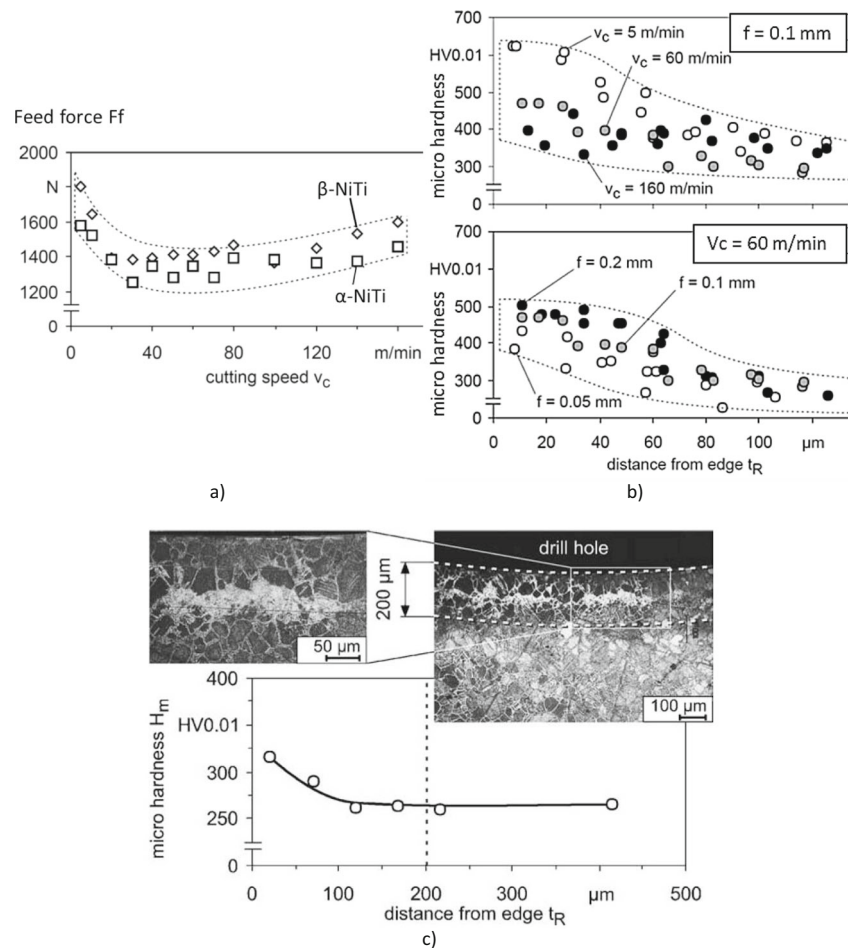


Table 5 A brief review of studies conducted on drilling of NiTi SMA/As

Reference	Material composition	Phase (room temperature)	Cooling condition	Tool material	Tool geometry
[42]	Ni50.3Ti49.7 (at.%)	Martensitic	Internal coolant	Coated carbide	Twist drill (Ø 5 mm)
[44]	Ni50Ti50.7 (at.%)	Martensitic	Internal coolant	HSS HSS + TiN carbide	Twist drill
[82]	Ni50.3Ti49.7 (at.%)	Martensitic	Internal coolant	HSS + coating ISO K10	Twist drill (Ø 5 mm)
[45]	Ni50.3Ti49.7 (at.%)	Martensitic	Internal coolant	HSS + coating ISO K10	Twist drill (Ø 5 mm)
[54] (Micro-drilling)	Ni50.2Ti49.2 (at.%)	Martensitic	High pressure (165 bar)	Carbide	Single-lip drill (Ø 0.5, 1, 1.5 mm)
[42]	Ni50.3Ti49.7 (at.%)	Austenitic	Internal coolant	Coated carbide	Twist drill (Ø 5 mm)
[44]	Ni50Ti50.7 (at.%)	Austenitic	Internal coolant	HSS HSS + TiN carbide	Twist drill
[82]	Ni50.3Ti49.7 (at.%)	Austenitic	Internal coolant	HSS + coating ISO K10	Twist drill (Ø 5 mm)
[45]	Ni50.3Ti49.7 (at.%)	Austenitic	Internal coolant	HSS + coating ISO K10	Twist drill (Ø 5 mm)
[54] (Micro-drilling)	Ni50.2Ti49.2 (at.%)	Austenitic	High pressure (165 bar)	Carbide	Single-lip drill (Ø 0.5, 1, 1.5 mm)

Reference	Cutting parameters		Remarks
	V_c (m/min)	f (mm/rev)	
[42]	5–160	0.05–0.2	Constant drilling torque of 3 Nm achieved under all conditions. Minimum cutting forces (1500 N) can be achieved at $V_c = 30$ –60 m/min. Increase of cutting speed resulted in less subsurface hardening, whereas effect of feedrate on subsurface hardening was converse. Subsurface hardening was more severe in β -NiTi
[44]	88–305 rpm	0.07–0.22	Optimum results were achieved at $V_c = 163$ rpm and $f = 0.07$ mm/rev. In both alloys, drilling forces around 5000 N was achieved. Carbide tool displayed longest tool life. Coated HSS drilled longer than uncoated one. Severe strain hardening was observed beneath the drilled surface
[82]	30–60	0.07	K10 carbide grade drill displayed longer tool life and drilling depth at $V_c = 60$ m/min. However, this tool failed very early at $V_c = 30$ m/min due to excessive chipping. Longest drilling depth was achieved with coated HSS drill
[45]	5–160	0.05–0.2	Minimum specific cutting energy was achieved between $V_c = 80$ –120 m/min. Increased feed rate resulted in decreased specific cutting energy because of decreased friction. Minimal subsurface hardening was obtained when at higher cutting speeds. Martensitic alloy displayed more subsurface hardening compared to austenitic alloy
[54] (Micro-drilling)	30–50	0.0025–0.0075	Severe adhesion was observed on single lip drill. Twist drill resulted in less wear longer drilling length. Higher cutting speed range resulted in lower cutting force and longer tool life. Optimum feedrate was $f = 0.005$ mm/rev. Optimum cutting speed values for single lip and twist drill are 30 and 50 m/min, respectively

Fig. 17 Drilling of NiTi: **a** feed force variation as function of cutting speed; **b** subsurface hardening under various cutting speed values; **c** microstructure and hardening of the subsurface zone when deep hole drilling NiTi [42]



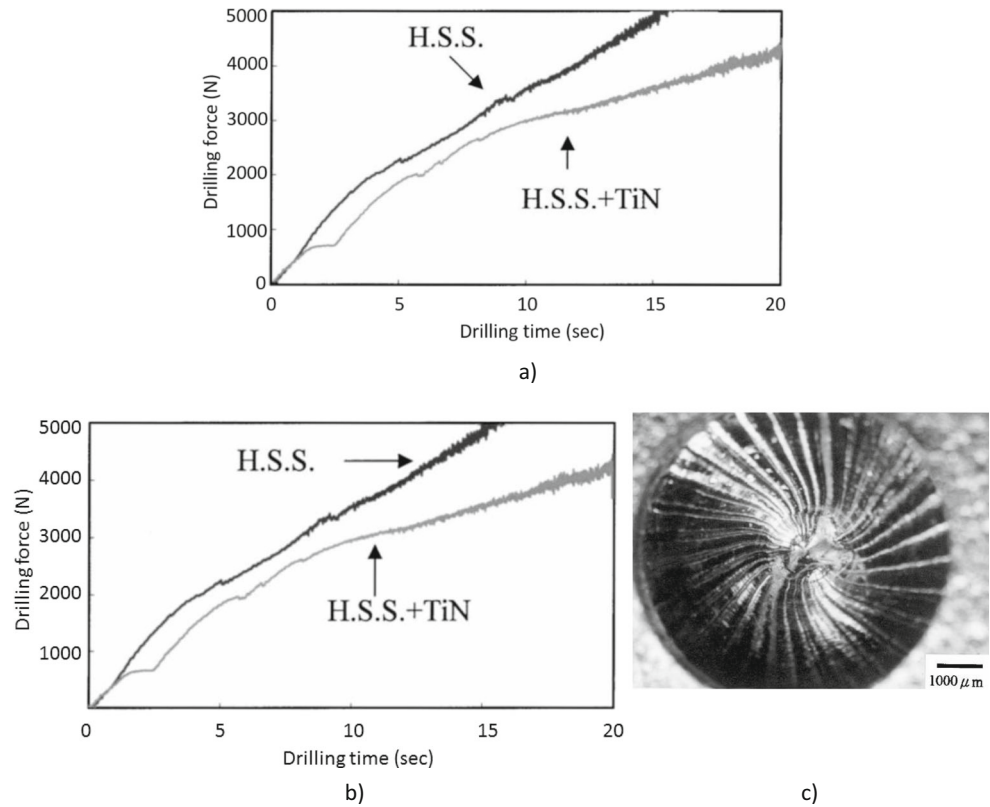
the austenite. Regarding drilling surface morphology, visual wavy tracks on drilled surface were observed (see Fig. 18c). This may promote higher drilling forces and increased vibration along with tool wear. Hardness values of the specimens near to the drilled holes were reported to reach 310 and 370 Hv for the $\text{Ni}_{50}\text{Ti}_{50}$ and $\text{Ni}_{51}\text{Ti}_{49}$, respectively, which may arise from strain hardening due to the large amount of plastic deformation.

Concerning very high loads in the drilling process and poor machinability of NiTi, proper cutting tool material selection is of great importance. Weinert et al. [82] investigated performance of two different drills (5-mm-diameter twist drill) substrates: (1) ISO K10 cemented carbide substrate and (2) ductile core substrate and a hard jacket (ISO M35). The material was $\text{Ni}_{50.3}\text{Ti}_{49.7}$ (martensitic at room temperature) and cutting parameters were cutting speed $V_c = 30, 60$ m/min, feedrate $f = 0.07$ mm/rev, and drilling depth $l = 15$ mm. It was reported that K10 grade drill performed better wear resistance and achieved a longer drilling depth at the cutting speed of $V_c = 60$ m/min. However, this tool failed at the cutting speed of $V_c = 30$ m/min due to excessive chipping after one single boring. This result probably originated from combination of limited toughness of K10 compared to HSS and increased

strain hardening at low cutting speeds. Longest drilling depth was achieved with coated M35 grade at $V_c = 30$ m/min.

Specific cutting energy is a very useful way of quantitatively measuring the efficiency of the metal cutting process or the machinability of a workpiece [144]. Specific cutting energy is affected by many variables such as workpiece material, cutting tool geometry and material, machining parameters (feed, cutting speed, depth of cut), and machining conditions [145–147]. Weinert et al. [45] investigated specific cutting energy of α -NiTi and β -NiTi under variable cutting parameters during drilling operation. They employed solid carbide drills with 5-mm diameter and capable of supplying internal coolant. No significant cutting energy between α -NiTi and β -NiTi was reported. Lower cutting energy was achieved between $V_c = 80$ and 120 m/min. Similarly, best surface quality of $R_z = 1$ μm was acquired at cutting speed of $V_c = 100$ m/min in β -NiTi. Increased feedrate led to increased drilling torque and feed force. However, the specific energy decreased at higher feedrate values because of decreased friction at high feed rates. Alteration of the feed rate did not have a significant effect on surface quality. Concerning subsurface microhardness, higher cutting speeds yielded better results in both regards, hardness value (650 Hv at $V_c = 5$ m/min, 400 Hv at

Fig. 18 Drilling force as a function of drilling time for **a** Ni₅₀Ti₅₀ and **b** Ni₅₁Ti₄₉. **c** Stereomicroscopic image of drilled surface of NiTi SMA [44]



$V_c = 160$ m/min) and harness depth (up to $100 \mu\text{m}$). Effects of feedrate and cutting speed on surface hardening are displayed in Fig. 19a. An increase of feedrate led to increased microhardness due to increased mechanical load. The martensitic alloy displayed more significant strain hardening of the sub-surface zone compared to austenitic alloy.

Biermann et al. investigated micro deep-hole drilling performance of single-lip drills ($\varnothing 0.5, 1, 1.5$ mm) and twist drills ($\varnothing 1$ mm) when machining Ni_{50.2}Ti_{49.8} (at.%) [54]. It was reported that the quality of the drilled holes was good; however, single-lip drill displayed unfavorable adhesion on guide pads. This was attributed to asymmetrical geometry of the

single-lip drill. The scholars suggested two different solution strategies for this: (1) using smaller tip angles to reduce radial forces and (2) guide pad coating to reduce the friction. No adhesion was reported in twist drills, thanks to symmetrical design and TiAlN coating. In terms of cutting length, twist drills outperformed single-lip drills with depths up to 1200 mm versus 420 mm, respectively. In Fig. 20, tool wear under various feedrate values and feed force under various cutting speed values are displayed. Optimum cutting parameters for single-lip drills were reported as cutting speed of $V_c = 30$ m/min and feedrate of $f = 5 \mu\text{m/rev}$. Using a higher cutting speed range resulted in enhanced adhesion, while the

Fig. 19 Drilling of B2 and B19' NiTi: **a** variation of subsurface microhardness for various cutting speed and feedrate values; **b** specific cutting energy as a function of cutting speed [45]

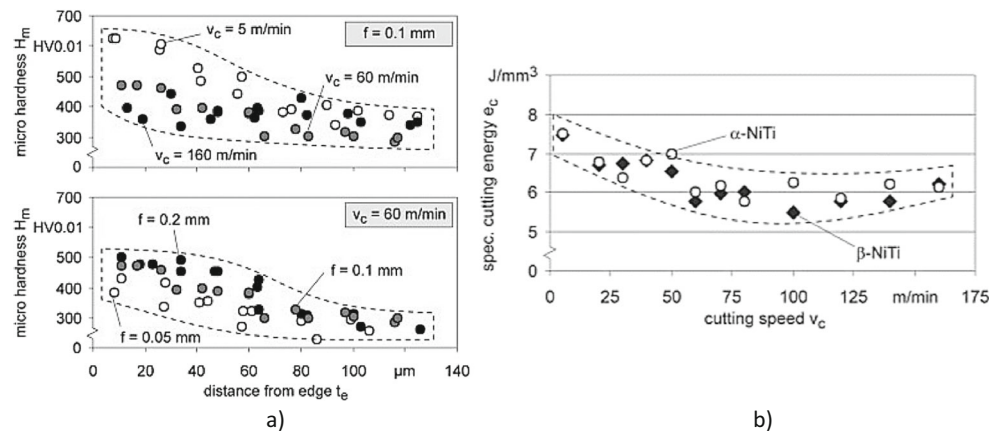
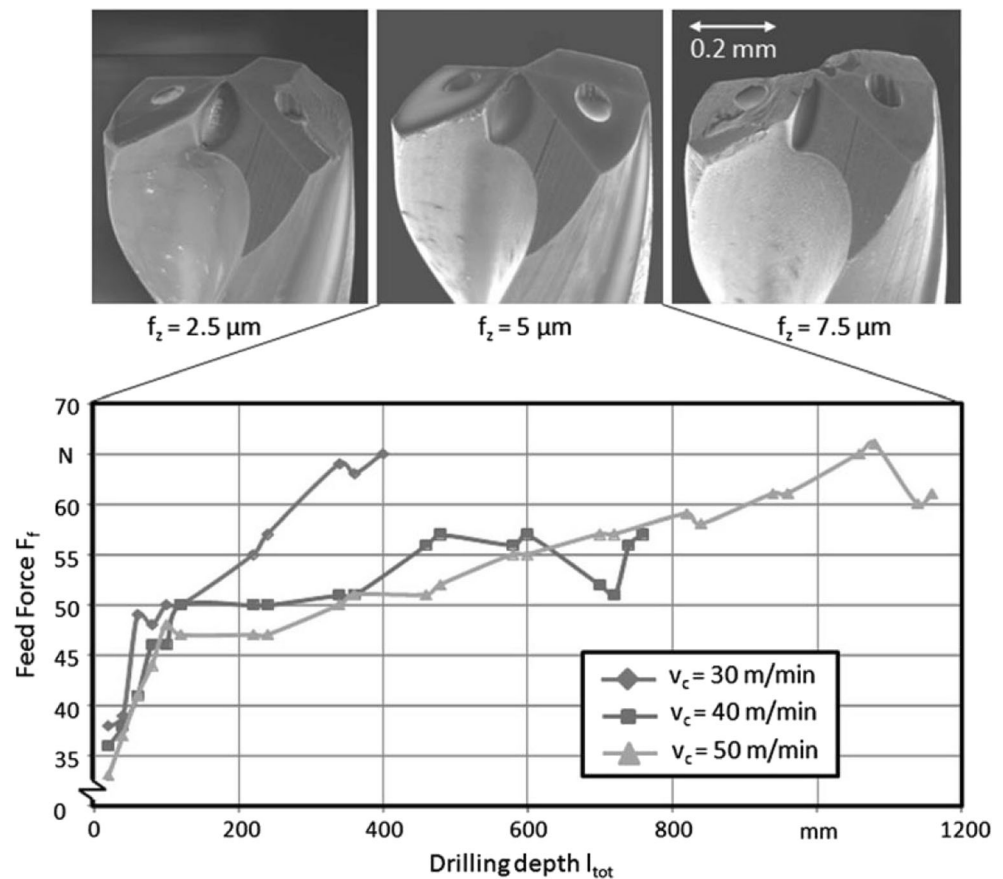


Fig. 20 Feed force and tool life of twist drills (\varnothing 1 mm) as a function of cutting speed [54]



lower range resulted in chipping due to severe strain hardening. When cutting with twist drills, cutting speed of $V_c = 50$ m/min resulted in least cutting force and longest drilling depth (1200 mm), while cutting speed of $V_c = 30$ m/min resulted in largest cutting force and shortest drilling depth (400 mm).

4.4 Milling

Milling operation has a very important place in the machining processes because nearly any shape can be generated by milling process. Although mechanics of milling are very similar to turning, different machinability responses might be observed due to interrupted cutting nature of milling. A brief review of NiTi milling studies and the consequences are briefly summarized in Table 6. Huang investigated effects of cutting speed, feedrate, and depth of cut on cutting force, machined surface characteristics, and tool wear in surface milling of room temperature austenite $\text{Ni}_{50.6}\text{Ti}_{49.4}$ alloy (at.%) [41]. The milling tool was uncoated carbide solid end mill with 10-mm diameter. During the experiments, a wide range of cutting parameters were used (cutting speed $V_c = 5$ to 500 m/min, feedrate $f = 50$ to 1000 mm/min, axial depth of cut $a_p = 0.05$ to 0.5 mm, radial depth of cut $a_e = 2.54$). Some machinability responses of cutting speed variation are displayed in Fig. 21a-d. In the cutting speed range between $V_c = 5$ and 50 m/min,

high cutting forces (25 N) with unfavorable tool wear and high surface roughness ($0.8 \mu\text{m}$, Ra) were observed. In the range between $V_c = 50$ and 200 m/min, minimum cutting forces (2–5 N) with low tool wear rates and best surface roughness ($0.1 \mu\text{m}$, Ra) were reported. Probably, decreased chip thickness and thermal softening caused these positive results. Cutting speed range of $V_c = 200$ to 500 m/min yielded similar results in terms of surface roughness values (0.1 – $0.2 \mu\text{m}$, Ra); however, slightly higher cutting forces (5–7 N) with severe tool wear were observed. This result may have originated from very small chip thickness and consequent tool–chip chemical reactivity. Feedrate variation resulted in expected results. The increase of feedrate resulted in increased cutting forces (range between 2 and 12 N), increased surface roughness (between 0.1 and $0.4 \mu\text{m}$, Ra), and increased wear rate. Depth-of-cut variation yielded similar results to feedrate. Under all milling parameters, microhardness values of machined surfaces (310 – 350 kg/mm^2) were greater than that of as-received part (220 kg/mm^2). Increase of cutting speed resulted in a sharp decrease in microhardness in the cutting speed range between $V_c = 5$ and 50 m/min. This was attributed to less strain hardening in higher speed values due to decreased cutting forces. Feedrate and depth of cut did not have a significant effect on surface hardness. It should be noted that the lowest speed of $V_c = 5$ m/min yielded deepest subsurface

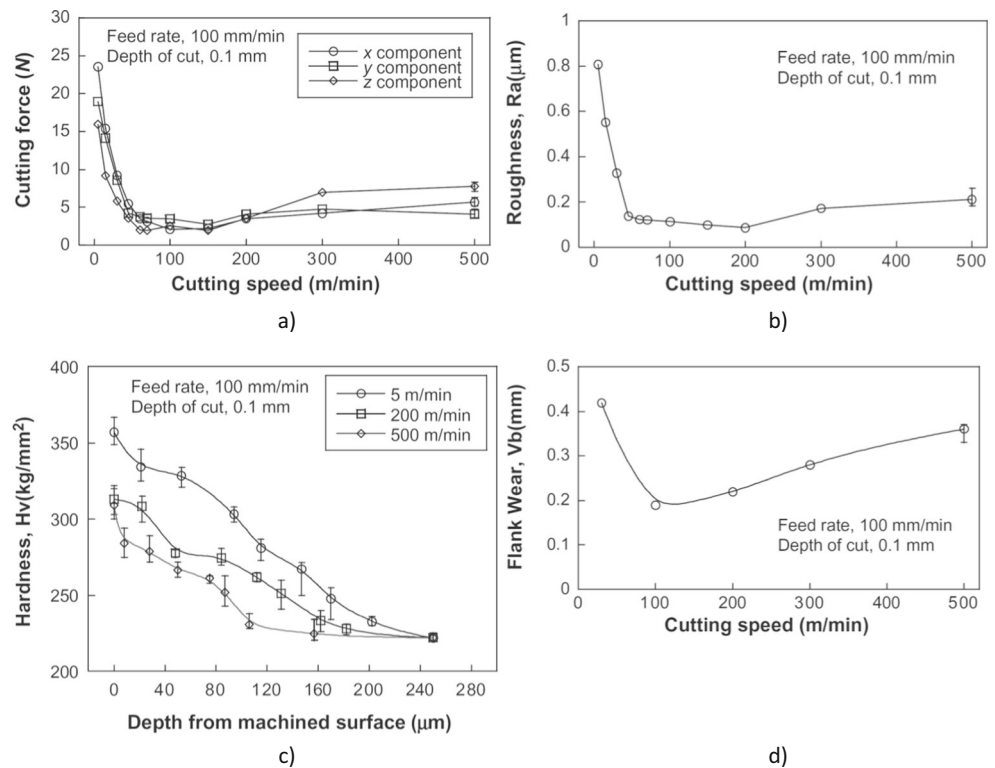
Table 6 A brief review of studies conducted on milling and sawing of NiTi SMAs

Reference	Material composition	Phase (room temperature)	Cooling condition	Tool material	Tool geometry
[41]	Ni50.6Ti49.4 (at.%)	Austenitic	Dry	Uncoated carbide	Solid end mill (\varnothing 10 mm) 4 teeth
[43]	Ni50.8Ti49.2 (at.%)	Martensitic	Flooding	Coated carbide	Indexable mill one tooth $r = 0.8$ mm
[148] ^a	Ni50.4Ti49.6 (at.%)	Austenitic	Flooding	Diamond blade	Circular saw
[44] ^a	Ni51Ti49 (at.%) Ni50Ti50 (at.%)	Austenitic/Martensitic	Flooding	Diamond blade/Emery blade	Circular saw

Reference	Cutting parameters	Remarks
	V_c (m/min)	f (mm/rev)
		ap (mm) \times ae (mm)
[41]	5–500	50–1000
		0.05–0.52.54
[43]	200	50–800
		0.10.25
[148] ^a	1050–1440	0.5
[44] ^a	2500–5000 rpm	

^a Sawing process

Fig. 21 Various machinability responses as a function of cutting speed variation: **a** cutting force, **b** surface roughness, **c** subsurface hardness, **d** flank wear [41]



hardness, while highest speed of 500 m/min resulted in least deep strain hardened layer. XRD spectra of the specimen machined at $V_c = 500$ m/min displayed very similar B2 peaks with as-received material. This means that there is no or minimum machining induced phase change. However, lower cutting speed values might yield B19' peaks because mechanical loads dominate thermal effects at low cutting speeds. This may result in twinning and dislocations under machined surface [119]. Increased subsurface hardening may be related to this occurrence.

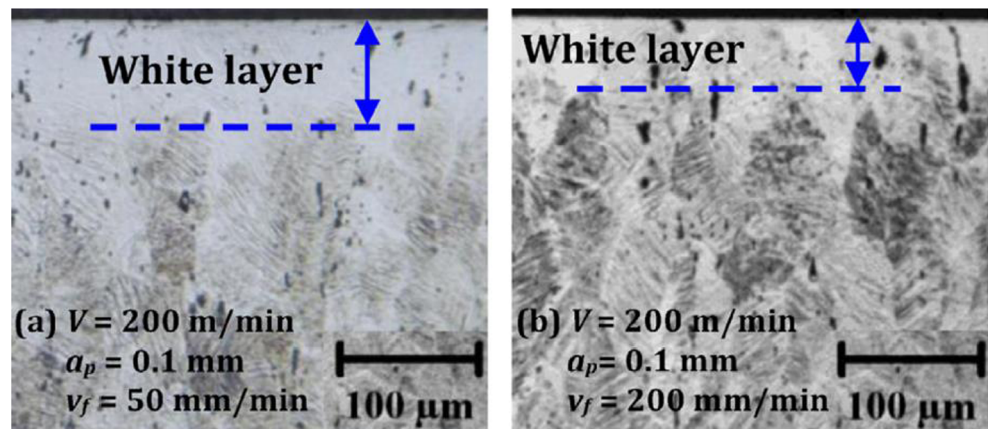
Guo et al. [43] investigated surface integrity characteristics of $\text{Ni}_{50.8}\text{Ti}_{49.2}$ in milling process using AlTiN/TiN-coated carbide milling tools (indexable tool with one active tooth). The investigated cutting parameters were $V_c = 200$ m/min, $f = 50$ – 800 mm/min, $a_p = 0.1$ mm, and $a_e = 0.251$ mm. Reported wear modes were notching, microchipping, flank wear, and coating flaking which is attributed to high cutting temperatures that induced tribo-chemical dissolving. In terms of the surface roughness, the lowest R_a value was yielded at the feed value of $f = 200$ mm/min. This result was attributed to uncertainty and machining dynamics. The largest burr formation was observed at highest feed value and minimum burr being at lowest feed. This may be a result of high ductility of the material rather than phase transformation properties. White layer formation below the milled surface is shown in Fig. 22. Here, the region below the affected layer shows the twinned structure of martensite. The thickness of the subsurface white layer formation was also largest at lowest feedrate.

This was attributed to high mechanical loads under lower feed values, which in turn yields deeper stress-induced phase transformation. This increased hardness was attributed to formation of austenitic structure, following the release of the cutting stress (temperatures above A_1) after the large plastic strain caused detwinned martensitic structure. Similar results were reported by [121]. Notch wear possibly originated from previously explained strain hardening. The findings of this study suggest that thermal softening of the material may take place at elevated feed values. Consequently, high cutting temperatures, possibly, dominated mechanical strains and in turn narrower white layer formation was observed. However, due to the combined complexity of this material and process, further studies need to be conducted in the milling process for a better understanding of this phenomenon.

4.5 Sawing

Sawing process is cutting a workpiece with bandsaws, hacksaws, and circular saws. Circular sawing produces quite accurate dimensions and smooth surfaces because of the rigidity of machines and cutting blade [55]. Therefore, this process gives accurate results when investigating machinability of materials. A brief review of the NiTi sawing studies and the consequences are briefly summarized in Table 6. First investigation on the machinability of the NiTi SMAs was conducted by Wu et al. using circular sawing process [148]. The researchers investigated and compared machinability characteristics of

Fig. 22 Cross-section microstructure of milled specimens [43] (here “ V ” denotes cutting speed, “ V_f ” denotes feed)



three different materials: (1) $\text{Ni}_{49.6}\text{Ti}_{50.4}$ SMA, (2) 18-8 stainless steel, and (3) $\text{Ti}_{50}\text{Al}_{50}$ intermetallic. It was reported that cutting time per unit area for the NiTi increased quickly with increased cutting area as shown in Fig. 23a. Besides, accumulated cut area using same diamond blade was smallest for NiTi among the investigated materials. Therefore, cutting time per unit area was very high for NiTi among the investigated materials. This result was attributed to high ductility of NiTi, which results in adhesion of cut fragments to the blade. Figure 23b displays cut sample microhardness values as a function of depth from the cut surface. Largest strain hardening under the machined surface was observed in cutting of NiTi, whereas hardening depth was similar for all materials. In addition to strain hardening due to cutting action of the cutting blade, this hardening effect was also attributed to fatigue hardening due to cutting process induced vibration [104]. Fatigue hardening is more related to machine dynamics and not discussed in this paper. SEM analysis showed that there were plowing groove and surface pit formation on the cut face. These are indicators of abrasive and adhesive wear impeding machinability rate negatively.

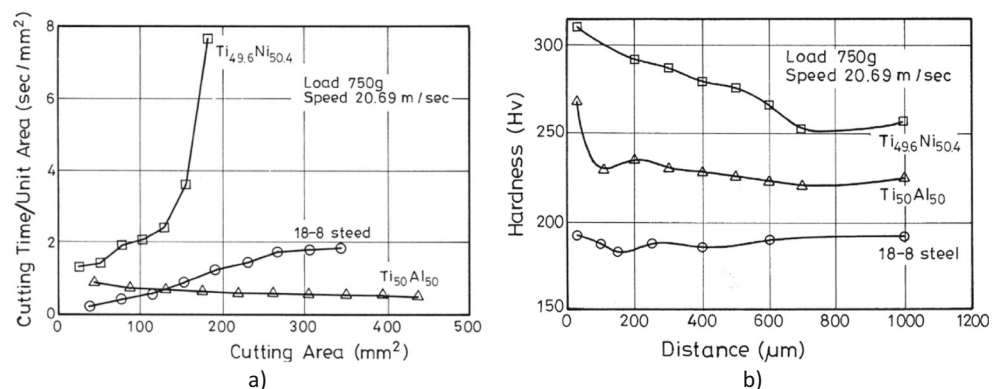
Lin et al. investigated machinability characteristics of $\text{Ni}_{50}\text{Ti}_{50}$ (B19') at room temperature) and $\text{Ni}_{51}\text{Ti}_{49}$ (B2 at room temperature) SMAs during circular sawing [44]. They found that increased cutting load at constant cutting speed resulted in

decreased cutting time only in the early period; however, further increase of the load did not effectively decrease the cutting time. The researchers ascribed this phenomenon to strain hardening and fatigue hardening effects at higher loads [104]. Similar behavior was observed when rotation speed was increased under constant cutting load. Increased cutting speed resulted in only a slight decrease in cutting time. This was attributed to the fatigue hardening effect of higher blade rotational speed. Regarding the blade material, emery blade displayed better cutting rate compared to diamond blade. The authors attributed this to adhesion of some cut fragments of NiTi on diamond blade because of high ductility of the material. Emery blade, on the other hand, was composed of SiC and Al_2O_3 particles, which dresses itself like abrasive cutting tools. It was reported that cutting time for both compositions were similar, although they exhibit different mechanical characteristics and active phase structures at room temperature. This result indicates that both materials were, probably, machined under the same phase structure. These were most probably temperature induced austenite.

4.6 Micro-milling

Micro-machined NiTi SMA parts are generally used for medical applications and micro-mechanical applications [11, 21,

Fig. 23 Circular sawing of three different materials including NiTi: **a** cutting time per unit area, **b** post cutting subsurface microhardness [27]



149, 150]. These components can be manufactured by laser cutting since this method renders possible producing topologies smaller than 100 μm in size and cutting NiTi thin film material [151, 152]. Micro-milling is an alternative production process for these components since it offers high material removal rates, high surface quality, and very little thermal damage. Although cutting mechanics do not differ, all machinability responses and machining parameters of the macro-scale milling process cannot be generalized down to micro-milling process. Thus, it is not possible to determine machining parameters by a linear scale-down approach because in micro-milling, the material spring back for ductile materials and a plowing effect, when undeformed chip thickness is comparable to cutting edge radius or lower, are observed [110]. These factors are known as size effect [153]. A brief review of micro-milling studies of NiTi is presented in Table 7.

As mentioned in previous sections, cutting parameters as well as cooling–lubrication conditions are of great influence in micro-machining of NiTi SMAs. Weinert and Petzoldt investigated optimum cutting parameters when micro-machining β -NiTi SMA (50.8, at.% nickel) in dry and MQL ($Q < 1$ ml/min, ester oil) condition [151]. The milling operation was conducted using 0.4-mm-diameter TiAlN-coated carbide mills using two different strategies: (1) slot milling (full radial immersion) and (2) end milling (partial immersion). Adhesion of NiTi on micro end milling cutter and burr formation were reported to be the main problems. Axial cutting depth of $a_p = 10$ μm led to best surface quality among the all investigated conditions. Increasing the radial cutting depth from $a_e = 10$ to 40 μm resulted in better surface quality as well as decreased cutting forces. Similar behavior was observed when feed rate was increased. Increasing feed per tooth value from $f_z = 8.4$ to 30 μm resulted in decreased cutting forces, especially in passive force component. Positive results of increased radial cutting depth and feed may have resulted from increased chip thickness, which diminishes the possibility of chemical reaction between cut chip and cutting tool. In dry cutting condition, no adhesion and a little burr formation were observed at the end of the first slot ($L = 10$ mm). However, when milling continues with the same tool, formation of adhesion and burr at the edge of slot geometry were reported at the end of the second slot ($L = 20$). In Fig. 24, tool wear and burr formation after first and second slot under dry cutting are displayed. In MQL condition ($a_p = 10$ μm , $a_e = 40$ μm), after milling with the same tool six consecutive slots, very little adhesion was reported and the workpiece quality remained on high level with the minimum burr formation.

Applying chilled air on cutting region is another strategy to increase machinability in nickel and titanium alloys [154–156]. Zailani and Mativenga investigated effects of chilled air application on the machinability of room temperature martensitic Ni₅₅Ti₄₅ (wt.%) in micro-milling process

under three cutting conditions: (1) chilled air ($T = -8.5$ to -10.5 °C, $u = 14$ m/s), (2) MQL, and (3) chilled air and MQL [110]. The researchers hypothesized that keeping the material at low temperatures (martensitic at room temperature) may prevent entering the austenitic phase during machining. The cutting tool was an AlTiN-coated carbide solid end mill with 0.5 mm diameter. The cutting parameters were as follows: $V_c = 35$ m/min, $f = 184$ mm/min, $a_p = 30$ μm , and $a_e = 0.2$ mm (MRR = 1.1 mm³/min). After machining in the chilled air condition, microstructure was more homogenous than machining with other conditions. However, it should be noted that the investigated specimens for microstructure analysis were layers parallel to milling surface, not cross-sectioned specimens. Under the chilled air condition, machining induced layer might have been observed in cross-sectioned specimens because the maximum hardness value of machined surface was observed when chilled air was applied. This indicates hardened martensite. MQL alone yielded least homogenous and dendritic structure. Minimum cutting forces were yielded when chilled air was applied. This may be an evidence to support the hypothesis that keeping the material in martensitic phase while machining results in lower flow stress because of softer structure of martensite. In terms of the surface quality, presence of chilled air and MQL together yielded the best results (Ra, 0.26 μm). Regarding burr formation, simultaneous application of chilled air and MQL resulted in smaller and uniform burrs. Under all conditions, the dominant wear mode was flank wear and chipping. Minimum tool wear was observed under MQL concurrently applied with chilled air condition (flank wear < 200 μm), while maximum wear was reported under chilled air condition (flank wear ≈ 1700 μm). This was attributed to high friction in absence of lubrication. Besides, strain hardening of martensitic structure may also be responsible for chipping. This study shows that keeping the temperature low around the cutting region is an efficient method for keeping the material in martensitic structure. However, the chilled air alone condition is not suitable due to increased friction at the tool–chip interface. As a result, the addition of MQL to chilled air application yielded optimum conditions.

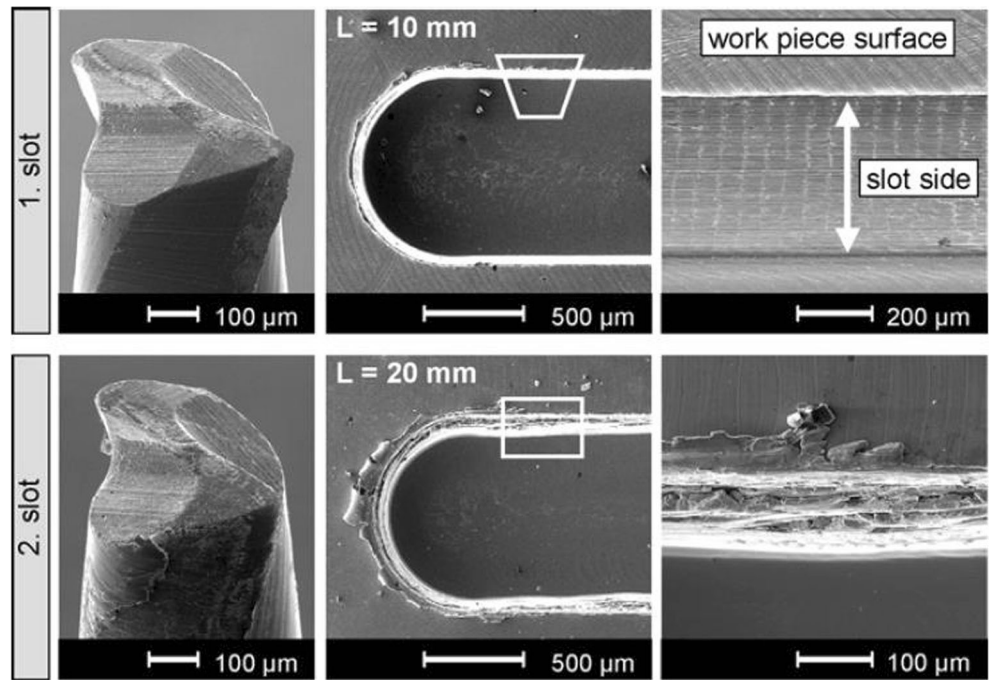
Kuppuswamy and Yui aimed to optimize cutting parameters of Ni_{50.6}Ti_{49.4} alloy (at.%) in micro-milling process (MQL at $P = 4$ bar, $Q = 80$ ml/h) using two-teeth solid carbide end mills of 0.3-mm diameter [99]. The material was in the austenite phase at room temperature and an R-phase transition was reported in DSC graph, which means Ti₃Ni₄ precipitates existed in specimens. A very broad range of machining parameters were tested in the study ($V_c = 4.7$ –30.1 m/min; $f_z = 0.005, 0.008, 0.012$ mm/tooth; $a_p = 0.008, 0.01, 0.012$ mm). The experiments resulted in a decrease in cutting forces and increase in hardness when cutting speed increased from 4.7 to 15 m/min as shown in Fig. 25. However, a further increase in cutting speed resulted in increased cutting force and decreased hardness value. The trend of the cutting forces, which is

Table 7 A brief review of studies conducted on micro-milling NiTi SMA

Reference	Material composition	Phase (room temperature)	Cooling condition	Tool material	Tool geometry
[110]	Ni55Ti45 (wt.%)	Martensitic	Chilled air/MQL	Coated carbide	Solid end mill Ø0.5 mm
[99]	Ni50.6Ti49.4 (at.%)	Austenitic	MQL	Carbide	Solid end mill Ø0.3 mm
[46]	NiTi	Martensitic/Austenitic	MQL	Coated carbide	Solid end mill Ø0.8 mm
[151]	Ni50.8Ti49.2 (at.%)	Austenitic	Dry MQL	Carbide (AlTiN coated)	Solid end mill Ø0.4 mm
[49]	Ni49.7Ti50.3 (at.%) Ni49.9Ti50.1 (at.%)	Martensitic/Austenitic	MQL	Coated carbide	Ball nose mill Ø1 mm

Reference	Cutting parameters	Remarks
	V_c (m/min) f_z ($\mu\text{m}/\text{tooth}$) a_p (μm) a_e (μm)	
[110]	35 $f = 184$ (mm/min) 30	Machining with chilled air yielded the most homogenous structure and minimum cutting forces. However, higher flank wear and chipping was observed under chilled air condition. Moreover, greatest surface hardness resulted from chilled air application. These results suggest that applying chilled air was successful at keeping the material in B19' structure
[99]	4.7–30.1 5–12 8–12	Minimum cutting forces and maximum surface hardness was obtained at $V_c = 15$ m/min. Increase of decrease of cutting speed from $V_c = 15$ m/min resulted in remarkable increase in cutting force and decrease in cutting force. This was attributed to stress induced martensite at $V_c = 15$ m/min. Maximum tool life was achieved at this cutting speed
[46]	30, 60 6, 12 50, 100 50, 100	Minimum burr formation was observed under $V_c = 30$ m/min, $f_z = 12$ $\mu\text{m}/\text{tooth}$, $a_e = 100$ μm and up-milling strategy. After machining, permanent martensitic and austenitic layer was observed under machined surface for austenitic and martensitic materials, respectively
[151]	33 8.4–30 10 10, 40	Problems: adhesion and burr formation Results: best surface quality and minimal tool life was achieved at $a_p = 10$ μm and $a_e = 40$ μm . Increasing feedrate from $f_z = 8.4$ to 30 $\mu\text{m}/\text{rev}$ resulted in less cutting forces. MQL yielded better tool life compared to dry cutting
[49]	37, 47 6 50–150, 250	Less adhesion, more favorable chip formation, and better surface quality was achieved at $a_p = 10$ μm and $a_e = 250$ μm . Inclination angle of 50° yielded best surface quality and minimum tool wear. Compared to martensitic alloy, less tool wear and better surface topography were yielded in austenitic alloy

Fig. 24 Tool wear and burr formation after machining first and second slots at $V_c = 33$ m/min, $f_z = 0.02$ mm/rev, $a_p = 0.010$ mm, $a_e = 0.04$ mm [151]

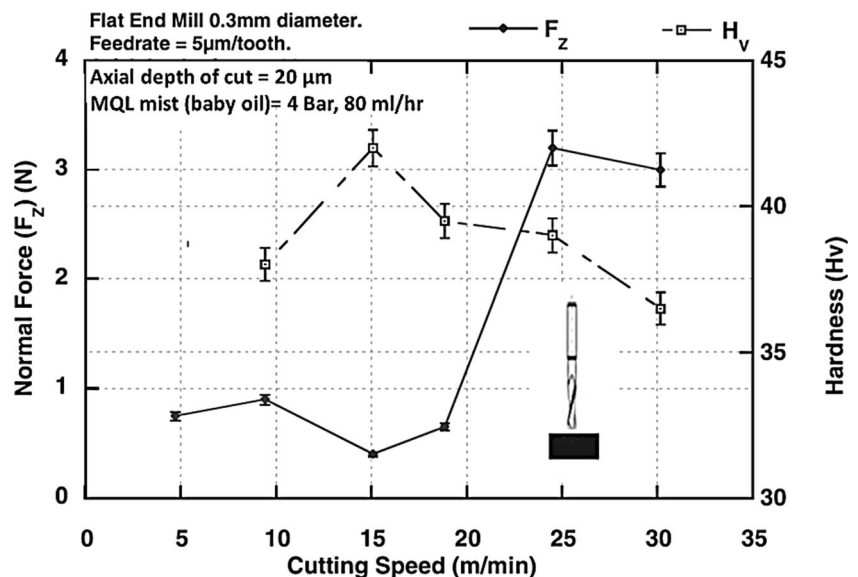


primarily affected from cutting speed, displayed the similar trend under all feed and depth-of-cut values. The reduction of hardness in either side of 15 m/min cutting speed was attributed to stress-induced martensitic phase transformation from B2 to B19' because it was shown that stress-induced martensite exhibits a higher hardness value than martensite [120, 157] and martensite is more prone to strain hardening [44, 45]. Burr formation and slot appearance were also reported to be indicators of austenite to martensite phase transformation between cutting speeds of 15 to 20 m/min, as only two of milled slots (under $V_c = 15$ and 24.5 m/min) were completely milled through. Higher mechanical strength of

the austenite possibly resisted feed motion of the cutting tool. This reduced micro slot quality. As expected, the tool wear behaviors were similar to cutting forces. At cutting speed of $V_c = 15$ m/min maximum tool life was achieved (80 m). At cutting speed of $V_c = 30$ m/min minimum tool life (<5 m) was observed with extensive built up edge (BUE) formation.

As mentioned previously, burr formation is one of the major problems in machining of NiTi due to ductility and unconventional stress–strain behavior of this alloy [42]. This problem gains more importance considering the significance of biomedical applications of NiTi. Piquard et al. investigated burr formation and machining-induced phase transformation

Fig. 25 Cutting force and hardness response of NiTi against cutting speed when micromilling NiTi [99]



in micro end-milling (0.5 mm tool diameter) of martensitic and austenitic NiTi alloys under MQL condition [46]. They employed design of experiments (DOE) approach to investigate the effects of process input parameters, namely, strategy (up-down milling), depth of cut ($a_p = 50, 100 \mu\text{m}$), cutting speed ($V_c = 30, 60 \text{ m/min}$), alloy phase at room temperature (martensitic, austenitic), feed ($f_z = 6, 12 \mu\text{m/tooth}$), and width of cut ($a_e = 100, 200 \mu\text{m}$) on the following machining responses: burr height, burr thickness, and burr width. It was reported that increase of feed led to decrease of burr height and burr width while the increase of cutting width led to increased burr height and burr width. Increase of depth of cut also resulted in decreased burr height. In terms of machining strategy, wider top burrs were reported in up milling. Regarding burr thickness, increase of cutting speed led to thicker burrs, whereas the increased depth of cut, feed, and width of cut decreased burr thickness. Effects of machining on microstructure were analyzed by micrographs of cross-sections from machined surface. Subsurface microstructure and permanent phase transformation results were similar to previously discussed studies [43, 99, 120]. It was reported that there was a white layer zone of approximately $20 \mu\text{m}$ under machined surface for martensitic material as shown in Fig. 26a. This zone was affected by austenitic phase transformation because of increased temperature during machining. However, this zone did not revert to martensite after cooling. For austenitic alloy, on the other hand, a narrower subsurface phase transformed zone ($10 \mu\text{m}$) was observed. This zone is characterized by permanent martensitic phase transformation, which happens due to extensive twinning.

Biermann et al. investigated effects of variation of cutting tool inclination angle and cutting parameters when multi-axis milling room temperature martensitic $\text{Ni}_{49.7}\text{Ti}_{50.3}$ (at.%) and austenitic $\text{Ni}_{49.9}\text{Ti}_{50.1}$ (at.%) alloys [49]. They used two-lip, TiAlN-coated ball nose cutters with 1-mm diameter under MQL condition. Less adhesion was reported when width of cut increased to $a_e = 0.25 \text{ mm}$. However, depth-of-cut values larger than $a_p = 0.1 \text{ mm}$ led to increased tool wear and surface deterioration. Best surface quality and minimum tool wear

were achieved at an inclination angle of 50° . Ball nose cutters have different peripheral cutting speed depending on their contact radius and inclination angle. Increased adhesive tool wear and decreased surface quality were reported where maximum cutting speed exceeded $V_c = 50 \text{ m/min}$. Machining of austenitic alloy resulted in quite acceptable surface quality and tool wear as shown in Fig. 27. Conversely, unfavorable surface quality and tool wear were observed in martensitic alloy. Label A shows the burr formation on the tips of milling path. As seen in Fig. 27, this kind of burr formation was more evident in martensitic alloy. The scholars attributed this to high break elongation of martensite. Higher rate of strain hardening of martensite may be another factor.

5 Numerical modeling

There is not a generally accepted theory explaining the exact chip formation mechanism due to the complexity of the machining process (variables such as strain hardening, very high strain rate, very high cutting temperatures, and heat transfer). In many of the proposed analytical models, prediction of the cutting forces is aimed and these variables are not included. Due to its capabilities to perform coupled analysis with these variables, finite element method (FEM) has been widely accepted in simulation studies, thanks to the development of new numerical models and faster computers. Considering the fact that experimental studies for every machining condition is time and money consuming (i.e., costly alloys and cutting tools) and not environment friendly (e.g., waste machining products, consumed energy), the popularity of FEM studies in machining simulation is now increasing. Today, finite element (FE) models in machining process are used for gaining knowledge on fundamental sight of metal cutting mechanisms; as they have a proven ability to predict important cutting parameters such as cutting forces, temperatures, stresses, and strains, which are essential for prediction of other machining outputs [158].

Fig. 26 Machining induced subsurface layer: **a** martensitic material, **b** austenitic material [46]

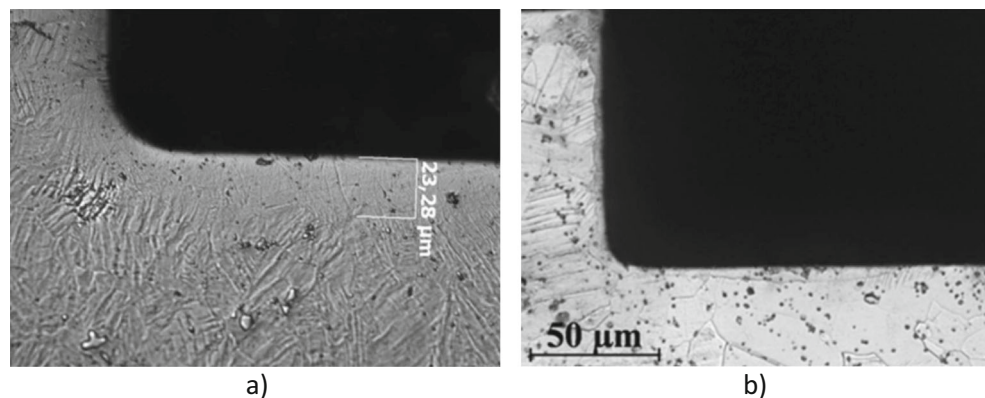
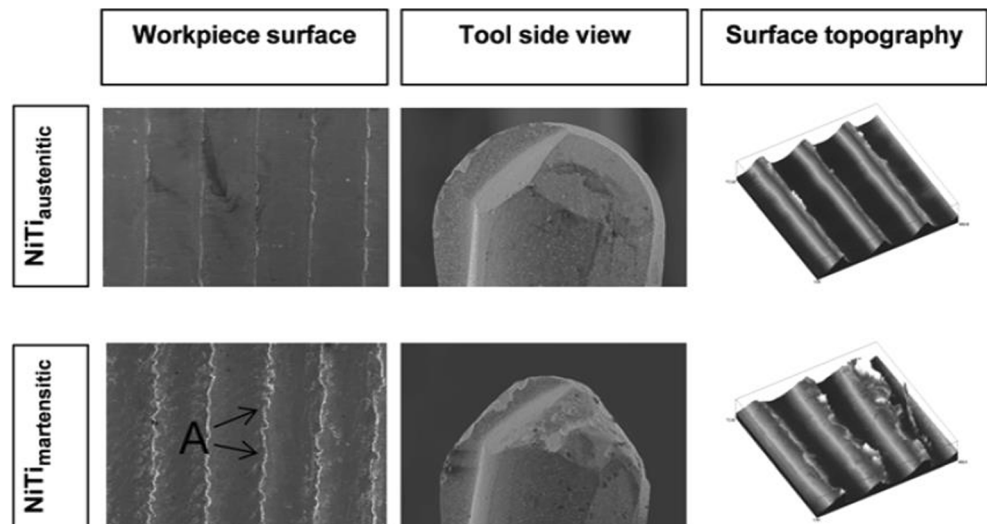


Fig. 27 Surface topography and tool wear of austenitic and martensitic NiTi after multi-axis micromilled [49]



The number of the FE-based NiTi machining models is very limited [67, 159]. However, there are studies, which develop the state of knowledge to predict behavior of these materials, conducted on modeling of mechanical, dynamic, and thermomechanical behaviors of NiTi. Qiang et al. proposed a back propagation neural network model to predict mechanical properties (compressive yield stress and Young's modulus) of porous NiTi SMA prepared by thermal explosion [160]. According to their validation comparison, the prediction error lies within 0.018. Nemat-Nasser et al. introduced a micromechanical model to predict the stress-induced phase transformations of porous shape-memory alloys with small porosity [161]. Similarly, Ashrafi et al. proposed a phenomenological constitutive material model for dense and porous SMAs including phase transformation behavior. They have also validated their numerical model by comparing FE software results to experimental results [162]. Williams et al. proposed a dynamic model to predict transient behavior of SMAs as an adaptive tuned vibration absorber [163]. Paradis et al. proposed thermomechanical coupled model with aim to predict the accumulated strain on NiTi [164]. They have reported a good agreement between experimental and simulated data; however, the validation was conducted only under uniaxial cyclic loading. Lagoudas et al. introduced a phenomenological constitutive model for NiTi that predicts stress-induced and thermally induced phase transformations [165]. The ability of the developed model to capture material behavior under different three-dimensional thermomechanical loadings was demonstrated. Petrini et al. developed a numerical model to predict macroscopic thermomechanical behaviors of NiTi mainly focusing on an efficient algorithm for practical applications [166]. They validated pseudoelasticity and shape memory prediction of the model by comparing experimental and numerical results on medical devices.

Many successful simulation studies were conducted mainly focusing on machinability concerns of Ni- and Ti-based high-

temperature alloys. These studies may guide the future numerical studies on machining of NiTi. It was reported that it is possible to achieve a good prediction of both the principal cutting forces and the chip morphology if the material constants for the constitutive material model are well identified using experimental data [167]. Özkaya and Biermann presented a new method to investigate chipping zone during drilling of Inconel 718 by combining FEM and computational fluid dynamics (CFD) simulations [168]. They reported that coolant does not reach the major cutting edges, although drills with internal coolant channels were used. Within the same context, CFD simulations and experimental results have shown that increasing the cooling pressure resulted in higher flow rates near the cutting edge [169]. Alternatively, modified twist drill [170] was developed using simulative optimizations [171]. Chen et al. developed a ductile fracture energy-based Johnson–Cook material model in FE analysis of high-speed machining of Ti6Al4V alloy [172]. They reported that predicted chip morphologies and cutting forces during high speed and relatively low cutting speeds showed a good agreement with experimental results. Thepsonthi and Özel carried out a FEM-based study toward understanding the effects of CBN coating on carbide micro-end mills in terms of surface roughness, burr formation, and tool wear performance, using the model proposed by Usui [173], in micro-machining of Ti6Al4V alloy [174]. Ranganath et al. presented a FE-based machining model of a nickel superalloy IN100 to predict critical parameters for the formation of machining-induced subsurface damages such as white layer and bent grains in finish machining [175]. Özel et al. compared 3D machining models of Inconel 718 developed using various commercially available FE software. In the study, experimental results were compared with computational results of temperature, strain, and stress distributions obtained from the FE models [176]. Mitrofanov et al. conducted a study toward FE modeling of thermomechanically coupled conventional turning and

ultrasonically assisted turning of Inconel 718 [177]. Özel et al. suggested a 3D FE model to predict machining-induced residual stresses for Ti6Al4V and IN100 alloys [178]. Jafarian et al. presented a study toward modeling a FE simulation for the prediction of the microstructure changes during the orthogonal machining of Inconel 718 alloy [179]. Uhlmann et al. conducted a study to implement 2D and 3D FE models of chip formation during machining of Inconel 718 focusing on qualitative and quantitative parameters of cut chip [180].

Mostly, cutting force, stress, and strain values in the primary deformation zone have a direct influence on tool wear and post machining mechanical properties of the workpiece [181]. Mehrpouya et al. investigated the optimum cutting speed of NiTi regarding cutting force, von Mises, and shear stress criteria aspects [67]. The experimental part of the study included machining of NiTi under various cutting speed values ($V_c = 20, 80, 100, 110, 130$ m/min) and constant feed ($f = 0.05$ mm/rev) and depth of cut ($a_p = 0.2$ mm). The results of the experimental part showed that there was a nearly linear decrease in cutting force when cutting speed was increased gradually from $V_c = 20$ to 110 m/min in both dry and flooded (emulsion) cutting concepts. Further increase of the cutting speed to 130 m/min resulted in increased cutting force. At the optimum cutting speed of $V_c = 110$ m/min, cutting forces of around 50 N was yielded. In 3D numerical part of the study, influences of cutting speed on von Mises stress and shear stress were studied. According to von Mises stress results, optimum cutting speed was $V_c = 110$ m/min, which resulted in lowermost von Mises stress of 3.38×10^9 N/m². Regarding shear stress values, optimum cutting speed was 80 m/min, which resulted in minimum shear stress of 1.26×10^9 N/m². Concerning the optimum cutting speed of NiTi, the experimental and simulative results of this study were in an agreement with previously reported experimental studies [41, 42, 82].

Shape memory and microstructural properties of NiTi SMAs have been greatly influenced from cutting conditions and cutting parameters, as presented by various studies [41, 45, 50, 82]. These studies showed that machining-induced martensitic phase transformation of NiTi affects microstructure and surface integrity characteristics [41, 44, 159]. A better understanding of this phase transformation is needed in order to control surface integrity and functional behavior of NiTi. In this regard, FE modeling approach may be an alternative or a supporter technique to experimental studies. A very limited number of studies focusing on phase transformation response during machining simulations were found in the literature. Ramesh and Meltoke investigated effects of stress and temperature on phase transformation of AISI 52100 steel in machining process [182]. Schulze et al. presented a study to simulate machining-induced phase transformation in cutting process [183]. Auricchio and Taylor made an attempt to simulate superelastic behavior of SMAs [184]. Their study suggested a

constitutive material model which can simulate three phase transformations: (1) conversion of austenite into single-variant martensite, (2) conversion of single-variant martensite into austenite, and (3) reorientation of single variant martensite. The first two of these phase transformations included martensite fraction. Accordingly, FE model simulations of a four-point bending test on a circular wire and radial displacement test on a medical stent were implemented. The experimental results of the bending test were in a good agreement with the FE simulations.

Lastly, Kaynak et al. presented a 2D numerical study toward understanding martensitic phase transformation of austenitic NiTi alloy (A_f at 6 °C) during turning experiments [159]. The cutting tool was TPGN 220412 (K313 grade, $r_e = 22\text{--}26$ μm) and the cutting parameters were uncut chip thickness of 0.05 mm and cutting speeds of $V_c = 6.25, 12.5$ m/min. Flow stress curves of the FE model were taken from study of Adharapurapu [111] to simulate plastic flow of the austenitic material. A rate-dependent transformation law, which expresses the rate of change of the volume fraction of martensite suggested by Anand and Gurtin [185], was employed to simulate the martensitic phase transformation [184]. FE simulation results showed that the higher volume fraction was present at the machined surface and around side of the chip in contact with the rake face of the cutting tool. This result was parallel with effective stress distribution (stress-induced martensite) results. Another important finding was that as the cutting speed increased, the martensitic volume fraction decreased. This was, most probably, a result of the decreased flow stress of the material at higher cutting speeds due to thermal softening. Optical microscope examination results of experimentally machined specimens showed that more twins took place beneath the machined surface. It was reported that depth of the affected layer at lower cutting speed ($h = 180 \pm 20$ μm at $V_c = 6.25$ m/min) was larger than that at higher cutting speed ($h = 140 \pm 20$ μm at $V_c = 12.5$ m/min). The results of the suggested FE model and experimental results were, qualitatively, in a good agreement through developing a better understanding of machining-induced martensitic transformation.

6 Discussion

Machining of NiTi SMAs is very difficult, mainly due to high cutting temperatures concentrated around the tool edge and unique stress–strain behavior of the material. High temperatures are caused by high ductility, low thermal conductivity, and high specific heat of the material. High work hardening capacity of the material further impedes the machinability. As a result of all these factors, severe tool wear and excessive burr formation stands for a major limitation. The solid-state phase transformation of this alloy, which happens in the range of

machining temperatures, is another substantial limitation. The studies showed that machinability responses and microstructure of the material may be significantly altered depending on active phase. Accordingly, optimum machining parameters reside in a very narrow range and cutting conditions have a significant effect on the machinability rate of these materials. In this section of the paper, discussion of the machining responses of NiTi is aimed. Due to size effect, direct quantitative cutting parameters of micro machining operations are not included to discussion. However, qualitative responses are included, as cutting mechanics are very similar.

Cutting forces are of paramount importance as they directly affect power consumption and have a very strong effect on tool wear and surface integrity. The review of the present studies showed that there is an agreement on optimum cutting parameters to achieve minimal cutting forces. The majority of the scholars reported that optimum cutting speed is around $V_c = 100$ m/min for coated carbide tools in turning process [42, 67, 82]. However, it was also reported that cutting forces were not significantly affected from the variation of cutting speed between $V_c = 25$ and 100 m/min [122]. This result may be originated from process design or tool coating. There is an agreement on feedrate, increase of which beyond $f = 0.05$ mm/rev increases cutting forces. Similarly, when drilling NiTi, cutting speed of $V_c = 100$ m/min and feedrate of $f = 0.05$ mm/rev yielded minimum cutting forces. When milling NiTi, optimum cutting speed and feed was $V_c = 200$ m/min and $f = 100$ mm/min to achieve minimum cutting forces. During machining, applying chilled air [110] or cryogenic cooling [105] were reported to decrease cutting force because these applications keep the material in the martensitic structure which is softer and more malleable. It should also be mentioned that the increase of the radial width of the cut a_e over 50% of the cutting tool under constant MRR resulted in decreased cutting forces [49, 151].

Tool wear is very severe when machining NiTi and is a major cause of the poor machinability rate of this material. Mostly observed wear types are flank wear, notch wear, chip flow damage, crater wear, edge breakage, chipping, and BUE, while most dominant wear mechanisms are adhesion and abrasion. Similar to other difficult-to-machine materials, wear rate and cutting force curves as a function of cutting parameters are very similar when machining NiTi. The most suitable cutting parameters for minimum tool wear lies within a very narrow range. Active phase of the material during machining was reported to have a remarkable effect on tool wear. Keeping the workpiece in B19' structure was reported to increase tool life, mainly because of lower yield strength of martensite compared to austenite [99, 110]. Accordingly, cooling conditions, where liquid N_2 or chilled air was applied to workpiece, resulted in superior results in terms of tool life [105, 110, 118, 122].

Surface roughness measurement has been considered as the primary indicator of the quality of the surface finish and is one of the most widely used methods to quantify the surface integrity of a part. According to the results of the studies, the scholars came to agreement in optimum cutting parameters for best surface quality. Mainly because of substantial negative effect of tool wear on surface quality, the cutting parameters, where minimum cutting force and tool wear are achieved, yielded minimum surface roughness. These values may be summarized as cutting speed between $V_c = 50$ –200 m/min, feedrate between $f = 100$ and 200 mm/min or $f = 0.04$ –0.12 mm/rev, and depth of cut between $a_p = 0.1$ and 0.5 mm. Application of chilled air and cryogenic cooling have been reported to decrease surface roughness mostly due to their indirect effects.

It is known that austenite phase is relatively harder and possesses a higher yield point, whereas martensite phase is softer and has a lower yield point [110]. Although machining in the austenite phase may seem unfavorable due to higher hardness value and higher flow stress, machining at martensite phase might lead to increased strain hardening. This may result in unfavorable subsurface damage in operating conditions and may lead to tensile residual stress formation and reduced fatigue life of machined components. A common result of the studies is that increase of the cutting speed resulted in less subsurface hardening [41, 42, 45, 50] because the thermal softening phenomenon takes place at higher cutting speed values and increased temperature dominates mechanical loadings. It may even cause a partial recovery effect on plastic deformations. Moreover, increased temperature causes temperature-induced phase transformation (austenitic). Accordingly, less strain hardening is observed. Conversely, attempts to keep the workpiece in martensitic structure during machining resulted in increased subsurface hardening [50, 110, 120]. This is not a desired condition except for some cases where hardened surface is desired. In addition to active workpiece phase during machining, the phase at room temperature prior to machining was reported to affect strain hardening. More significant strain hardening was reported for alloys in B19' structure at room temperature [44, 45]. Some studies, however, attributed increased hardness to austenitic to martensitic transformation-induced hardness [157] rather than strain hardening of martensite [99].

High temperature coupled with high stress around the cutting region during the machining process may affect microstructure and active phase of NiTi. Considering relatively low phase transformation temperatures of NiTi compared to other alloys, understanding machining-induced phase transformation gains more importance. Surface and subsurface layer may be affected from machining-induced phase transformation in two different ways. First, mechanical properties such as subsurface hardness may be affected as observed in some of the other difficult-to-cut materials. Secondly, special

properties such as actuation capacity, damping capacity, shape memory property, and pseudoelasticity property may be affected. These kinds of alterations may negatively affect the functional properties of NiTi, which are the primary selection criteria of SMAs in application industries like biomedical and aerospace.

Machining-induced layer of NiTi is measured by the depth of twinned layer or white layer on the post machining cross-sectional specimens. Machining-induced phase transformation is measured by XRD analysis. These two measures are indicators of permanent martensite structure [46], plastic deformation, and dislocation density [186, 187]. Increase of cutting speed resulted in a decreased machining induced layer and decreased peak broadening in XRD spectrum. When cryogenic machining is applied, with purpose to keep the workpiece in martensitic structure, machining-induced layer and peak broadening significantly increased [50, 119–121]. Increased subsurface hardening is further evidence to support these two occurrences. Increased cutting speed results in an increased strain rate in deformation zone and this raises cutting temperatures. Increased temperature along with thermal softening dominate mechanical effects. Consequently, reduced density of twins/dislocations is observed. Conversely, more dominant mechanical loads at low cutting speeds or under cryogenic cooling cause higher permanent plastic strains. Peak broadening, observed at low cutting speeds or under cryogenic cooling, proves previously described stress induced martensitic structure.

During solid-state phase transformation of NiTi, latent heat or transformation enthalpy (ΔH) can be considered as a volumetric measure of transformed material [188, 189]. As stated by Ortin and Planes [190], measurements of the heat of the martensitic transformation also include contributions from the elastic strain energy and the frictional energy dissipated during phase transformation, in addition to the chemical enthalpy. Frictional energy loss and plastic deformation during transformation essentially constitute irreversible energy [191, 192]. Large differences in cyclic behavior of cryogenically machined specimens were probably resulted from internal frictional work [31, 193]. Similarly, post machining DSC analysis showed that decrease of the cutting speed or application of cryogenic machining remarkably decreased ΔH of NiTi [50, 120, 121]. Accordingly, volume of transformed material reduced. This response was attributed to the high density of dislocations and vacancies in the crystal structure of the material [140, 143]. Moreover, substantially increased A_S and A_T transformation temperatures were observed when cryogenic cooling was applied. As suggested by Mahmud et al. [142], deformation-induced martensite stabilization is generally recognized as the increase of the transformation hysteresis via increase in reverse transformation temperature [194]. Accordingly, shift of transformation temperatures to higher values resulted from requirement of additional frictional

energy to overcome frictional stress due to stabilized martensite. Considering the fact that functional properties of NiTi mainly depend on solid-state phase transformation, lower cutting speed values or cryogenic machining may negatively affect long-term use of these materials. Furthermore, undesired functional behaviors could be observed due to excessive latent heat reduction or transformation temperature shift.

The number of studies that presented numerical models for simulating machining responses of NiTi is very limited. Simulation of solid-state phase transformation during machining process is of great importance. In this respect, only the trend of martensitic phase transformation can be simulated with the presently available FE models. A well-defined constitutive material model is required, which simulates both (1) plastic flow stress with regard to temperature, strain, strain rate, and (2) machining-induced phase transformation.

7 Utilization and future trend

Some operative advices may be derived from this study oriented toward practical applications in terms of machining conditions and parameters. When main concern is tool life or machining at higher speed values, application of cryogenic cooling would probably give favored results because of its cooling and lubrication effects. Similarly, the application of chilled air (cooling) to cutting region or MQL and chilled air together (lubrication and cooling) is expected to yield similar results. The results of the studies showed that there may be a compromise between tool life and post machining functional fatigue performance of this material. When achieving the best subsurface microstructure and functional performance is the main goal, dry cutting or MQL cutting is recommended. In this case, MQL cutting, most probably, would give better tool life results. As this material is very prone to accumulate excessive heat at the cutting region, application of preheated machining has given negative results, and it has not been suggested with current state of application knowledge. As for cutting parameters when using carbide cutting tools, the literature survey showed that cutting speed of $V_c = 100$ m/min and feedrate of $f = 0.05$ m/min may be accepted as reference values.

With the knowledge gained from the studies discussed in this paper, it looks possible to contribute application areas given in Table 1. A better understanding of machining-induced functional properties may help research and development in sectors such as aerospace or biomedical where actuation or damping performance limitation is substantially critical. Minimization of the post machining burr formation may be ensured by selection of the correct machining parameters or application of suitable machining conditions. This may help reducing the time of de-burring operations or completely remove them, which is highly favored especially for micro-

machining operations. Finding optimum process parameters for tool life, process speed, and part quality is very crucial for application sectors like automotive. This may be rendered possible by carefully studying reported literature. Accordingly, the application range of these materials may increase with increased profitability. This may further push researchers and industry to explore this material. Similarly, increased need for NiTi products may cause a demand for higher speed machining. In this case, cutting tool producers may benefit from the information discussed regarding cutting tool behavior and wear.

The manufacturing process of this promising material requires special care concerning functional properties. Yet, limited number of investigations have been carried out regarding machining effects on functional properties such as transformation temperatures, transformation enthalpy, and activation energy. More detailed studies are needed to understand these effects. There are extensive studies investigating the effects of cold forming and heat treatment on mechanical and functional properties of NiTi. With the information gained from those studies, it is possible to develop a better understanding of machining effects. Alternatively, including these methods to machining course may yield improved machining or post machining characteristics. Similarly, very few studies were conducted on effects of post processing strategies like ball burnishing or shoot peening, which are applied with an aim to eliminate internal stresses and adjust microstructure. The effects of these post processing methods on the phase transformation properties and microstructure of NiTi parts are still not well known. Likewise, more studies are needed on the phase transformation behaviors after application of non-traditional machining methods.

Tool wear stands for one of the major limiting factors for high-speed machining of NiTi. This limitation mainly arises from increased temperatures at higher speed values. Until now, surface coating of carbide cutting tools and application of cryogenic cooling have been reported to ease this problem at higher cutting speed values. Some further studies are desired in order to increase machinability rate of these materials. Some suggested methods for these potential studies may be listed as follows: use of textured cutting tools, application of multilayer coating, or using rotary turning tools. These methods have been successfully used when machining other difficult-to-cut materials.

Additive manufacturing (AM) may be a profitable production alternative to machining when producing parts with complex geometries and in small batches. Therefore, AM may be a very attractive alternative for some NiTi parts. Yet, AM of NiTi has not gained much attention so far. High cost of infrastructure investment and limitations of this process such as lack of geometric precision and thermomechanical defects may be responsible for that. However, application and research of AM process increasing exponentially.

Thermomechanical behaviors of NiTi during AM need to be more extensively investigated.

8 Conclusions

Shape memory alloys are a class of functional materials which undergo solid-state phase transformation by applied heat or stress. NiTi is the most widely employed and studied among them, owing to its superior mechanical properties and corrosion resistance in addition to its functional properties. Considering the application range of these alloys (e.g., biomedical, aerospace), final shaping of the components should be conducted precisely and with minimal damage to subsurface zone and functional properties. For this purpose, conventional machining methods are applied extensively. However, machining of these alloys is characterized by severe tool wear (i.e., severe adhesion), high specific cutting energy, and high strain hardening. Furthermore, effects of machining on microstructure and phase transformation behaviors have to be kept under control in order not to impair functional properties.

There are distinctive differences in mechanical properties between austenite and martensite. Since phase transformation temperatures of NiTi reside in a close interval around room temperature values, small variations in cutting parameters may yield significant differences. Current state-of-the-art studies showed that coated cemented carbide grade cutting tools at relatively high cutting speeds ($V_c = 100$ m/min for turning, $V_c = 200$ m/min for milling) yielded optimal results in terms of tool wear, cutting force, surface quality, machining-induced layer, and subsurface hardening. The scholars came to an agreement that the main tool wear problem, when turning these materials, is notch wear due to strain hardening. Extensive chipping and BUE was reported when milling.

Attempts to keep this material in martensitic structure during machining (i.e., application of chilled air, cryogenic cooling) resulted in less tool wear and decreased cutting forces because of the softer structure and the lower yield stress of the martensite. However, these applications also resulted in permanent plastic deformations, decreased volume of transformed material, shift of reverse transformation temperatures, deeper machining-induced layer, and increased surface hardening. All things considered, the functional properties and the machinability rate of NiTi are very sensitive to machining parameters and other machining concepts. Therefore, the machinability rate of NiTi should be assessed not only by usual machinability factors (i.e., tool wear, cutting forces, surface integrity) but also post machining functional behaviors.

Acknowledgements This work was supported by Anadolu University Scientific Research Commission (grant numbers 1706F382, 1803F068).

Publisher's Note Springer Nature remains neutral with regard to jurisdictional claims in published maps and institutional affiliations.

References

- Zainal MA, Sahlan S, Ali MSM (2015) Micromachined shape-memory-alloy microactuators and their application in biomedical devices. *Micromachines* 6(7):879–901
- Stoeckel D (1990) Shape memory actuators for automotive applications. *Mater Des* 11(6):302–307. [https://doi.org/10.1016/0261-3069\(90\)90013-A](https://doi.org/10.1016/0261-3069(90)90013-A)
- Butera F, Coda A, Vergani G, SpA SG (2007) Shape memory actuators for automotive applications. *Nanotec IT newsletter Roma: AIRI/nanotec IT:12–16*. [https://doi.org/10.1016/0261-3069\(90\)90013-A](https://doi.org/10.1016/0261-3069(90)90013-A)
- Bil C, Massey K, Abdullah EJ (2013) Wing morphing control with shape memory alloy actuators. *J Intell Mater Syst Struct* 24(7):879–898. <https://doi.org/10.1177/1045389X12471866>
- Hartl DJ, Lagoudas DC (2007) Aerospace applications of shape memory alloys. *Proc Inst Mech Eng G J aerosp eng* 221(4):535–552. <https://doi.org/10.1243/09544100JAERO211>
- Petrini L, Migliavacca F (2011) Biomedical applications of shape memory alloys. *J Metall*. <https://doi.org/10.1155/2011/501483>
- Kaya A, Kaya I, Karaca HE (2013) Radio frequency U-shape slot antenna design with NiTi shape memory alloys. *Microw Opt Technol Lett* 55(12):2976–2984. <https://doi.org/10.1002/mop.27977>
- Kaya A, Kaya I, Karaca HE (2016) U-shape slot antenna design with high-strength Ni54Ti46 alloy. *Arab J Sci Eng* 41(9):3297–3307. <https://doi.org/10.1007/s13369-015-1819-2>
- Furuya Y (1996) Design and material evaluation of shape memory composites. *J Intell Mater Syst Struct* 7(3):321–330. <https://doi.org/10.1177/1045389X9600700313>
- Kohl M (2013) Shape memory microactuators. Springer Science & Business Media.
- Kahn H, Huff M, Heuer A (1998) The TiNi shape-memory alloy and its applications for MEMS. *J Micromech Microeng* 8(3):213. <https://doi.org/10.1088/0960-1317/8/3/007>
- Wilkes KE, Liaw PK (2000) The fatigue behavior of shape-memory alloys. *JOM* 52(10):45–51. <https://doi.org/10.1007/s11837-000-0083-3>
- Huang W (2002) On the selection of shape memory alloys for actuators. *Mater Des* 23(1):11–19. [https://doi.org/10.1016/S0261-3069\(01\)00039-5](https://doi.org/10.1016/S0261-3069(01)00039-5)
- Jani JM, Leary M, Subic A, Gibson MA (2014) A review of shape memory alloy research, applications and opportunities. *Mater Des* (1980–2015) 56:1078–1113. <https://doi.org/10.1016/j.matdes.2013.11.084>
- Elahinia MH, Hashemi M, Tabesh M, Bhaduri SB (2012) Manufacturing and processing of NiTi implants: a review. *Prog Mater Sci* 57(5):911–946. <https://doi.org/10.1016/j.pmatsci.2011.11.001>
- Ryhänen J (2000) Biocompatibility of nitinol. *Minim Invasive Ther Allied Technol* 9(2):99–105. <https://doi.org/10.3109/13645700009063056>
- Ryhänen J, Niemi E, Serlo W, Niemelä E, Sandvik P, Pernu H, Salo T (1997) Biocompatibility of nickel–titanium shape memory metal and its corrosion behavior in human cell cultures. *J Biomed Mater Res* 35(4):451–457
- Shih CC, Lin SJ, Chen YL, Su YY, Lai ST, Wu GJ, Kwok CF, Chung KH (2000) The cytotoxicity of corrosion products of nitinol stent wire on cultured smooth muscle cells. *J Biomed Mater Res* 52(2):395–403
- Bahraminasab M, Sahari BB (2013) NiTi shape memory alloys, promising materials in orthopedic applications. In: Shape memory alloys—processing, characterization and applications. InTech. <https://doi.org/10.5772/48419>
- Shabalovskaya SA (2002) Surface, corrosion and biocompatibility aspects of nitinol as an implant material. *Biomed Mater Eng* 12(1):69–109
- Es-Souni M, Es-Souni M, Fischer-Brandies H (2005) Assessing the biocompatibility of NiTi shape memory alloys used for medical applications. *Anal Bioanal Chem* 381(3):557–567. <https://doi.org/10.1007/s00216-004-2888-3>
- Sun L, Huang WM (2009) Nature of the multistage transformation in shape memory alloys upon heating. *Met Sci Heat Treat* 51(11):573–578. <https://doi.org/10.1007/s11041-010-9213-x>
- Lagoudas DC (2008) Shape memory alloys. Science and Business Media, LLC
- Otsuka K, Wayman CM (1999) Shape memory materials. Cambridge University Press.
- Morgan NB (2004) Medical shape memory alloy applications—the market and its products. *Mater Sci Eng A* 378(1):16–23. <https://doi.org/10.1016/j.msea.2003.10.326>
- Massalski TB, Okamoto H, Subramanian P, Kacprzak L (1991) Binary alloy phase diagrams, (ASM International, Materials Park, OH, 1990). Google Scholar 3503
- Wu MH (2002) Fabrication of nitinol materials and components. *Mater Sci Forum* 394-395:285–292. <https://doi.org/10.4028/www.scientific.net/MSF.394-395.285>
- Shishkovsky I, Yadroitsev I, Smurov I (2012) Direct selective laser melting of nitinol powder. *Phys Procedia* 39:447–454. <https://doi.org/10.1016/j.phpro.2012.10.060>
- Miyazaki S, Kimura S, Takei F, Miura T, Otsuka K, Suzuki Y (1983) Shape memory effect and pseudoelasticity in a Ti Ni single crystal. *Scr Metall* 17(9):1057–1062. [https://doi.org/10.1016/0036-9748\(83\)90453-2](https://doi.org/10.1016/0036-9748(83)90453-2)
- Srivastava AK, Schryvers D, Van Humbeeck J (2007) Grain growth and precipitation in an annealed cold-rolled Ni50.2Ti49.8 alloy. *Intermetallics* 15(12):1538–1547. <https://doi.org/10.1016/j.intermet.2007.06.003>
- McCormick P, Liu Y (1994) Thermodynamic analysis of the martensitic transformation in NiTi—II. Effect of transformation cycling. *Acta Metall Mater* 42(7):2407–2413. [https://doi.org/10.1016/0956-7151\(94\)90319-0](https://doi.org/10.1016/0956-7151(94)90319-0)
- Miller DA, Lagoudas DC (2001) Influence of cold work and heat treatment on the shape memory effect and plastic strain development of NiTi. *Mater Sci Eng A* 308(1–2):161–175. [https://doi.org/10.1016/S0921-5093\(00\)01982-1](https://doi.org/10.1016/S0921-5093(00)01982-1)
- Carroll MC, Somsen C, Eggeler G (2004) Multiple-step martensitic transformations in Ni-rich NiTi shape memory alloys. *Scr Mater* 50(2):187–192. <https://doi.org/10.1016/j.scriptamat.2003.09.020>
- Filip P, Mazanec K (1995) Influence of work hardening and heat treatment on the substructure and deformation behaviour of TiNi shape memory alloys. *Scr Metall Mater* 32(9):1375–1380. [https://doi.org/10.1016/0956-716X\(95\)00174-T](https://doi.org/10.1016/0956-716X(95)00174-T)
- Morawiec H, Stróż D, Goryczka T, Chrobak D (1996) Two-stage martensitic transformation in a deformed and annealed NiTi alloy. *Scr Mater* 35(4):485–490. [https://doi.org/10.1016/1359-6462\(96\)00179-0](https://doi.org/10.1016/1359-6462(96)00179-0)
- Eggeler G, Hornbogen E, Yawny A, Heckmann A, Wagner M (2004) Structural and functional fatigue of NiTi shape memory alloys. *Mater Sci Eng A* 378(1):24–33. <https://doi.org/10.1016/j.msea.2003.10.327>
- Frick CP, Ortega AM, Tyber J, Maksound AEM, Maier HJ, Liu Y, Gall K (2005) Thermal processing of polycrystalline NiTi shape memory alloys. *Mater Sci Eng A* 405(1):34–49. <https://doi.org/10.1016/j.msea.2005.05.102>

38. Khaleghi F, Khalil-Allafi J, Abbasi-Chianeh V, Noori S (2013) Effect of short-time annealing treatment on the superelastic behavior of cold drawn Ni-rich NiTi shape memory wires. *J Alloys Compd* 554:32–38. <https://doi.org/10.1016/j.jallcom.2012.11.183>
39. Lei X, Rui W, Yong L (2011) The optimization of annealing and cold-drawing in the manufacture of the Ni–Ti shape memory alloy ultra-thin wire. *Int J Adv Manuf Technol* 55(9):905–910. <https://doi.org/10.1007/s00170-010-3116-2>
40. Canadinc D, Trehern W, Ozcan H, Hayrettin C, Karakoc O, Karaman I, Sun F, Chaudhry Z (2017) On the deformation response and cyclic stability of Ni50Ti35Hf15 high temperature shape memory alloy wires. *Scr Mater* 135:92–96. <https://doi.org/10.1016/j.scriptamat.2017.03.025>
41. Huang H (2004) A study of high-speed milling characteristics of nitinol. *Mater Manuf Process* 19(2):159–175. <https://doi.org/10.1081/AMP-120029849>
42. Weinert K, Petzoldt V (2004) Machining of NiTi based shape memory alloys. *Mater Sci Eng A* 378(1):180–184. <https://doi.org/10.1016/j.msea.2003.10.344>
43. Guo Y, Klink A, Fu C, Snyder J (2013) Machinability and surface integrity of nitinol shape memory alloy. *CIRP Ann Manuf Technol* 62(1):83–86. <https://doi.org/10.1016/j.cirp.2013.03.004>
44. Lin H, Lin K, Chen Y (2000) A study on the machining characteristics of TiNi shape memory alloys. *J Mater Process Technol* 105(3):327–332. [https://doi.org/10.1016/S0924-0136\(00\)00656-7](https://doi.org/10.1016/S0924-0136(00)00656-7)
45. Weinert K, Petzoldt V, Kötter D, Buschka M (2004) Drilling of NiTi shape memory alloys. *Mater Werkst* 35(5):338–341
46. Piquard R, D'Acunto A, Laheurte P, Dudzinski D (2014) Micro-end milling of NiTi biomedical alloys, burr formation and phase transformation. *Precis Eng* 38(2):356–364. <https://doi.org/10.1016/j.precisioneng.2013.11.006>
47. Kong M, Axinte D, Voice W (2011) Challenges in using waterjet machining of NiTi shape memory alloys: an analysis of controlled-depth milling. *J Mater Process Technol* 211(6):959–971
48. Porter G, Liaw P, Tiegts T, Wu K (2001) Fatigue and fracture behavior of nickel–titanium shape-memory alloy reinforced aluminum composites. *Mater Sci Eng A* 314(1):186–193. [https://doi.org/10.1016/S0921-5093\(00\)01915-8](https://doi.org/10.1016/S0921-5093(00)01915-8)
49. Biermann D, Kahleiss F, Surmann T (2009) Micromilling of NiTi shape-memory alloys with ball nose cutters. *Mater Manuf Process* 24(12):1266–1273. <https://doi.org/10.1080/10426910903129935>
50. Kaynak Y, Karaca H, Jawahir I (2015) Cutting speed dependent microstructure and transformation behavior of NiTi alloy in dry and cryogenic machining. *J Mater Eng Perform* 24(1):452–460. <https://doi.org/10.1007/s11665-014-1247-6>
51. Theisen W, Schuermann A (2004) Electro discharge machining of nickel–titanium shape memory alloys. *Mater Sci Eng A* 378(1):200–204. <https://doi.org/10.1016/j.msea.2003.09.115>
52. Uppal N, Shiakolas PS (2008) Micromachining characteristics of NiTi based shape memory alloy using femtosecond laser. *J Manuf Sci Eng* 130(3):031117. <https://doi.org/10.1007/s00170-015-7598-9>
53. Huang H, Zheng H, Liu Y (2005) Experimental investigations of the machinability of Ni50. 6Ti49. 4 alloy. *Smart Mater Struct* 14(5):S297. <https://doi.org/10.1088/0964-1726/14/5/019>
54. Biermann D, Kahleiss F, Krebs E, Upmeier T (2011) A study on micro-machining technology for the machining of NiTi: five-axis micro-milling and micro deep-hole drilling. *J Mater Eng Perform* 20(4):745–751. <https://doi.org/10.1007/s11665-010-9796-9>
55. Handbook A (1989) Volume 16: machining. ASM International Handbook Committee. ASM International, Electronic
56. Handbook M (1990) Vol. 2—properties and selection: nonferrous alloys and special-purpose materials. ASM Inter 1119–1124
57. Ismail F, Mridha S Microstructure–hardness relationship of Inconel 718 compressor blade heat treated at different conditions. In: *Advanced Materials Research*, 2012. Trans Tech Publ, p 459–462. doi:<https://doi.org/10.4028/www.scientific.net/AMR.576.459>
58. Stanford MK (2012) Thermophysical properties of 60-nitinol for mechanical component applications
59. Stanford MK (2016) Hardness and microstructure of binary and ternary nitinol compounds
60. Ezugwu EO, Wang ZM (1997) Titanium alloys and their machinability—a review. *J Mater Process Technol* 68(3):262–274. [https://doi.org/10.1016/S0924-0136\(96\)00030-1](https://doi.org/10.1016/S0924-0136(96)00030-1)
61. Jianxin D, Yousheng L, Wenlong S (2008) Diffusion wear in dry cutting of Ti–6Al–4V with WC/co carbide tools. *Wear* 265(11):1776–1783. <https://doi.org/10.1016/j.wear.2008.04.024>
62. Kitagawa T, Kubo A, Maekawa K (1997) Temperature and wear of cutting tools in high-speed machining of Inconel 718 and Ti–6Al–6V–2Sn. *Wear* 202(2):142–148. [https://doi.org/10.1016/S0043-1648\(96\)07255-9](https://doi.org/10.1016/S0043-1648(96)07255-9)
63. Ezugwu E, Da Silva R, Bonney J, Machado A (2005) Evaluation of the performance of CBN tools when turning Ti–6Al–4V alloy with high pressure coolant supplies. *Int J Mach Tools Manuf* 45(9):1009–1014. <https://doi.org/10.1016/j.ijmactools.2004.11.027>
64. Grzesik W, Zalisz Z, Krol S, Nieslony P (2006) Investigations on friction and wear mechanisms of the PVD-TiAlN coated carbide in dry sliding against steels and cast iron. *Wear* 261(11):1191–1200. <https://doi.org/10.1016/j.wear.2006.03.004>
65. Wolfe G, Petrosky C, Quinto D (1986) The role of hard coatings in carbide milling tools. *J Vac Sci Technol A* 4(6):2747–2754. <https://doi.org/10.1116/1.573673>
66. Ezugwu EO, Wang ZM, Okeke CI (1999) Tool life and surface integrity when machining Inconel 718 with PVD- and CVD-coated tools. *Tribol Trans* 42(2):353–360. <https://doi.org/10.1080/10402009908982228>
67. Mehrpouya M, Shahedin AM, Daood Salman Dawood S, Kamal Ariffin A (2017) An investigation on the optimum machinability of NiTi based shape memory alloy. *Mater Manuf Process* 1–8. doi:<https://doi.org/10.1080/10426914.2017.1279290>
68. Xavier MA, Manohar M, Jeyapandiarajan P, Madhukar PM (2017) Tool wear assessment during machining of Inconel 718. *Proced Eng* 174:1000–1008. <https://doi.org/10.1016/j.proeng.2017.01.252>
69. Davoodi B, Hosseini Tazehkandi A (2016) Cutting forces and surface roughness in wet machining of Inconel alloy 738 with coated carbide tool. *Proc Inst Mech Eng B J Eng Manuf* 230(2):215–226. <https://doi.org/10.1177/0954405414542990>
70. Thakur A, Gangopadhyay S (2016) Dry machining of nickel-based super alloy as a sustainable alternative using TiN/TiAlN coated tool. *J Clean Prod* 129:256–268. <https://doi.org/10.1016/j.jclepro.2016.04.074>
71. Bhatt A, Attia H, Vargas R, Thomson V (2010) Wear mechanisms of WC coated and uncoated tools in finish turning of Inconel 718. *Tribol Int* 43(5–6):1113–1121. <https://doi.org/10.1016/j.triboint.2009.12.053>
72. Sharif S, Rahim EA (2007) Performance of coated- and uncoated-carbide tools when drilling titanium alloy—Ti–6Al4V. *J Mater Process Technol* 185(1):72–76. <https://doi.org/10.1016/j.jmatprotec.2006.03.142>
73. Zhang S, Li JF, Deng JX, Li YS (2008) Investigation on diffusion wear during high-speed machining Ti–6Al–4V alloy with straight tungsten carbide tools. *Int J Adv Manuf Technol* 44(1):17. <https://doi.org/10.1007/s00170-008-1803-z>
74. Choudhury IA, El-Baradie MA (1998) Machinability of nickel-base super alloys: a general review. *J Mater Process Technol* 77(1):278–284. [https://doi.org/10.1016/S0924-0136\(97\)00429-9](https://doi.org/10.1016/S0924-0136(97)00429-9)

75. Richards N, Aspinwall D (1989) Use of ceramic tools for machining nickel based alloys. *Int J Mach Tools Manuf* 29(4):575–588. [https://doi.org/10.1016/0890-6955\(89\)90072-2](https://doi.org/10.1016/0890-6955(89)90072-2)
76. Ding X, Liew WYH, Liu XD (2005) Evaluation of machining performance of MMC with PCBN and PCD tools. *Wear* 259(7):1225–1234. <https://doi.org/10.1016/j.wear.2005.02.094>
77. Ezugwu EO, Bonney J, Da Silva RB, Çakir O (2007) Surface integrity of finished turned Ti–6Al–4V alloy with PCD tools using conventional and high pressure coolant supplies. *Int J Mach Tools Manuf* 47(6):884–891. <https://doi.org/10.1016/j.ijmactools.2006.08.005>
78. Altin A, Nalbant M, Taskesen A (2007) The effects of cutting speed on tool wear and tool life when machining Inconel 718 with ceramic tools. *Mater Des* 28(9):2518–2522. <https://doi.org/10.1016/j.matdes.2006.09.004>
79. Li L, He N, Wang M, Wang ZG (2002) High speed cutting of Inconel 718 with coated carbide and ceramic inserts. *J Mater Process Technol* 129(1):127–130. [https://doi.org/10.1016/S0924-0136\(02\)00590-3](https://doi.org/10.1016/S0924-0136(02)00590-3)
80. Ezugwu EO, Bonney J, Fadare DA, Sales WF (2005) Machining of nickel-base, Inconel 718, alloy with ceramic tools under finishing conditions with various coolant supply pressures. *J Mater Process Technol* 162–163:609–614. <https://doi.org/10.1016/j.jmatprotec.2005.02.144>
81. Kertesz J, Pryor RJ, Richerson DW, Cutler RA (1988) Machining titanium alloys with ceramic tools. *JOM* 40(5):50–51. <https://doi.org/10.1007/bf03258917>
82. Weinert K, Petzoldt V, Kötter D (2004) Turning and drilling of NiTi shape memory alloys. *CIRP Ann Manuf Technol* 53(1):65–68. [https://doi.org/10.1016/S0007-8506\(07\)60646-5](https://doi.org/10.1016/S0007-8506(07)60646-5)
83. Zhou J, Bushlya V, Avdovic P, Ståhl JE (2012) Study of surface quality in high speed turning of Inconel 718 with uncoated and coated CBN tools. *Int J Adv Manuf Technol* 58(1):141–151. <https://doi.org/10.1007/s00170-011-3374-7>
84. Bushlya V, Zhou J, Ståhl J-E (2012) Effect of cutting conditions on machinability of superalloy Inconel 718 during high speed turning with coated and uncoated PCBN tools. *Proced CIRP* 3:370–375
85. Costes J-P, Guillet Y, Poulachon G, Dessoly M (2007) Tool-life and wear mechanisms of CBN tools in machining of Inconel 718. *Int J Mach Tools Manuf* 47(7–8):1081–1087. <https://doi.org/10.1016/j.ijmactools.2006.09.031>
86. Tanaka H, Sugihara T, Enomoto T (2016) High speed machining of Inconel 718 focusing on wear behaviors of PCBN cutting tool. *Proced Cirp* 46:545–548. <https://doi.org/10.1016/j.procir.2016.03.120>
87. Arunachalam R, Mannan M, Spowage A (2004) Residual stress and surface roughness when facing age hardened Inconel 718 with CBN and ceramic cutting tools. *Int J Mach Tools Manuf* 44(9):879–887. <https://doi.org/10.1016/j.ijmactools.2004.02.016>
88. Corduan N, Himbart T, Poulachon G, Dessoly M, Lambertin M, Vigneau J, Payoux B (2003) Wear mechanisms of new tool materials for Ti–6Al–4V high performance machining. *CIRP Ann* 52(1):73–76. [https://doi.org/10.1016/S0007-8506\(07\)60534-4](https://doi.org/10.1016/S0007-8506(07)60534-4)
89. Dogra M, Sharma VS, Sachdeva A, Suri NM, Dureja JS (2010) Tool wear, chip formation and workpiece surface issues in CBN hard turning: a review. *Int J Precis Eng Manuf* 11(2):341–358. <https://doi.org/10.1007/s12541-010-0040-1>
90. Zoya Z, Krishnamurthy R (2000) The performance of CBN tools in the machining of titanium alloys. *J Mater Process Technol* 100(1–3):80–86. [https://doi.org/10.1016/S0924-0136\(99\)00464-1](https://doi.org/10.1016/S0924-0136(99)00464-1)
91. Zareena AR, Rahman M, Wong Y (2005) Binderless CBN tools, a breakthrough for machining titanium alloys. *J Manuf Sci Eng* 127(2):277–279
92. Hirosaki K, Shintani K, Kato H, Asakura F, Matsuo K (2004) High speed machining of bio-titanium alloy with a binder-less PcBN tool. *JSME Int J Ser C Mech Syst Mach Elem Manuf* 47(1):14–20. <https://doi.org/10.1299/jsmec.47.14>
93. Amin AKMN, Ismail AF, Nor Khairusshima MK (2007) Effectiveness of uncoated WC–Co and PCD inserts in end milling of titanium alloy—Ti–6Al–4V. *J Mater Process Technol* 192–193:147–158. <https://doi.org/10.1016/j.jmatprotec.2007.04.095>
94. Nabhani F (2001) Machining of aerospace titanium alloys. *Robot Comput Integr Manuf* 17(1–2):99–106. [https://doi.org/10.1016/S0736-5845\(00\)00042-9](https://doi.org/10.1016/S0736-5845(00)00042-9)
95. Honghua S, Peng L, Yucan F, Jiuhua X (2012) Tool life and surface integrity in high-speed milling of titanium alloy TA15 with PCD/PCBN tools. *Chin J Aeronaut* 25(5):784–790. [https://doi.org/10.1016/S1000-9361\(11\)60445-7](https://doi.org/10.1016/S1000-9361(11)60445-7)
96. Oosthuizen GA, Akdogan G, Treurnicht N (2011) The performance of PCD tools in high-speed milling of Ti6Al4V. *Int J Adv Manuf Technol* 52(9):929–935. <https://doi.org/10.1007/s00170-010-2804-2>
97. Astakhov VP, Davim JP (2008) Tools (geometry and material) and tool wear. *Machining*. Springer, In, pp 29–57
98. Poulachon G, Moisan A, Jawahir I (2001) Tool-wear mechanisms in hard turning with polycrystalline cubic boron nitride tools. *Wear* 250(1–12):576–586. [https://doi.org/10.1016/S0043-1648\(01\)00609-3](https://doi.org/10.1016/S0043-1648(01)00609-3)
99. Kuppuswamy R, Yui A (2015) High-speed micromachining characteristics for the NiTi shape memory alloys. *Int J Adv Manuf Technol*. <https://doi.org/10.1007/s00170-015-7598-9>
100. Zhu D, Zhang X, Ding H (2013) Tool wear characteristics in machining of nickel-based superalloys. *Int J Mach Tools Manuf* 64:60–77
101. Arrazola P-J, Garay A, Iriarte L-M, Armendia M, Marya S, Le Maitre F (2009) Machinability of titanium alloys (Ti6Al4V and Ti555. 3). *J Mater Process Technol* 209(5):2223–2230. <https://doi.org/10.1016/j.jmatprotec.2008.06.020>
102. Zhuang K, Zhu D, Zhang X, Ding H (2014) Notch wear prediction model in turning of Inconel 718 with ceramic tools considering the influence of work hardened layer. *Wear* 313(1–2):63–74. <https://doi.org/10.1016/j.wear.2014.02.007>
103. Ezugwu E, Wang Z, Machado A (1999) The machinability of nickel-based alloys: a review. *J Mater Process Technol* 86(1–3):1–16. [https://doi.org/10.1016/S0924-0136\(98\)00314-8](https://doi.org/10.1016/S0924-0136(98)00314-8)
104. Clayton P (1993) Tribological behavior of a titanium-nickel alloy. *Wear* 162–164(Part A):202–210. [https://doi.org/10.1016/0043-1648\(93\)90502-D](https://doi.org/10.1016/0043-1648(93)90502-D)
105. Kaynak Y, Karaca H, Noebe R, Jawahir I (2013) Tool-wear analysis in cryogenic machining of NiTi shape memory alloys: a comparison of tool-wear performance with dry and MQL machining. *Wear* 306(1):51–63. <https://doi.org/10.1016/j.wear.2013.05.011>
106. Kaynak Y, Karaca HE, Noebe RD, Jawahir IS (2013) Analysis of tool-wear and cutting force components in dry, preheated, and cryogenic machining of NiTi shape memory alloys. *Proced CIRP* 8(Supplement C):498–503. <https://doi.org/10.1016/j.procir.2013.06.140>
107. Narutaki N, Yamane Y, Hayashi K, Kitagawa T, Uehara K (1993) High-speed machining of Inconel 718 with ceramic tools. *CIRP Annals-Manufacturing Technology* 42(1):103–106. [https://doi.org/10.1016/S0007-8506\(07\)62402-0](https://doi.org/10.1016/S0007-8506(07)62402-0)
108. Arunachalam R, Mannan M (2000) Machinability of nickel-based high temperature alloys. *Mach Sci Technol* 4(1):127–168. <https://doi.org/10.1080/10940340008945703>
109. Ghani A, Barrow G, De Barr A (1985) Tool failure at exit during interrupted cutting. *CIRP Ann Manuf Technol* 34(1):71–74. [https://doi.org/10.1016/S0007-8506\(07\)61726-0](https://doi.org/10.1016/S0007-8506(07)61726-0)

110. Zailani ZA, Mativenga PT (2016) Effects of chilled air on machinability of NiTi shape memory alloy. *Proced CIRP* 45:207–210. <https://doi.org/10.1016/j.procir.2016.02.156>
111. Adharapurapu RR, Jiang F, Bingert JF, Vecchio KS (2010) Influence of cold work and texture on the high-strain-rate response of nitinol. *Mater Sci Eng A* 527(20):5255–5267. <https://doi.org/10.1016/j.msea.2010.04.076>
112. Lin H, Lin K, Cheng I (2001) The electro-discharge machining characteristics of TiNi shape memory alloys. *J Mater Sci* 36(2):399–404
113. Huang H, Zheng H, Lim G (2004) Femtosecond laser machining characteristics of nitinol. *Appl Surf Sci* 228(1):201–206. <https://doi.org/10.1016/j.apsusc.2004.01.018>
114. Axinte D, Kong M (2009) An integrated monitoring method to supervise waterjet machining. *CIRP Ann Manuf Technol* 58(1):303–306. <https://doi.org/10.1016/j.cirp.2009.03.022>
115. Kong M, Axinte D (2009) Response of titanium aluminide alloy to abrasive waterjet cutting: geometrical accuracy and surface integrity issues versus process parameters. *Proc Inst Mech Eng B J Eng Manuf* 223(1):19–42. <https://doi.org/10.1243/09544054JEM1226>
116. Frotscher M, Kahleiss F, Simon T, Biermann D, Eggeler G (2011) Achieving small structures in thin NiTi sheets for medical applications with water jet and micro machining: a comparison. *J Mater Eng Perform* 20(4):776–782. <https://doi.org/10.1007/s11665-010-9789-8>
117. Hattori S, Tainaka A (2007) Cavitation erosion of Ti–Ni base shape memory alloys. *Wear* 262(1):191–197. <https://doi.org/10.1016/j.wear.2006.05.012>
118. Kaynak Y, Robertson SW, Karaca HE, Jawahir IS (2015) Progressive tool-wear in machining of room-temperature austenitic NiTi alloys: the influence of cooling/lubricating, melting, and heat treatment conditions. *J Mater Process Technol* 215(Supplement C):95–104. <https://doi.org/10.1016/j.jmatprotec.2014.07.015>
119. Kaynak Y (2014) Machining and phase transformation response of room-temperature austenitic NiTi shape memory alloy. *J Mater Eng Perform* 23(9):3354–3360. <https://doi.org/10.1007/s11665-014-1058-9>
120. Kaynak Y, Tobe H, Noebe R, Karaca H, Jawahir I (2014) The effects of machining on the microstructure and transformation behavior of NiTi alloy. *Scr Mater* 74:60–63. <https://doi.org/10.1016/j.scriptamat.2013.10.023>
121. Kaynak Y, Huang B, Karaca H, Jawahir I (2017) Surface characteristics of machined NiTi shape memory alloy: the effects of cryogenic cooling and preheating conditions. *J Mater Eng Perform* 26(7):3597–3606. <https://doi.org/10.1007/s11665-017-2791-7>
122. Kaynak Y, Karaca HE, Noebe RD, Jawahir I (2015) The effect of active phase of the work material on machining performance of a NiTi shape memory alloy. *Metall Mater Trans A* 46(6):2625–2636. <https://doi.org/10.1007/s11661-015-2828-1>
123. Ezugwu EO, Bonney J, Yamane Y (2003) An overview of the machinability of aeroengine alloys. *J Mater Process Technol* 134(2):233–253. [https://doi.org/10.1016/S0924-0136\(02\)01042-7](https://doi.org/10.1016/S0924-0136(02)01042-7)
124. Pusavec F, Hamdi H, Kopac J, Jawahir I (2011) Surface integrity in cryogenic machining of nickel based alloy—Inconel 718. *J Mater Process Technol* 211(4):773–783. <https://doi.org/10.1016/j.jmatprotec.2010.12.013>
125. Bermingham M, Kirsch J, Sun S, Palanisamy S, Dargusch M (2011) New observations on tool life, cutting forces and chip morphology in cryogenic machining Ti–6Al–4V. *Int J Mach Tools Manuf* 51(6):500–511. <https://doi.org/10.1016/j.ijmachtools.2011.02.009>
126. Hong SY, Ding Y, W-c J (2001) Friction and cutting forces in cryogenic machining of Ti–6Al–4V. *Int J Mach Tools Manuf* 41(15):2271–2285. [https://doi.org/10.1016/S0890-6955\(01\)00029-3](https://doi.org/10.1016/S0890-6955(01)00029-3)
127. Ding H, Shin YC (2013) Improvement of machinability of Waspalloy via laser-assisted machining. *Int J Adv Manuf Technol* 1–12. <https://doi.org/10.1007/s00170-012-4012-8>
128. Attia H, Tavakoli S, Vargas R, Thomson V (2010) Laser-assisted high-speed finish turning of superalloy Inconel 718 under dry conditions. *CIRP Ann* 59(1):83–88. <https://doi.org/10.1016/j.cirp.2010.03.093>
129. Parida AK, Maity K (2017) Effect of nose radius on forces, and process parameters in hot machining of Inconel 718 using finite element analysis. *Eng Sci Technol Int J* 20(2):687–693. <https://doi.org/10.1016/j.jestech.2016.10.006>
130. Zhuang K, Zhang X, Zhu D, Ding H (2015) Employing preheating- and cooling-assisted technologies in machining of Inconel 718 with ceramic cutting tools: towards reducing tool wear and improving surface integrity. *Int J Adv Manuf Technol* 80(9):1815–1822. <https://doi.org/10.1007/s00170-015-7153-8>
131. Merchant ME (1945) Mechanics of the metal cutting process. I. Orthogonal cutting and a type 2 chip. *J Appl Phys* 16(5):267–275
132. Sugihara T, Enomoto T (2015) High speed machining of Inconel 718 focusing on tool surface topography of CBN tool. *Proced Manuf* 1(Supplement C):675–682. <https://doi.org/10.1016/j.promfg.2015.09.010>
133. Khan SA, Soo SL, Aspinwall DK, Sage C, Harden P, Fleming M, White A, M'Saoubi R (2012) Tool wear/life evaluation when finish turning Inconel 718 using PCBN tooling. *Proced CIRP* 1(Supplement C):283–288. <https://doi.org/10.1016/j.procir.2012.04.051>
134. Rao GA, Kumar M, Srinivas M, Sarma D (2003) Effect of standard heat treatment on the microstructure and mechanical properties of hot isostatically pressed superalloy inconel 718. *Mater Sci Eng A* 355(1):114–125. [https://doi.org/10.1016/S0921-5093\(03\)00079-0](https://doi.org/10.1016/S0921-5093(03)00079-0)
135. Kieback B, Neubrand A, Riedel H (2003) Processing techniques for functionally graded materials. *Mater Sci Eng A* 362(1):81–106. [https://doi.org/10.1016/S0921-5093\(03\)00578-1](https://doi.org/10.1016/S0921-5093(03)00578-1)
136. Ramesh A, Melkote S, Allard L, Riester L, Watkins T (2005) Analysis of white layers formed in hard turning of AISI 52100 steel. *Mater Sci Eng A* 390(1–2):88–97. <https://doi.org/10.1016/j.msea.2004.08.052>
137. Moberly WJ, Proft JL, Duerig TW, Sinclair R (1990) Deformation, twinning and thermo-mechanical strengthening of Ti50Ni47Fe3. *Acta Metall Mater* 38(12):2601–2612. [https://doi.org/10.1016/0956-7151\(90\)90272-I](https://doi.org/10.1016/0956-7151(90)90272-I)
138. Ii S, Yamauchi K, Maruhashi Y, Nishida M (2003) Direct evidence of correlation between {201}B19' and {114}B2 deformation twins in Ti–Ni shape memory alloy. *Scr Mater* 49(7):723–727. [https://doi.org/10.1016/S1359-6462\(03\)00356-7](https://doi.org/10.1016/S1359-6462(03)00356-7)
139. Morawiec H, Stroz D, Chrobak D (1995) Effect of deformation and thermal treatment of NiTi alloy on transition sequence. *J Phys IV* 5(C2):C2–205–C202–210. <https://doi.org/10.1051/jp4:1995232>
140. Miller DA, Lagoudas DC (2000) Thermomechanical characterization of NiTiCu and NiTi SMA actuators: influence of plastic strains. *Smart Mater Struct* 9(5):640. <https://doi.org/10.1088/0964-1726/9/5/308>
141. De la Flor S, Urbina C, Ferrando F (2009) Effect of mechanical cycling on stabilizing the transformation behaviour of NiTi shape memory alloys. *J Alloys Compd* 469(1–2):343–349. <https://doi.org/10.1016/j.jallcom.2008.01.140>
142. Mahmud AS, Yang H, Tee S, Rio G, Liu Y (2008) Effect of annealing on deformation-induced martensite stabilisation of NiTi. *Intermetallics* 16(2):209–214. <https://doi.org/10.1016/j.intermet.2007.09.003>

143. Lin H, Wu S-K, Chou T, Kao H (1991) The effects of cold rolling on the martensitic transformation of an equiatomic TiNi alloy. *Acta Metall Mater* 39(9):2069–2080. [https://doi.org/10.1016/0956-7151\(91\)90177-3](https://doi.org/10.1016/0956-7151(91)90177-3)
144. Sarwar M, Persson M, Hellbergh H, Haider J (2009) Measurement of specific cutting energy for evaluating the efficiency of bandsawing different workpiece materials. *Int J Mach Tools Manuf* 49(12):958–965. <https://doi.org/10.1016/j.ijmachtools.2009.06.008>
145. Rodrigues AR, Coelho RT (2007) Influence of the tool edge geometry on specific cutting energy at high-speed cutting. *J Braz Soc Mech Sci Eng* 29(3):279–283. <https://doi.org/10.1590/S1678-58782007000300007>
146. Sreejith P, Krishnamurthy R, Malhotra S, Narayanasamy K (2000) Evaluation of PCD tool performance during machining of carbon/phenolic ablative composites. *J Mater Process Technol* 104(1):53–58. [https://doi.org/10.1016/S0924-0136\(00\)00549-5](https://doi.org/10.1016/S0924-0136(00)00549-5)
147. Chou YK, Song H (2004) Tool nose radius effects on finish hard turning. *J Mater Process Technol* 148(2):259–268. <https://doi.org/10.1016/j.jmatprotec.2003.10.029>
148. Wu S, Lin H, Chen C (1999) A study on the machinability of a Ti 49.6 Ni 50.4 shape memory alloy. *Mater Lett* 40(1):27–32
149. Kohl M, Just E, Pflöging W, Miyazaki S (2000) SMA microgripper with integrated antagonism. *Sensors Actuators A Phys* 83(1):208–213. [https://doi.org/10.1016/S0924-4247\(99\)00385-4](https://doi.org/10.1016/S0924-4247(99)00385-4)
150. Shishkovsky I, Volova L, Kuznetsov M, Morozov YG, Parkin I (2008) Porous biocompatible implants and tissue scaffolds synthesized by selective laser sintering from Ti and NiTi. *J Mater Chem* 18(12):1309–1317. <https://doi.org/10.1039/B715313A>
151. Weinert K, Petzoldt V (2008) Machining NiTi micro-parts by micro-milling. *Mater Sci Eng A* 481–482(Supplement C):672–675. <https://doi.org/10.1016/j.msea.2006.10.220>
152. Fu Y, Du H, Huang W, Zhang S, Hu M (2004) TiNi-based thin films in MEMS applications: a review. *Sensors Actuators A Phys* 112(2–3):395–408. <https://doi.org/10.1016/j.sna.2004.02.019>
153. Aramcharoen A, Mativenga P (2009) Size effect and tool geometry in micromilling of tool steel. *Precis Eng* 33(4):402–407. <https://doi.org/10.1016/j.precisioneng.2008.11.002>
154. Kale A, Khanna N (2017) A review on cryogenic machining of super alloys used in aerospace industry. *Proced Manuf* 7:191–197. <https://doi.org/10.1016/j.promfg.2016.12.047>
155. Yuan S, Yan L, Liu W, Liu Q (2011) Effects of cooling air temperature on cryogenic machining of Ti–6Al–4V alloy. *J Mater Process Technol* 211(3):356–362. <https://doi.org/10.1016/j.jmatprotec.2010.10.009>
156. Hong SY, Markus I, W-c J (2001) New cooling approach and tool life improvement in cryogenic machining of titanium alloy Ti-6Al-4V. *Int J Mach Tools Manuf* 41(15):2245–2260
157. Brinson LC, Schmidt I, Lammerring R (2004) Stress-induced transformation behavior of a polycrystalline NiTi shape memory alloy: micro and macromechanical investigations via in situ optical microscopy. *J Mech Phys Solids* 52(7):1549–1571. <https://doi.org/10.1016/j.jmps.2004.01.001>
158. Markopoulos AP (2012) Finite element method in machining processes. Springer Science & Business Media.
159. Kaynak Y, Manchiraju S, Jawahir I (2015) Modeling and simulation of machining-induced surface integrity characteristics of NiTi alloy. *Proced CIRP* 31:557–562. <https://doi.org/10.1016/j.procir.2015.03.071>
160. Li Q, Yu J-Y, Mu B-C, Sun X-D (2006) BP neural network prediction of the mechanical properties of porous NiTi shape memory alloy prepared by thermal explosion reaction. *Mater Sci Eng A* 419(1):214–217. <https://doi.org/10.1016/j.msea.2005.12.027>
161. Nemat-Nasser S, Su Y, Guo W-G, Isaacs J (2005) Experimental characterization and micromechanical modeling of superelastic response of a porous NiTi shape-memory alloy. *J Mech Phys Solids* 53(10):2320–2346. <https://doi.org/10.1016/j.jmps.2005.03.009>
162. Ashrafi MJ, Arghavani J, Naghdabadi R, Sohrabpour S, Auricchio F (2016) Theoretical and numerical modeling of dense and porous shape memory alloys accounting for coupling effects of plasticity and transformation. *Int J Solids Struct* 88–89:248–262. <https://doi.org/10.1016/j.ijsolstr.2016.03.003>
163. Williams KA, Chiu GTC, Bernhard RJ (2005) Dynamic modeling of a shape memory alloy adaptive tuned vibration absorber. *J Sound Vib* 280(1):211–234. <https://doi.org/10.1016/j.jsv.2003.12.040>
164. Paradis A, Terriault P, Brailovski V (2009) Modeling of residual strain accumulation of NiTi shape memory alloys under uniaxial cyclic loading. *Comput Mater Sci* 47(2):373–383. <https://doi.org/10.1016/j.commatsci.2009.08.013>
165. Lagoudas D, Hartl D, Chemisky Y, Machado L, Popov P (2012) Constitutive model for the numerical analysis of phase transformation in polycrystalline shape memory alloys. *Int J Plast* 32–33: 155–183. <https://doi.org/10.1016/j.ijplas.2011.10.009>
166. Petrini L, Migliavacca F, Massarotti P, Schievano S, Dubini G, Auricchio F (2005) Computational studies of shape memory alloy behavior in biomedical applications. *J Biomech Eng* 127(4):716–725. <https://doi.org/10.1115/1.1934203>
167. Umbrello D (2008) Finite element simulation of conventional and high speed machining of Ti6Al4V alloy. *J Mater Process Technol* 196(1):79–87. <https://doi.org/10.1016/j.jmatprotec.2007.05.007>
168. Oezkaya E, Biermann D (2018) A new reverse engineering method to combine FEM and CFD simulation three-dimensional insight into the chipping zone during the drilling of Inconel 718 with internal cooling. *Mach Sci Technol* 1–18. doi:<https://doi.org/10.1080/10910344.2017.1415933>
169. Oezkaya E, Beer N, Biermann D (2016) Experimental studies and CFD simulation of the internal cooling conditions when drilling Inconel 718. *Int J Mach Tools Manuf* 108:52–65. <https://doi.org/10.1016/j.ijmachtools.2016.06.003>
170. Beer N, Özkaya E, Biermann D (2014) Drilling of Inconel 718 with geometry-modified twist drills. *Procedia CIRP* 24:49–55. <https://doi.org/10.1016/j.procir.2014.07.124>
171. Biermann D, Bückler M, Tiffe M, Özkaya E (2017) Experimental investigations for a simulative optimization of the cutting edge design of twist drills used in the machining of Inconel 718. *Proced Manuf* 14:8–16. <https://doi.org/10.1016/j.promfg.2017.11.002>
172. Chen G, Ren C, Yang X, Jin X, Guo T (2011) Finite element simulation of high-speed machining of titanium alloy (Ti–6Al–4V) based on ductile failure model. *Int J Adv Manuf Technol* 56(9):1027–1038. <https://doi.org/10.1007/s00170-011-3233-6>
173. Usui E, Shirakashi T, Kitagawa T (1978) Analytical prediction of three dimensional cutting process—part 3: cutting temperature and crater wear of carbide tool. *J Eng Ind* 100(2):236–243. <https://doi.org/10.1115/1.3439415>
174. Thepsonthi T, Özel T (2013) Experimental and finite element simulation based investigations on micro-milling Ti-6Al-4V titanium alloy: effects of cBN coating on tool wear. *J Mater Process Technol* 213(4):532–542. <https://doi.org/10.1016/j.jmatprotec.2012.11.003>
175. Ranganath S, Guo C, Hegde P (2009) A finite element modeling approach to predicting white layer formation in nickel superalloys. *CIRP Ann* 58(1):77–80. <https://doi.org/10.1016/j.cirp.2009.03.109>
176. Ozel T, Llanos I, Soriano J, Arrazola PJ (2011) 3D finite element modelling of chip formation process for machining INCONEL 718: comparison of FE software predictions. *Mach Sci Technol* 15(1):21–46. <https://doi.org/10.1080/10910344.2011.557950>

177. Mitrofanov AV, Babitsky VI, Silberschmidt VV (2004) Finite element analysis of ultrasonically assisted turning of Inconel 718. *J Mater Process Technol* 153–154:233–239. <https://doi.org/10.1016/j.jmatprotec.2004.04.299>
178. Özel T, Ulutan D (2012) Prediction of machining induced residual stresses in turning of titanium and nickel based alloys with experiments and finite element simulations. *CIRP Ann* 61(1):547–550. <https://doi.org/10.1016/j.cirp.2012.03.100>
179. Jafarian F, Imaz Ciaran M, Umbrello D, Arrazola PJ, Filice L, Amirabadi H (2014) Finite element simulation of machining Inconel 718 alloy including microstructure changes. *Int J Mech Sci* 88:110–121. <https://doi.org/10.1016/j.ijmecsci.2014.08.007>
180. Uhlmann E, von der Schulenburg MG, Zettier R (2007) Finite element modeling and cutting simulation of Inconel 718. *CIRP Ann* 56(1):61–64. <https://doi.org/10.1016/j.cirp.2007.05.017>
181. Shaw MC, Cookson J (1984) *Metal cutting principles*. Clarendon press Oxford,
182. Ramesh A, Melkote SN (2008) Modeling of white layer formation under thermally dominant conditions in orthogonal machining of hardened AISI 52100 steel. *Int J Mach Tools Manuf* 48(3–4):402–414. <https://doi.org/10.1016/j.ijmactools.2007.09.007>
183. Schulze V, Michna J, Zanger F, Pabst R (2011) Modeling the process-induced modifications of the microstructure of work piece surface zones in cutting processes. In: *Advanced Materials Research*. Trans Tech Publ, p 371–380. doi:<https://doi.org/10.4028/www.scientific.net/AMR.223.371>
184. Auricchio F, Taylor R (1996) Shape-memory-alloy superelastic behavior: 3D finite-element simulations. In: *Proceedings-SPIE the international society for optical engineering*. SPIE international society for optical, p 487–492
185. Anand L, Gurtin ME (2003) Thermal effects in the superelasticity of crystalline shape-memory materials. *J Mech Phys Solids* 51(6):1015–1058. [https://doi.org/10.1016/S0022-5096\(03\)00017-6](https://doi.org/10.1016/S0022-5096(03)00017-6)
186. Shahmir H, Nili-Ahmadabadi M, Mansouri-Arani M, Langdon TG (2013) The processing of NiTi shape memory alloys by equal-channel angular pressing at room temperature. *Mater Sci Eng A* 576:178–184. <https://doi.org/10.1016/j.msea.2013.04.001>
187. Shri DNA, Tsuchiya K, Yamamoto A (2014) Surface characterization of TiNi deformed by high-pressure torsion. *Appl Surf Sci* 289:338–344. <https://doi.org/10.1016/j.apsusc.2013.10.161>
188. Tang W (1997) Thermodynamic study of the low-temperature phase B19' and the martensitic transformation in near-equiatomic Ti-Ni shape memory alloys. *Metall Mater Trans A* 28(3):537–544. <https://doi.org/10.1007/s11661-997-0041-6>
189. Yang SY, Dui GS (2013) Temperature analysis of one-dimensional NiTi shape memory alloys under different loading rates and boundary conditions. *Int J Solids Struct* 50(20):3254–3265. <https://doi.org/10.1016/j.ijsolstr.2013.05.026>
190. Ortin J, Planes A (1988) Thermodynamic analysis of thermal measurements in thermoelastic martensitic transformations. *Acta Metall* 36(8):1873–1889
191. Hamilton RF, Sehitoglu H, Chumlyakov Y, Maier HJ (2004) Stress dependence of the hysteresis in single crystal NiTi alloys. *Acta Mater* 52(11):3383–3402. <https://doi.org/10.1016/j.actamat.2004.03.038>
192. Ramaiah K, Saikrishna C, Bhaumik S (2014) Ni₂₄ Ti₅₀ 3Pd₂₅. 0 high temperature shape memory alloy with narrow thermal hysteresis and high thermal stability. *Mater Des* (1980–2015) 56:78–83. <https://doi.org/10.1016/j.matdes.2013.10.079>
193. Pelton AR, Huang GH, Moine P, Sinclair R (2012) Effects of thermal cycling on microstructure and properties in nitinol. *Mater Sci Eng A* 532:130–138. <https://doi.org/10.1016/j.msea.2011.10.073>
194. Karaman I, Karaca HE, Luo Z, Maier H (2003) The effect of severe marforming on shape memory characteristics of a Ti-rich NiTi alloy processed using equal channel angular extrusion. *Metall Mater Trans A* 34(11):2527–2539. <https://doi.org/10.1007/s11661-003-0012-5>